IZMIR DEMOCRACY UNIVERSITY

NATURAL & APPLIED SCIENCES JOURNAL

IDUNAS

E-ISSN: 2645-9000

Year: 2019

Volume: 2, Issue: 2

Table of Contents

DOI: 10.38061/idunas.658011

IDUNAS	NATURAL & APPLIED SCIENCES JOURNAL	2019 Vol. 2 No. 2 (1-15)

Artificial Photosynthesis with Titania Photocatalysts

Review Article

Hüsnü Arda Yurtsever[1*], Muhsin Çiftçioğlu[2]

[1] *Adana Alparslan Türkeş Science and Technology University, Department of Materials Engineering, Adana, Turkey*
[2] *İzmir Institute of Technology, Department of Chemical Engineering, İzmir, Turkey*

Author E-mails
husnuarda@gmail.com
Tel: +90 322 455 00 00 / 2160
Fax: +90 322 455 00 39
*Correspondence to: H.A. Yurtsever, Adana Alparslan Türkeş Science and Technology University, Department of Materials Engineering, Adana, Turkey
DOI: 10.38061/idunas.658011

Received: December 11, 2019; Accepted: December 31, 2019

Abstract

Increasing energy demand and global warming due to extensive use of fossil fuels will soon force mankind to use clean and sustainable fuels and artificial photosynthesis is being considered as a promising solution to both problems. Photocatalysis is a light induced process involved in artificial photosynthesis and it will make a great contribution to the solution of environmental problems and generation of renewable energy sources. Titania based photocatalytic materials are one of the widely used materials in artificial photosynthesis research due to their unique chemical and optical properties. Recent research has shown that the activity of titania phases can be improved in the visible light region by several modification techniques. This article aims to present a brief review based on the last 2 decades of global research on the preparation and modification of titania based photocatalysts, their application and importance in artificial photosynthesis and its effect on reducing global warming by the development of a sustainable energy source. This review is mostly based on the PhD thesis of the corresponding author (Yurtsever, 2015).

Keywords: titania, artificial photosynthesis, global warming, sustainable energy

1.INTRODUCTION

Light energy of the sun captured and utilized by plants through photosynthesis processes in which inorganic substances like CO_2 and water are consumed for the synthesis of organic compounds necessary for their survival started and sustains the life processes of animals (Collings and Critchley, 2005). The balance in the plant-animal life processes was disturbed by human activities in the last two hundred years. Anthropogenic CO_2 emissions increased due to the increasing fossil fuel use since the beginning of industrial revolution and the excess CO_2 which cannot be consumed by the plants started to accumulate in the atmosphere.

In 1824, Jean Baptiste Fourier, a French mathematician, discovered that earth's temperature was rising gradually. This discovery which is about the atmosphere's capturing sunlight escaping and sending it back to the earth, led the basic theory of "Global Warming" arise. This theory was named as the "Greenhouse Effect" since 1990s. Scientific research showed that CO_2 emission originating from the fossil fuel usage as the main energy source is the reason for global warming (Collings and Critchley, 2005). Scientists found that earth's global temperature and sea levels raised approximately 0.6^oC and 20 cm, respectively, during 20^{th} century. The average temperature difference reached to 0.6^oC by 2000s. In the year 2100, global CO_2 concentration will reach from the present value of 369 ppmv to 650 ppmv unless the fearless fossil fuel consumption was stopped (Houghton, 2004).

Many governments are trying to take precautions by regulations since the discovery and acceptance of global warming. The most important international agreement to fight with the global warming is the "Kyoto Protocol" which was accepted in 1997. According to this protocol, greenhouse gases emissions would have been reduced beginning from 2005 by 125 countries which accepted this protocol (Collings and Critchley, 2005).

2. ENERGY FROM THE SUN

Energy from fossil fuels (e.g. oil, coal), nuclear energy and renewable energy (e.g. wind, solar and biomass) are possible choices that can be used to satisfy the energy demand of humanity and sustain life on earth. Geopolitical issues about fossil fuels, capital costs of constructing renewable energy producing facilities directed us to use non-sustainable fossil fuels. More than 80% of our energy is provided by fossil fuels at present. Our dependence on fossil fuels to create and sustain the well-being and development of society damages the nature irreversibly.

Use of fossil fuels to sustain the energy production until now caused the aforesaid global warming and pollution problem. Increasing energy demand and global warming due to extensive use of fossil fuels will soon force mankind to use clean and sustainable fuels. Solar energy is one of these sustainable energy resources to meet our present and future energy demand. Being limitless and free makes it a promising choice among these renewable resources. The hourly solar energy flux to the earth is more than the energy that we consume in a year. Our energy need can be provided by harvesting 0.02% of the energy from the sun without using any other energy resources. Solar energy can be converted into electrical energy for the simultaneous production and use or can be converted into heat or chemical energy and stored for the further use (Hammarstrom and Hammes-Schiffer, 2009).

The earth is heated with an energy flux of 1369 W/m^2 after 30% of solar energy is absorbed and scattered in the atmosphere. The reason for the loss of energy is the absorption by gases such as water, ozone, CO_2 and the scattering by clouds and aerosols in the atmosphere. Light with the wavelengths lower than 300 nm is absorbed by ozone, nitrogen and oxygen. Absorption in the infrared region is caused by water and CO_2. Solar radiation spectrum at the top of the atmosphere and at sea level is given in Figure 1. The solar light with a spectrum between 300 nm and 2500 nm reaches to the earth's surface after a portion is absorbed by the atmosphere. Solar radiation consists of three main regions. These are 5% UV (300-400 nm), 40% visible (400-800 nm) and 55% infrared (800-2500 nm) regions.

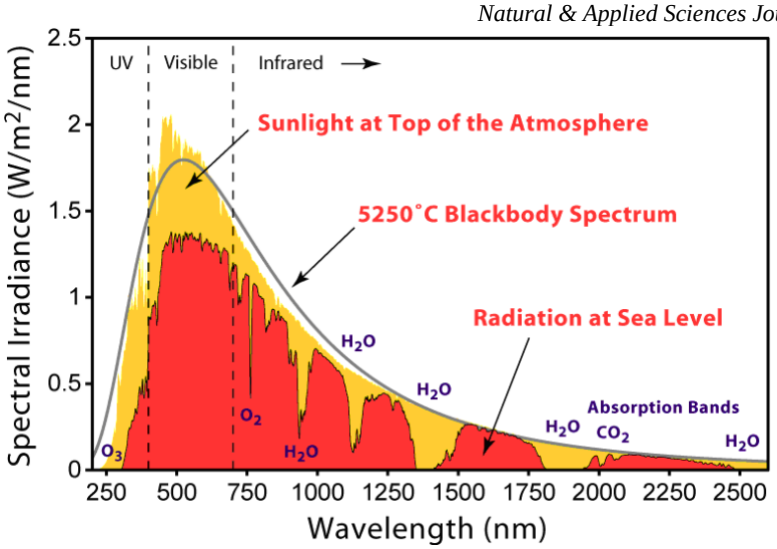

Figure 1. Solar radiation spectrum. (Robert A. Rohde, Global Warming Art project).

3. UTILIZATION OF SOLAR ENERGY VIA PHOTOCATALYSIS

Research on the utilization of solar energy to meet the energy demand gained significant interest in the last years. Among the most solar energy utilization techniques, artificial photosynthesis is promising since renewable and sustainable fuels can be generated while global CO_2 concentration in the atmosphere is reduced. (Cogdell et al., 2010). The properties of the photocatalyst materials have significant effect on the efficiency of the photocatalytic processes and artificial photosynthesis. These materials should be corrosion resistant (Zhu and Zach, 2009), chemically stable and cheap with high and efficient visible light absorption (Silija et al., 2012).

A photocatalyst is a semiconductor which is mostly an oxide of a metal having a specific band gap energy (E_g) between the conduction and valence band. Semiconductor becomes active when it is exposed to light having photons with energies equal to or higher than the band gap energy of that material (Figure 2). An electron (e-) hops from the conduction band leaving a hole (which can act as a positively charge electron) in the valence band of the semiconductor when the material is excited by photons (Linsebigler et al., 1995).

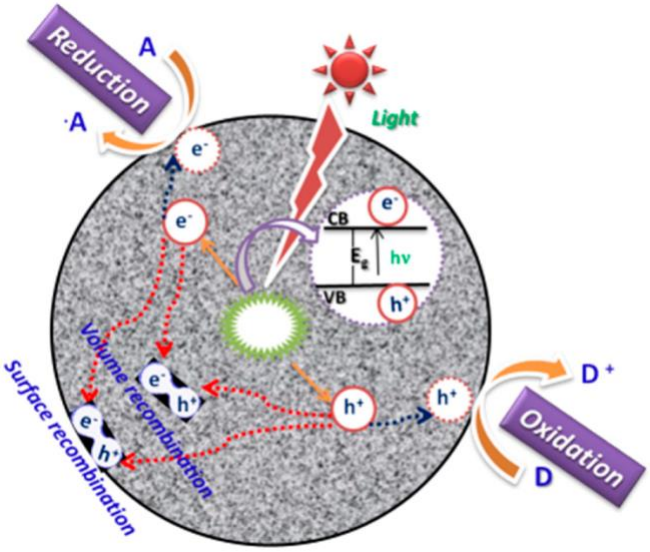

Figure 2. Schematic representation of photocatalysis mechanism (Kumar et al., 2018).

An ideal photocatalyst should have the following characteristics:

- photoactive,
- biologically and chemically inert,
- photostable (i.e., not prone to photocorrosion),
- inexpensive
- non-toxic.

Photocatalytic processes are started and carried on by the electron-hole pairs (e^--h^+) which are generated and separated on the surface of the semiconducting material. Excited electrons and holes can react with electron donors/acceptors adsorbed on the surface which triggers oxidation-reduction reactions or recombine/get trapped in surface states becoming useless from the viewpoint of photocatalysis (Zaleska, 2008). Electron-hole pairs generated in the lattice are separated and captured in suitable parts of the nanostructure to avoid recombination on the surface or in the volume. Holes conduct oxidation reactions and electrons conduct reduction reactions (Linsebigler et al., 1995). Electron transfer is more efficient when the reactants are preadsorbed on the surface of the photocatalyst. The probability and the rate of charge transfer process depend strictly on the band edge position of the semiconducting material and the redox potential of the adsorbed species. The bottom of conduction band of the semiconductor must be at a more negative potential than H^+/H_2 (0 V vs. NHE at pH 0) and the top of the valence band must be at a more positive potential than H_2O/O_2 (1.23 V vs. NHE at pH 0). The minimum electron energy should be 1.23 eV (the corresponding wavelength is around 1000 nm) for water splitting reaction to be thermodynamically possible (Zang, 2011). Some examples of photocatalysts and redox potentials of water splitting and oxidation of organics are given in Figure 3.

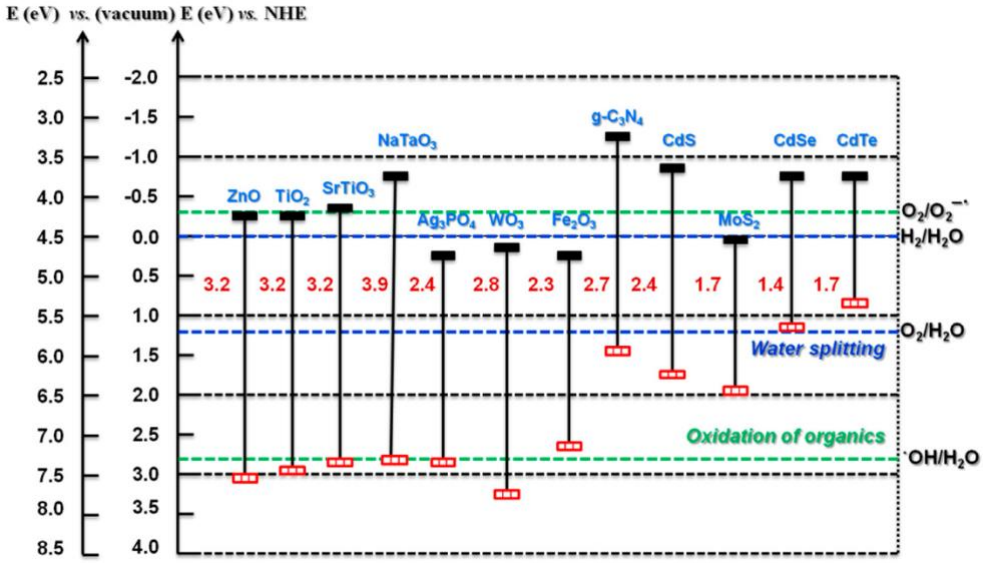

Figure 3. Relationship between band structure of semiconductor and redox potentials of water splitting and oxidation of organics (Kumar et al., 2018).

Nanostructured photocatalytic material preparation techniques were improved and the application area was expanded by the advances in nanotechnology in the last 20 years. Fujishima and Honda conducted the pioneering studies in 1970s to produce renewable energy via artificial photosynthesis and water splitting to produce hydrocarbons and hydrogen (Fusijhima et al., 1972, Inoue et al., 1979). A huge variety of photocatalytic materials to be used in different photocatalytic processes were prepared since Fujishima and Honda. Many oxide, sulfide, nitride based semiconducting materials are used as photocatalysts since they have sufficient band gap energies for photocatalysis. Some examples are TiO_2, WO_3, $SrTiO_3$ α-Fe_2O_3, ZnO, CuO, ZnS, CdS, CdSe, GaN. The band gap energies of these materials are 3.2, 2.8, 3.2, 3.1, 3.2, 1.2, 3.6,

2.4, 1.7, 3.4 eV, respectively (Hoffman et al., 1995). The boundary of UV and visible light regions is around 3.1 eV photon energy which corresponds to the energy of a light with 400 nm wavelength. TiO_2 is the most extensively used photocatalyst due its favorable properties such as biological and chemical inertness, thermal stability, photo/chemical corrosion stability and being cheap. The main applications of TiO_2 based phocatalysts are: photovoltaics, photoinduced superhydrophilicity and in photocatalysis, organic synthesis, degradation of pollutants, nitrogen fixation and artificial photosynthesis including hydrogen production and CO_2 reduction. The diverse applications of TiO_2 make it a favorable and preferred material in the photocatalysis area.

4. NATURAL AND ARTIFICIAL PHOTOSYNTHESIS

In natural photosynthesis plants and cyanobacteria (which are photoautotrophic) synthesize their own building block materials from inorganic compounds such as CO_2, nitrates, sulfates with the help of sunlight energy. Photon energy splits water into oxygen and hydrogen which is then bounded to NADPH (Nicotinamide adenine dinucleotide phosphate). This process, which is called as *Light Reactions*, is conducted at photosynthesis reaction centers embedded in cell wall and includes the electron transfer related to ATP (Adenozine triphosphate) synthesis. In *Dark Reactions*, NADPH, ATP and CO_2 is consumed in Calvin Cycle (Figure 4) to produce carbohydrates (Gan et al., 2019).

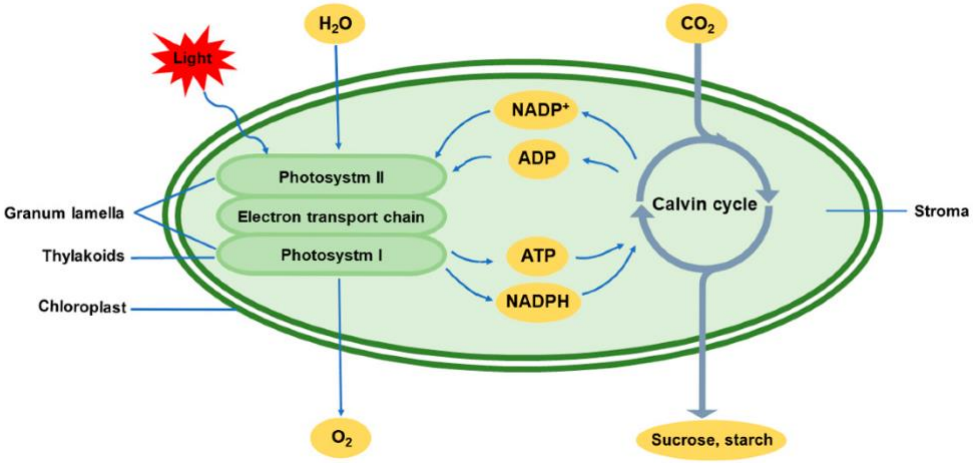

Figure 4. Photosynthesis under normal conditions (Gan et al., 2019).

Biomass, oxygen and also fossil fuels are the products of photosynthesis organized by plants and cyanobacteria. The life on earth is tied to photosynthesis and is a cycle of CO_2. Animals are heterotrophic and need carbohydrates/other organics to survive. They provide the energy for their own life processes by using biomass which is produced by plants. CO_2 is produced when oxygen is consumed. In brief, sunlight captured and utilized by plants is the source of life and related processes on earth.

Solar energy can be utilized by many different ways. Solar cells can transform solar energy into electricity, solar ponds can store the energy from the sun as heat energy and solar energy can be used to generate steam for turbines or transformed into chemical energy via photocatalysis (Hammarstrom and Hammes-Schiffer, 2009). Each method has its own advantages and disadvantages. Artificial photosynthesis is the mimicking of natural photosynthesis and is one of the common photocatalytic processes which convert CO_2 and water into useful chemicals such as methanol, methane, carbon monoxide, other hydrocarbons and hydrogen which can be stored and used as energy source.

CO_2 is a linear molecule (O=C=O) without a dipole moment and is one of the most stable compounds (but not inert) which is mostly produced by oxidation/combustion reactions. CO_2 needs high energy reducing molecules to be converted into hydrocarbons. The Gibbs free energy change of a reaction should be negative in order to be thermodynamically favorable. Most reactions given in Table 1 have positive

Gibbs free energy changes and reaction of CO_2 with H_2O seems thermodynamically unfavorable. High energy input is needed to convert CO_2 into hydrocarbons. Therefore, high temperatures and pressures are needed to activate CO_2. In photocatalysis, CO_2 can be activated by electrons and react with holes at room temperature and atmospheric pressure by the energy input from the sunlight. Reducing molecules such as H_2, H_2O or CH_4 are needed for this purpose among which H_2 seems to be more attractive since the Gibbs free energy changes of the reactions involving H_2 are low or negative. However, it is meaningless to reduce CO_2 with H_2 which has more chemical potential and the system loses its chemical potential by consuming H_2. If H_2 is produced by water splitting without synthetic energy input e.g. solar energy, not the energy from burning fossil fuels, the process would be feasible.

Table 1. Change of Gibbs free energy at 298 K for reactions related to the photocatalytic reduction of CO_2 to various renewable fuels (Zang, 2011).

Reductant	Product	Chemical equation	ΔG^0 (kJ/mol)
H_2	HCOOH	$CO_2+H_2 \rightarrow HCOOH$	43
	CH_3OH	$CO_2+3H_2 \rightarrow CH_3OH+H_2O$	4
	CH_4	$CO_2+4H_2 \rightarrow CH_4+2H_2O$	-114
CH_4	CH_3COCH_3	$CO_2+2CH_4 \rightarrow CH_3COCH_3+H_2O$	115
	CH_3COOH	$CO_2+CH_4 \rightarrow CH_3COOH$	71
	HCHO	$CO_2+CH_4 \rightarrow 2HCHO$	240
H_2O	HCOOH	$CO_2+H_2O \rightarrow HCOOH+1/2O_2$	272
	HCHO	$CO_2+H_2O \rightarrow HCHO+O_2$	521
	CH_3OH	$CO_2+2H_2O \rightarrow CH_3OH+3/2O_2$	690
	CH_4	$CO_2+2H_2O \rightarrow CH_4+2O_2$	801
		$H_2O(g) \rightarrow H_2+1/2O_2$	229
		$H_2O(l) \rightarrow H_2+1/2O_2$	237

The reaction of CO_2 with H_2 can be carried out either in gaseous or liquid phases. The form of CO_2 may vary depending on the phase (gas or a dissolved ion in water). Aqueous solutions of NaOH are used mostly in order to increase CO_2 solubility since it is soluble at high pH. CO_2 dissolves in water according to the following equilibrium reactions (Wojtowicz, 2001):

$CO_2(aq) + H_2O \leftrightarrow H_2CO_3$ (1)

$H_2CO_3 \leftrightarrow H^+ + HCO_3^-$ (2)

$HCO_3^- \leftrightarrow H^+ + HCO_3^{2-}$ (3)

Some selected redox potentials involving CO_2 species and hydrocarbons are given in Table 2. Gaseous CO_2 or water dissolved CO_2 (H_2CO_3) can be reduced to CH_3OH, CH_4, HCOOH with anatase TiO_2 whose valence and conduction band potentials are 2.7 and -0.5 V versus NHE, respectively. It is also seen that the reduction of gaseous CO_2 would be easier due to the closeness of the reduction potentials and conduction band potential of anatase TiO_2, however the products of photocatalytic CO_2 reduction with TiO_2 are not restricted to the given ones in Table 2 since the photocatalytic properties of TiO_2 can easily be tuned by several modification methods which may shift the band edge positions or change the reaction mechanism. This table is an illustration of the possible products that may be produced with TiO_2. There are reports of gaseous CO and CH_4 production when CO_2 reduction was carried out in aqueous conditions (Koci et al., 2009 and 2011, Rajalakshmi et al., 2012).

Table 2. Summary of reduction potentials for half-cell reactions at pH 7 in aqueous solution vs. the normal hydrogen electrode (Tahir and Amin, 2013).

Chemical equations	Thermodynamic potential, V vs. NHE
$CO_2 + e^- \rightarrow CO_2^-$	-2.0
$2H^+ + 2e^- \rightarrow H_2$	-0.41
$CO_2 + 2H^+ + 2e^- \rightarrow HCOOH$	-0.61
$CO_2 + 6H^+ + 6e^- \rightarrow CH_3OH + H_2O$	-0.38
$CO_2 + 8H^+ + 8e^- \rightarrow CH_4 + H_2O$	-0.24
$H_2CO_3 + 2H^+ + 2e^- \rightarrow HCOOH + H_2O$	-0.166
$H_2CO_3 + 6H^+ + 6e^- \rightarrow CH_3OH + 2H_2O$	+0.044
$2CO_3^{2-} + 8H^+ + 6e^- \rightarrow CH_3OH + 2H_2O$	+0.209

The mechanism of photocatalytic reduction of CO_2 consists of water splitting and reduction of CO_2 with species formed in water splitting reactions. Structural and electronic properties of semiconducting photocatalysts determine the important steps in photocatalysis such as the absorption of photons, charge separation/migration and surface adsorption/reactions. Captured holes react with water adsorbed on the surface of the semiconducting material to produce O_2 and H^+. H· radicals are formed by the interaction of H^+ ions with excited electrons. Union of two H^+ ions forms one H_2 molecule. These two steps explain the photocatalytic water splitting mechanism. In the presence of CO_2, electrons interact with CO_2 molecules to form $\cdot CO^-$ radicals (Koci et al., 2009). Newly formed H· and $\cdot CO^-$ radicals react to form CO. Consecutive reactions transform CO to $\cdot CH_3$ radicals. Finally, CH_4 or CH_3OH molecules are formed when $\cdot CH_3$ radicals react with H· or OH· radicals, respectively. These steps along with water splitting steps explain the photocatalytic reduction mechanism of CO_2 into hydrocarbons. The recombination of produced electron hole pairs can cause releasing of heat without chemical work which is not desired in photocatalysis.

5. ARTIFICIAL PHOTOSYNTHESIS WITH TITANIA PHOTOCATALYSTS

Intensive research on artificial photosynthesis (hydrogen production via water splitting and hydrocarbon production by the reduction of CO_2) which may become a key process in the future for sustainable energy needs of humanity and global pollution/warming prevention have been conducted in the last 20 years (Wu et al., 2005, Matejova et al., 2014, Raja et al., 2011, Tan et al., 2012, Uner et al., 2011, Zhang et al., 2009). Fujishima and Honda conducted the pioneering study in 1972 to produce hydrogen on a TiO_2 electrode (Fusijhima and Honda, 1972) and Inoue et al. (Fujishima and Honda who are the leading researchers of photocatalysis of TiO_2 were the co-workers in this study) reported the first photocatalytic reduction of CO_2 in aqueous media via photocatalytic processes by using solar energy in 1979. They used different photocatalysts such as TiO_2, WO_3, ZnO, GaP, CdS and SiC. The products of the reactions were formic acid, methanol, methane and formaldehyde (Inoue et al., 1979). Since then many studies on photoreduction of CO_2 were conducted. Early studies of photocatalytic reduction of CO_2 involved the use of SiC, GaP, $SrTiO_3$, WO_3, $BaTiO_3$, $LiNbO_3$, $CaFe_2O_4$, Cu_2OxH_2O, ZnS, CdS photocatalysts by Inoue et al. (1979), Ogura et al. (1992) and Yoneyama (1997). Intensive research on the photoreduction of CO_2 by using TiO_2 was conducted after this period due to the recognition of its extraordinary properties.

TiO_2 has three stable phases which are anatase, rutile, brookite along with three metastable and five high pressure phases. The lattice structures of anatase, rutile and brookite which are the most frequently used phases, are shown in Figure 5.

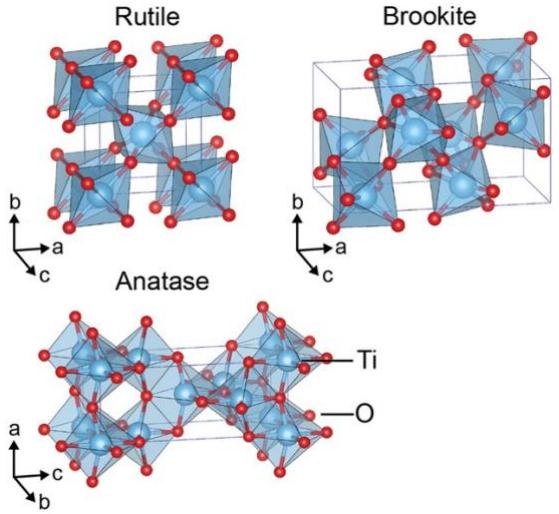

Figure 5. Lattice structures of anatase, rutile and brookite (Haggerty et al., 2017).

TiO_2 can be synthesized by various methods for industrial or laboratory uses. Sulfate and chloride methods are widely used for high production rates; however, alkoxide method is widely used in research for lab-scale applications. These methods are based on the chemical source of the desired product, however chemical vapor deposition, precipitation, hydro/solvothermal, sol-gel, emulsion/micro-emulsion, ultrasound/microwave irradiation, spray pyrolysis, electrochemical synthesis are common methods based on different apparatus used and different chemical and physical principles (Anpo and Kamat, 2010). According to the source, *Alkoxide Method*, according to the principles and apparatus *Sol-Gel* and *Chemical Precipitation Methods* along with a brief information about *Sulfate* and *Chloride Method* are described below.

Sulfate method

In sulfate method, titanium oxysulphate ($TiOSO_4$) which is formed by dissolving titanium minerals in sulfuric acid is treated with a base to form hydrated TiO_2. After heat treatment (calcination) crystalline TiO_2 powders are obtained. Hydrated TiO_2 synthesized by sulfate method has low photocatalytic activity since it has crystal defects which act as centers for recombination of electron-hole pairs, despite the high surface area. The calcined hydrated TiO_2 has also low photocatalytic activity because of the contaminants (sulfate ion or ions from minerals) originating from the method (Gazquez et al., 2014).

Chloride method

This method is also called as vapor method because titanium minerals are reacted with chlorine gas yielding titanium tetrachloride ($TiCl_4$) and oxidized to TiO_2 at 700-1000^{o}C. Crystallization of TiO_2 into anatase or rutile also occurs because of the application of high temperatures. Commercially available Degussa P-25 which is commonly used by researchers is synthesized by using this method. Degussa P-25 has 80 wt.% anatase and 20 wt.% rutile phases and has a very high photocatalytic activity under UV light illumination (Gazquez et al., 2014).

Alkoxide method (Sol-Gel)

Metal alkoxides are mostly used precursors for metal oxide synthesis in laboratory scale since the product of sulfate method has contaminations and chlorine method reaction conditions are hard to control. Metal alkoxide can also be produced in highly pure grade which leads to highly pure metal oxide. TiO_2 can be synthesized from various titanium alkoxides (e.g. titanium ethoxide, titanium propoxide, titanium butoxide). Titanium alkoxide is hydrolysed to form TiO_2 sol/precipitate. TiO_2 sol is then gelated to form polymeric TiO_2. Proper heat treatment of TiO_2 gels leads to highly active TiO_2 with high specific surface areas (Kaneko and Okura, 2002). This method is known as the ***"Sol-gel"*** method in the literature. Sol-gel

method has several advantages such as high purity and homogenous product, low temperature synthesis, excellent atomic mixing, precise control of size and surface properties, wide variety of precursors or other chemicals, possibility of different form of products such as films or powders. High amount of solvent usage in this method makes it infeasible for high production rates of TiO_2 (Tseng et al., 2010).

Chemical precipitation

Chemical precipitation is a liquid phase reaction which is used to synthesize insoluble solid particles. Solid particles obtained during precipitation, the precipitate, are formed in the solution due to a reaction or when the solution has been supersaturated by a compound. Titanium precipitates are titanium hydroxide ($Ti(OH)_4$), TiO_2 or titanium oxyhydroxide ($TiO(OH)_3$). Titanium precursor can be alkoxide based or inorganic (e.g. $TiCl_4$). The dissolved precursor solution is mostly precipitated by the use of an alkali solution since Ti^{4+} is soluble in acidic conditions. The precipitates can be crystalline or amorphous particles. After a heat treatment, oxide particles can be obtained. Usually an aqueous or alcohol solution of inorganic salt (sulfate, chloride or nitrate) of desired dopant ion is used to modify TiO_2 and Ti^{4+} is precipitated with dopant ions in an alkali solution (of NH_4OH, NaOH). Unwanted growth of particles is inevitable during calcination. Thus, direct precipitation from a non-aqueous solution may be carried out in order to obtain ultrafine particles.

The commonly known anatase and rutile phases of titania (TiO_2) are the most important and widely used materials in environmental related photocatalytic research and applications. The most important disadvantage of these titania phases is their relatively high band gap energies (in the 3.0-3.2 eV range) which results in absorption of sun light in the ultra-violet (UV) range which represents < 5% of solar radiation spectrum (Nassoko et al., 2012). The reduction and modification of the band gap energies of the titania phases by doping with various elements for more efficient light absorption and the determination of their activities in the photocatalytic degradation of organic molecules and artificial photosynthesis are the main concern of intense research in the last 10-15 years. These dopants comprise heavily nonmetals like C, N, S etc. (Cong et al., 2007, Dong et al., 2011, Park et al., 2006, Rockafellow et al., 2009, Shen et al., 2007, Yang et al., 2010) and transition metals like Cu, Ag, Fe, Co etc. (Akpan and Hameed, 2010, Silija et al., 2012, Baiju et al., 2007, Nie et al., 2009). Research conducted in the last 20 years on the effects of titania phase stability and dye decomposition activities have shown that lanthanide incorporation also reduced the band gap energy, widened absorption into the visible light region and increased the photocatalytic activity of TiO_2 (Choudhury et al., 2013, Li et al., 2004, Obregon et al., 2013, Ranjit et al., 2001, Xiao et al., 2007).

Band gap engineering for improving the photocatalytic activity of TiO_2 can be accomplished by;

- doping TiO_2 with various cations/anions (metal or nonmetal) to introduce sub energy levels between the conduction and valence band (Zaleska, 2008),
- combining with low band gap materials; a coupled semiconductor mechanism in which low band gap semiconductor absorbs the photons of visible light and transfers them to the surface of TiO_2 (Magesh et al., 2009),
- surface modification (Dugandzic et al., 2012),
- using different synthesis routes to modify the crystallite sizes.

Using different synthesis routes such as chemical vapor deposition, precipitation, hydro/solvothermal, sol-gel, emulsion/micro-emulsion, ultrasound/microwave irradiation, spray pyrolysis, electrochemical synthesis methods, as stated previously, may alter the physicochemical, optical and electronic properties by tuning the surface chemistry, pore structure or crystallinity of TiO_2. Phase composition (anatase to rutile weight ratio), crystallite size, band-to-band transitions have significant effect on the band gap energy of semiconductors. Changing the synthesis route may significantly change these properties and thus the band gap energy of TiO_2. Combining TiO_2 with low band gap materials is also another versatile method to improve the optical properties of TiO_2. According to this coupled mechanism,

a visible light absorbing material can transfer electrons to the conduction band of TiO_2 and redox reactions are started by these lower energy charge carriers.

Doping TiO_2 with anions/cations is the most preferred one since it is easy to tune the absorption edge by the type or amount of doping ion which leads to the improvement of photocatalytic activity. Interpretations on the contribution of doped ions to the electronic structure of TiO_2 can be done considering the valence band of TiO_2 is at oxygen 2p state and conduction band is at titanium 3d&4s state. Metal doping introduces new energy levels in the band gap of TiO_2 which narrows the band gap and improves the light absorption of TiO_2. Transition metal doping also enables the trapping of electrons which inhibits the electron-hole recombination and improves oxidation-reduction activity of TiO_2. Nonmetal doping improves the light absorption and photocatalytic activity of TiO_2 by three mechanisms. First one is the band gap narrowing by hybridization of oxygen 2p with nonmetal 2p by introducing a new valence band closer to the conduction band. Second one is the introduction of isolated impurity levels in which electrons are excited only by visible light. Electrons in the valence band and impurity level are both excited with UV irradiation, however visible light only excites the electrons in the impurity level. Third one is the creation of holes localized in oxygen vacancies forming O_2^{-}. and OH^{-}. radicals which trigger the oxidation reactions (Zaleska, 2008).

Doping can be achieved by various methods e.g. chemical vapor deposition, ion-assisted sputtering, ion implantation and chemical synthesis methods such as sol-gel and chemical precipitation. Mostly used methods are chemical precipitation and sol-gel which were described previously. Transition metals (such as V, Cr, Fe, Co, Ni, Cu) and nonmetals (N, S, C, B, P, I, F) doped TiO_2 photocatalysts were prepared in various research papers presenting the band gap tuning (Bellardita et al., 2011, Magesh et al., 2009, Zaleska, 2008). An example of UV-Vis Diffuse Reflectance spectrum presenting the band gap tuning and red shift of the absorption edge of TiO_2 is given in Figure 6.

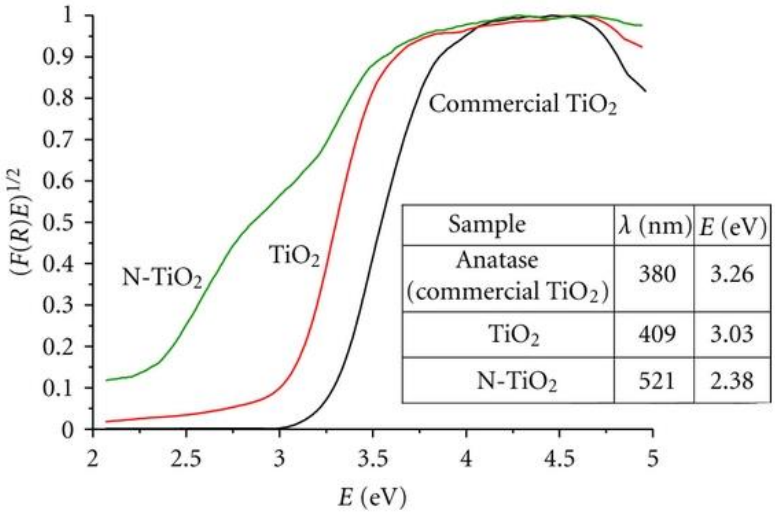

Figure 6. Band gap narrowing of TiO_2 by N doping (Factorovich et al., 2011).

A summary of dopant/composite materials, estimated band gap energies and main products of photocatalytic reduction of CO_2 with TiO_2 based materials reported in research papers from the last 20 years is given in Table 3.

Table 3. A brief summary of the last 20 years of photocatalytic reduction of CO_2 with TiO_2 based materials.

Dopant/ Composite material	Band gap energy (eV)	Main Products	Reference
2.0 wt. % Cu	3.0 eV	MOH	Tseng et al., 2002
Ru/SiO_2	3.04 eV	H, FA, FAL, MN	Sasirekha et al., 2006
RuBpy	NA	MN	Ozcan et al. 2007
Ag	2.74 eV	MN, MOH	Koci et al. 2010
N/nanotube	3.1 eV	FA	Zhao et al. 2012
CeO_2	2.2 eV	MN, CO	Wang et al. 2013
Pt	2.06 eV	MN	Xiong et al. 2015
Au-CdS	2.40 eV	MN	Wei et al. 2015
CPO27-Mg	NA	MN	Wang et al. 2016
NH_2-UiO-66	2.70 eV	CO	Crake et al. 2017
$CuInS_2$	NA	MOH, MN	Xu at al. 2018
Nd	1.83	CO	Yurtsever et al. 2018
AuCu + ZIF-8	NA	MN, CO	Butburee at al. 2019
C_3N_4	2.34	CO, H	Shi et al. 2019

MOH: Methanol, FA: Formic acid, FAL: Formaldehyde, H: Hydrogen, CO: Carbon monoxide, MN: Methane.

6. CONCLUSION

Titania photocatalysts used in artificial photosynthesis will contribute to the development of renewable energy resources in the near future by hydrogen production via water splitting and hydrocarbon production via CO_2 photoreduction. Research conducted in the last 20 years on titania based materials developed towards photocatalytic water splitting and artificial photosynthesis was briefly reviewed in this paper. The superior properties and chemical stability of titania which was the main reason behind its frequent use in the long past history of artificial photosynthesis will continue to make it a popular and preferred material for use in diverse photocatalytic applications in the near future. This review also shows that titania coupled with recently developed novel materials such as metal organic frameworks and 2D nanosheets may present novel and efficient photocatalysts to be used in artificial photosynthesis.

REFERENCES

Akpan, U.G., Hameed, B.H. (2010). The advancements in sol–gel method of doped-TiO2 photocatalysts. *Applied Catalysis A: General*, 375, 1-11.

Anpo, M., Kamat, P.V., (2010). Environmentally benign photocatalysts applications of titanium oxide-based materials. USA: Springer.

Baiju, K.V., Periyat, P., Wunderlich, W., Krishna Pillai, P., Mukundan, P., Warrier, K.G.K. (2007). Enhanced photoactivity of neodymium doped mesoporous titania synthesized through aqueous sol–gel method. *Journal of Sol-Gel Science and Technology*, 43, 283-290.

Bellardita, M., Addamo, M., Di Paola, A., Palmisano, L. (2007). Photocatalytic behaviour of metal-loaded TiO2 aqueous dispersions and films. *Chemical Physics*, 339, 94-103.

Butburee, T., Sun, Z., Centeno, A., Xie, F., Zhao, Z., Wu, D. et al. (2019). Improved CO2

photocatalytic reduction using a novel 3-component heterojunction. *Nano Energy*, 62, 426-433.

Choudhury, B., Borah, B., Choudhury, A. (2013). Ce–Nd codoping effect on the structural and optical properties of TiO2 nanoparticles. *Materials Science and Engineering: B*, 178, 239-247.

Cogdell, R.J., Brotosudarmo, T.H.P., Gardiner, A.T., Sanchez, P.M., Cronin, L. (2010). Artificial photosynthesis – solar fuels: current status and future prospects. *Biofuels*, 1, 861-876.

Collings, A.F., Critchley, C., (2005). *Artificial photosynthesis from basic biology to industrial application*. Germany: Wiley-VCH.

Cong, Y., Zhang, J., Chen, F., Anpo, M. (2007). Synthesis and characterization of nitrogen-doped TiO2 nanophotocatalyst with high visible light activity. *The Journal of Physical Chemistry C*, 111, 6976-6982.

Crake, A., Christoforidis, K. C., Kafizas, A., Zafeiratos, S., & Petit, C. (2017). CO2 capture and photocatalytic reduction using bifunctional TiO2/MOF nanocomposites under UV–vis irradiation. *Applied Catalysis B: Environmental*, 210, 131-140.

Dong, F., Guo, S., Wang, H., Li, X., Wu, Z. (2011). Enhancement of the visible light photocatalytic activity of c-doped TiO2 nanomaterials prepared by a green synthetic approach. *The Journal of Physical Chemistry C*, 115, 13285-13292.

Dugandžić, I.M., Jovanović, D.J., Mančić, L.T., Zheng, N., Ahrenkiel, S.P., Milošević, O.B., Šaponjić, Z.V., Nedeljković, J.M. (2012). Surface modification of submicronic TiO2 particles prepared by ultrasonic spray pyrolysis for visible light absorption. *Journal of Nanoparticle Research*. 14, 1-11.

Factorovich M., Guz L., Candal R. (2011). N-TiO2: chemical synthesis and photocatalysis. *Advances in Physical Chemistry*, 2011, 821204.

Fujishima, A., Honda, K. (1972). Electrochemical photolysis of water at a semiconductor electrode. *Nature*, 238, 37-38.

Gan, P., Liu, F., Li, R., Wang, S., & Luo, J. (2019). Chloroplasts-beyond energy capture and carbon fixation: tuning of photosynthesis in response to chilling stress. *International Journal of Molecular Sciences*, 20(20), 5046.

Gázquez, M.J., Bolívar, J.P., Garcia-Tenorio, R., Vaca, F. (2014). A review of the production cycle of titanium dioxide pigment. *Materials Sciences and Applications*, 05, 441-458.

Haggerty, J.E.S., Schelhas, L.T., Kitchaev, D.A. (2017). High-fraction brookite films from amorphous precursors. *Scientific Reports*, 7, 15232.

Hammarstrom, L., Hammes-Schiffer, S. (2009). Artificial photosynthesis and solar fuels. *Accounts of Chemical Research*, 42, 1859-1860.

Hoffmann, M.R., Martin, S.T., Choi, W., Bahnemann, D.W. (1995). Environmental applications of semiconductor photocatalysis. *Chemical Reviews*, 95, 69-96.

Houghton, J. (2004). *Global warming the complete briefing.* USA: Cambridge University Press.

Inoue, T., Fujishima, A., Konishi, S., Honda, K. (1979). Photoelectrocatalytic reduction of carbon dioxide in aqueous suspensions of semiconductor powders. *Nature*, 277, 637-638.

Kaneko, M., Okura I. (2002). *Photocatalysis : science and technology*. Kodansha: Springer.

Kočí, K., Obalová, L., Matějová, L., Plachá, D., Lacný, Z., Jirkovský, J., Šolcová, O. (2009). Effect of TiO2 particle size on the photocatalytic reduction of CO2. *Applied Catalysis B: Environmental*, 89, 494-502.

Kočí, K., Matějů, K., Obalová, L., Krejčíková, S., Lacný, Z., Plachá, D., Čapek, L., Hospodková, A., Šolcová, O. (2010). Effect of silver doping on the

TiO2 for photocatalytic reduction of CO2. *Applied Catalysis B: Environmental*, 96, 239-244.

KočÍ, K., ZatloukalovÁ, K., ObalovÁ, L., KrejČÍKovÁ, S., LacnÝ, Z., ČApek, L., HospodkovÁ, A., ŠOlcovÁ, O. (2011). Wavelength effect on photocatalytic reduction of CO2 by Ag/TiO2 catalyst. *Chinese Journal of Catalysis*, 32, 812-815.

Kumar, S., Karthikeyan, S., Lee, A.F. (2018). g-c3n4-based nanomaterials for visible light-driven photocatalysis. *Catalysts*, 8, 74.

Li, F.B., Li, X.Z., Hou, M.F. (2004). Photocatalytic degradation of 2-mercaptobenzothiazole in aqueous La3+–TiO2 suspension for odor control. *Applied Catalysis B: Environmental*, 48, 185-194.

Linsebigler, A.L., Lu, G., Yates, J.T. (1995). Photocatalysis on TiO2 surfaces: principles, mechanisms, and selected Results. *Chemical Reviews*, 95, 735-758.

Magesh, G., Viswanathan, B., Viswanath, R.P., Varadarajan, T.K. (2009). Photocatalytic behavior of CeO2-TiO2 system for the degradation of methylene blue. *Indian Journal of Chemistry*, 48A, 480-488.

Matějová, L., Kočí, K., Reli, M., Čapek, L., Hospodková, A., Peikertová, P., Matěj, Z., Obalová, L., Wach, A., Kuśtrowski, P., Kotarba, A. (2014). Preparation, characterization and photocatalytic properties of cerium doped TiO2: On the effect of Ce loading on the photocatalytic reduction of carbon dioxide. *Applied Catalysis B: Environmental*, 152-153, 172-183.

Nassoko, D., Li, Y.-F., Li, J.-L., Li, X., Yu, Y. (2012). Neodymium-doped TiO2 with anatase and brookite two phases: mechanism for photocatalytic activity enhancement under visible light and the role of electron. *International Journal of Photoenergy*, 2012, 1-10.

Nie, X., Zhuo, S., Maeng, G., Sohlberg, K. (2009). Doping of TiO2 polymorphs for altered optical and photocatalytic properties. *International Journal of Photoenergy*, 2009, 1-22.

Obregón, S., Kubacka, A., Fernández-García, M., Colón, G. (2013). High-performance Er3+–TiO2 system: Dual up-conversion and electronic role of the lanthanide. *Journal of Catalysis*, 299, 298-306.

Ogura, K., Kawano, M., Yano, J., Sakata, Y. (1992). Visible-light-assisted decomposition of H2O and photomethanation of CO2 over CeO2-TiO2 catalyst. *Journal of Photochemistry and Photobiology A: Chemistry*. 66, 91-97.

Ozcan, O., Yukruk, F., Akkaya, E., Uner, D. (2007). Dye sensitized artificial photosynthesis in the gas phase over thin and thick TiO2 films under UV and visible light irradiation. *Applied Catalysis B: Environmental*, 71, 291-297.

Park, J.H., Kim, S., Bard, A.J. (2006). Novel carbon-doped TiO2 nanotube arrays with high aspect ratios for efficient solar water splitting. *Nano Letters*. 6, 24-28.

Raja, K.S., Smith, Y.R., Kondamudi, N., Manivannan, A., Misra, M., Subramanian, V. (2011). CO2 photoreduction in the liquid phase over pd-supported on TiO2 nanotube and bismuth titanate photocatalysts. *Electrochemical and Solid-State Letters*, 14, F5-F8.

Rajalakshmi, K., Jeyalakshmi, V., Krishnamurthy, K.R., Viswanathan, B. (2012). Photocatalytic reduction of carbon dioxide by water on titania: role of photophysical and structural properties. *Indian Journal of Chemistry*. 51A, 411-419.

Ranjit, K.T., Willner, I., Bossmann, S.H., Braun, A.M. (2001). Lanthanide oxide doped titanium dioxide photocatalysts: effective photocatalysts for the enhanced degradation of salicylic acid and t-cinnamic acid. *Journal of Catalysis*. 204, 305-313.

Rohde, Robert A., Solar radiation spectrum, (http://www.globalwarmingart.com/), licence: https://creativecommons.org/licenses/by-sa/3.0/deed.en.

Rockafellow, E.M., Stewart, L.K., Jenks, W.S. (2009). Is sulfur-doped TiO2 an effective visible light photocatalyst for remediation?. *Applied Catalysis B: Environmental*. 91, 554-562.

Sasirekha, N., Basha, S., Shanthi, K. (2006). Photocatalytic performance of Ru doped anatase mounted on silica for reduction of carbon dioxide. *Applied Catalysis B: Environmental*. 62, 169-180.

Shen, H., Mi, L., Xu, P., Shen, W., Wang, P.-N. (2007). Visible-light photocatalysis of nitrogen-doped TiO2 nanoparticulate films prepared by low-energy ion implantation. *Applied Surface Science*. 253, 7024-7028.

Shi, H., Long, S., Hu, S., Hou, J., Ni, W., Song, C. et al. (2019). Interfacial charge transfer in 0D/2D defect-rich heterostructures for efficient solar-driven CO2 reduction. *Applied Catalysis B: Environmental*, 245, 760-769.

Silija, P., Yaakob, Z., Suraja, V., Binitha, N.N., Akmal, Z.S. (2012). An enthusiastic glance in to the visible responsive photocatalysts for energy production and pollutant removal, with special emphasis on titania. *International Journal of Photoenergy*. 2012, 1-19.

Tahir, M., Amin, N.S. (2013). Recycling of carbon dioxide to renewable fuels by photocatalysis: prospects and challenges. *Renewable and Sustainable Energy Reviews*. 25, 560-579.

Tan, J.Z.Y., Fernández, Y., Liu, D., Maroto-Valer, M., Bian, J., Zhang, X. (2012). Photoreduction of CO2 using copper-decorated TiO2 nanorod films with localized surface plasmon behavior. *Chemical Physics Letters.* 531, 149-154.

Tseng, I.H., Chang, W.-C., Wu, J.C.S. (2002). Photoreduction of CO2 using sol–gel derived titania and titania-supported copper catalysts. *Applied Catalysis B: Environmental*. 37, 37-48.

Tseng, T.K., Lin, Y.S., Chen, Y.J., Chu, H. (2010). A review of photocatalysts prepared by sol-gel method for VOCs removal. *International Journal of Molecular Sciences*. 11, 2336-2361.

Uner, D., Oymak, M.M., İpek, B. (2011). CO2 utilisation by photocatalytic conversion to methane and methanol. *International Journal of Global Warming*. 3, 142-162.

Wang, Y., Li, B., Zhang, C., Cui, L., Kang, S., Li, X., Zhou, L. (2013). Ordered mesoporous CeO2-TiO2 composites: highly efficient photocatalysts for the reduction of CO2 with H2O under simulated solar irradiation. *Applied Catalysis B: Environmental*. 130-131, 277-284.

Wang, M., Wang, D., & Li, Z. (2016). Self-assembly of CPO-27-Mg/TiO2 nanocomposite with enhanced performance for photocatalytic CO2 reduction. *Applied Catalysis B: Environmental*, 183, 47-52.

Wei, Y., Jiao, J., Zhao, Z., Liu, J., Li, J., Jiang, G. et al. (2015). Fabrication of inverse opal TiO2-supported Au@CdS core–shell nanoparticles for efficient photocatalytic CO2 conversion. *Applied Catalysis B: Environmental*, 179, 422-432.

Wojtowicz, J.A. (2001). The carbonate system in swimming pool water. *Journal of the Swimming Pool and Spa Industry*. 4, 54-59.

Wu, J.C.S., Lin, H.-M., Lai, C.-L. (2005). Photo reduction of CO2 to methanol using optical-fiber photoreactor. *Applied Catalysis A: General*. 296, 194-200.

Xiao, Q., Si, Z., Zhang, J., Xiao, C., Yu, Z., Qiu, G. (2007). Effects of samarium dopant on photocatalytic activity of TiO2 nanocrystallite for methylene blue degradation. *Journal of Materials Science*. 42, 9194-9199.

Xiong, Z., Wang, H., Xu, N., Li, H., Fang, B., Zhao, Y. et al. (2015). Photocatalytic reduction of CO2 on Pt2+–Pt0/TiO2 nanoparticles under UV/Vis light irradiation: A combination of Pt2+ doping and Pt nanoparticles deposition. *International Journal of Hydrogen Energy*, 40(32), 10049-10062.

Xu, F., Zhang, J., Zhu, B., Yu, J., & Xu, J. (2018). CuInS2 sensitized TiO2 hybrid nanofibers for

improved photocatalytic CO2 reduction. *Applied Catalysis B: Environmental*, 230, 194-202.

Yang, G., Jiang, Z., Shi, H., Xiao, T., Yan, Z. (2010). Preparation of highly visible-light active N-doped TiO2 photocatalyst. *Journal of Materials Chemistry*. 20, 5301.

Yoneyama, H. (1997). Photoreduction of carbon dioxide on quantized semiconductor nanoparticles in solution. *Catalysis Today*. 39, 169-175.

Yurtsever, H. A., (2015). Preparation and characterization of titania based powders and suspensions for photocatalytic applications. PhD Thesis, Graduate School of Engineering and Sciences of Izmir Institute of Technology.

Yurtsever, H. A., Çiftçioğlu, M. (2018). The effect of powder preparation method on the artificial photosynthesis activities of neodymium doped titania powders. *International Journal of Hydrogen Energy*, 43(44), 20162-20175.

Zaleska, A. (2008). Doped-TiO2: a review. *Recent Patents on Engineering*. 2, 157-164.

Zang, L., (2011). Energy efficiency and renewable energy through nanotechnology. USA: Springer.

Zhang, Q.-H., Han, W.-D., Hong, Y.-J., Yu, J.-G. (2009). Photocatalytic reduction of CO2 with H2O on Pt-loaded TiO2 catalyst. *Catalysis Today*. 148, 335-340.

Zhao, Z., Fan, J., Wang, J., Li, R. (2012). Effect of heating temperature on photocatalytic reduction of CO2 by N–TiO2 nanotube catalyst. *Catalysis Communications*. 21, 32-37.

Zhu, J., Zäch, M. (2009). Nanostructured materials for photocatalytic hydrogen production. *Current Opinion in Colloid & Interface Science*. 14, 260-269.

DOI: 10.38061/idunas.657975

IDUNAS	NATURAL & APPLIED SCIENCES JOURNAL	2019 Vol. 2 No. 2 (16-29)

Synthesis and Characterization of Oleic Acid Coated Magnetic Nanoparticles for Hyperthermia Applications

Research Article

Fatih Şentürk[1]*, Soner Çakmak[2], Göknur Güler Ozturk[1]

[1]Department of Biophysics, Faculty of Medicine, Gazi University, Ankara, Turkey.
[2]Department of Bioengineering, Graduate School of Science and Engineering, Hacettepe University, Ankara, Turkey.

Author E-mail:
senturkfatih52@gmail.com
*Correspondence to: F. Şentürk, Department of Biophysics, Faculty of Medicine, Gazi University, Ankara, Turkey
DOI: 10.38061/idunas.657975

Received: December 11, 2019; Accepted: December 31, 2019

Abstract

The present study focuses on obtaining highly stable iron oxide nanoparticles (IONs), stabilized by the coating of oleic acid (OA) for magnetic nano hyperthermia (MNH) applications. For this purpose, bare and different amounts of oleic acid (0.2%, 0.5% and 1.0%, v/v) coated IONs were prepared by co-precipitation method. Then, their structures, morphologies, magnetic properties and heating abilities were characterized by using suitable techniques. IONs+1.0%OA nanoparticles showed low agglomeration with high dispersion capacity. Moreover, 1.0% OA coating showed the highest heating ability with a temperature increase of (25.2 °C) compared to IONs+OA (0.2%, 16.4 °C; 0.5%, 19 °C), but similar to bare IONs (26.7 °C). The specific absorption rate (SAR) values of bare IONs and IONs+OA (0.2%, 0.5%, 1.0%, v/v) were found as 39.50, 34.81, 23.36 and 45.98 W/g, respectively. Our results showed that comparable hyperthermia effect of IONs+1.0%OA with bare IONs was attributable to their uniform dispersion performance along with higher SAR values. We concluded that the dispersion of hydrophobic IONs+OA in the aqueous medium is one of the critical requirements for increasing temperature in magnetic nano hyperthermia applications.

Keywords: Iron oxide nanoparticles, magnetic hyperthermia, oleic acid, co-precipitation.

1.INTRODUCTION

Hyperthermia is introduced as an adjuvant therapy for various cancers, in which the targeted tissue is exposed to high temperatures. Traditional hyperthermia produces the highest temperature gradient on the body's surface that immediately diminishes with distance from the heat-generating sources such as radiofrequency, microwave, laser, ultrasound and magnetic field [1, 2]. Therefore, the heat delivery rate to the tumor site remains quite limited. Nanomaterials have the potential for use as the hyperthermia agents that can absorb energy from the external magnetic field and increase the effect of heating in tumor site [3, 4].

Magnetic nano hyperthermia (MNH) is a promising therapeutic procedure for the treatment of various cancers. It depends on the idea that magnetic nanoparticles delivered to tumors can generate heat after exposure to the noninvasive magnetic field and consequently induce cell death [5]. The increase of temperatures above 46 °C lead cancer cells to necrosis, whereas moderate temperature increases up to 41 °C - 45 °C might change the functionality of intercellular proteins that cause cellular degradation and induce apoptosis [1, 5]. In contrast to necrosis, hyperthermia induced apoptosis is a preferable cellular death pathway for tumor eradication because it does not cause undesirable effects on healthy tissue [3, 6].

Iron oxide nanoparticles (IONs) have received tremendous attention because of their unique magnetic properties, high surface area, magnetothermal effect and biocompatibility. For many years, IONs have been successfully used for bio-applications that include targeted drug delivery, magnetic separation and magnetic nano hyperthermia (MNH) [7-9]. Iron oxide nanoparticles could be utilized as MNH agents to trigger heat-induced cell death [3]. When IONs are targeted or injected into tumor site and exposed to an alternating magnetic field, they become a source of heat which capable of increasing temperature to kill cancer cells [10]. However, the effective interaction between magnetic fields and IONs depends on the physical and chemical properties of nanoparticles, such as size, shape, saturation magnetization, state of aggregation and monodispersibility, etc. [11].

Chemical co-precipitation is the most conventional method for the production of IONs because of its simplicity and productivity. This method is based on the reaction between ferric and ferrous ions in aqueous media under basic conditions. Although gram-scale production and facility are the best-known advantages of the co-precipitation, the obtained IONs are highly agglomerated because of difficulty in controlling particle-particle interactions and distributions [12, 13]. Agglomeration of nanoparticles is a major challenge for biological applications. This also reduces the heating ability of IONs. Therefore, IONs generally coated with surfactants such as oleic acid (OA), polyethylene glycol (PEG), or citric acid. Oleic acid stabilizes the IONs and prevents oxidation or erosion caused by oxygen and acid or base, respectively [14]. Moreover, OA coating facilitates IONs uniform suspension performance such as dispersibility and stability [12, 14].

There are some studies investigating OA coating on IONs within low (0–1.5 wt%) or high (8–96 wt%) OA concentration[15, 16]. Lai et al. investigated low OA concentrations for IONs coating and they only determined optimum OA loading amount in terms of IONs colloidal stability [15]. On the other hand, Ghosh et al. used high OA concentrations and they characterized the heating ability of OA coated IONs [17]. Some other studies functionalized the surface of IONs with using constant OA concentration and the heating potential of the OA coated IONs were determined for hyperthermia applications [18, 19].

Although oleic acid is a commonly used surfactant to encapsulate magnetic nanoparticles, as far as we know, few studies have been carried out on the heating ability of OA coated IONs for hyperthermia studies. Hence, we have investigated the effect of (i) low OA concentrations on physical and chemical properties of iron oxide nanoparticles, (ii) different amounts of nanoparticles and OA concentrations on heating performance of IONs under relatively low alternating magnetic field, with comprehensive characterization techniques. In this study, we have prepared OA coated iron oxide nanoparticles by co-precipitation method. The structure, morphology and magnetic properties of nanoparticles were characterized by using the X-ray diffraction (XRD), Fourier transform infrared spectroscopy (ATR-FTIR), thermogravimetric analysis (TGA), transmission electron microscopy (TEM), dynamic light scattering (DLS) and vibrating sample magnetometer (VSM). Then, the induction heating ability and specific absorption rate (SAR) values of nanoparticles were evaluated under exposure of alternating magnetic field.

The amount of optimum oleic acid concentration required on the IONs and concentration dependent heating abilities of IONs were investigated for hyperthermia efficiency.

2. EXPERIMENTAL SECTION

2.1. Materials

Ferric chloride hexahydrate ($FeCl_3.6H_2O$), ferrous chloride tetrahydrate ($FeCl_2.4H_2O$) and oleic acid (OA, technical grade, 90%) were purchased from Sigma Aldrich (USA). Ammonium hydroxide (NH_4OH, 25%) and hydrochloric acid (HCl, 37%) were obtained from Merck (Germany).

2.2. Synthesis of iron oxide nanoparticles

Iron oxide nanoparticles were prepared by co-precipitation method according to the Massart's procedure [20]. Ultra-pure water used for solution preparations was degassed with nitrogen for 30 min before synthesis. In a typical synthesis, aqueous solutions of ferric chloride hexahydrate (8 mL; 2.162 g; 1 M) and ferrous chloride tetrahydrate (2 mL; 0.793 g; 2 M HCl) was added to 100 mL of ultra-pure water in a three necked flask. Then, the solution temperature was increased step by step to 50 °C under constant stirring, followed by dropwise addition of ammonium hydroxide (5.3 mL; 0.7 M) solution. After that, the reaction was cooled to room temperature and the resultant suspension was washed three times with ultra-pure water to remove excess ammonia. The mixture was located on a neodymium magnet followed by removal of the upper supernatant. Finally, the black precipitate was dried under vacuum for further analysis.

2.3. Synthesis of oleic acid coated iron oxide nanoparticles

In situ oleic acid coating of IONs with different concentrations (0.2%, 0.5% and 1.0%, v/v) were carried out with the same procedure described above where OA was poured into the reaction mixture before the addition of ammonium hydroxide solution. Then, the same as bare IONs synthesis, the reaction was cooled to room temperature and oleic acid coated IONs were washed repeatedly with ultra-pure water and ethanol, respectively. OA coated IONs were collected by magnetic decantation and dried under vacuum for further characterizations. After this point, bare nanoparticles and IONs coated with 0.2, 0.5 and 1.0%, v/v OA concentrations are abbreviated as IONs, IONs+0.2%OA, IONs+0.5%OA and IONs+1.0%OA, respectively.

2.4. Characterization of magnetic nanoparticles

The crystal structure of the iron oxide nanoparticles was investigated by X-ray diffraction analysis (Rigaku, D/Max-B, Tokyo, Japan) using CuKα radiation at a scanning rate of 0.2°/min, from 20 to 80°. The average crystallite size was calculated based on the XRD pattern according to the Scherrer's equation (1) [21]:

$$d = 0.9\lambda/\beta \cos\theta \quad (1)$$

where d is the crystallite size, λ is the X-ray wavelength (λ=1.5405 Å), β is the full width at half maximum (fwhm) and θ is Bragg angle.

The presence of various functional groups on the surface of the iron oxide nanoparticles before and after OA coating was analyzed by Attenuated total reflection Fourier Transform Infrared (ATR-FTIR) Spectroscopy (Nicolet iS10, Thermo Scientific, USA) in the range of 1000 - 4000 cm^{-1}.

The amount of OA coatings was determined by thermogravimetric analysis (TGA) using Exstar 6000 TG/DTA 6300 (SII Nano Technology Inc., Japan). Samples were heated from 30 to 900 °C with a heating rate 10 °C/min under nitrogen atmosphere. Mass losses were quantified from the obtained thermograms.

The morphology and size of the synthesized nanoparticles were examined by using transmission electron microscopy (TEM, FEI Tecnai G_2 Spirit BioTwin, USA). The aqueous dispersions of iron oxide nanoparticles were dropped onto copper grid and the samples were dried prior to the analysis. The average sizes and size distributions of iron oxide nanoparticles were calculated from TEM images using ImageJ software (National Institute of Health, USA).

The hydrodynamic size and size distribution of the iron oxide nanoparticles were determined by dynamic light scattering (DLS) experiments using a Zetasizer Nano ZS (Malvern, UK) at room temperature.

The magnetic field dependent magnetization of iron oxide nanoparticles was measured with quantum design physical property measurement system (QD-PPMS, USA) at room temperature in the field range between $-2\ T$ and $+2\ T$.

2.5. Heating potential evaluation of iron oxide nanoparticles

Magnetic hyperthermia experiments were carried out using Easy Heat 8310 system (Ambrell, UK) with a 3.43 cm diameter (8 turns) heating coil. Cold water circulation is provided to keep the coil at ambient temperature. Bare and OA coated IONs (1-10 mg/mL) were suspended in 2.5 mL of distilled water in a glass vial and sonicated for 1-2 min to achieve homogeneous dispersions. Then, samples were placed at the center of the coil and induction heating was applied at 100 A, 312 kHz frequency during 10 min. Magnetic field strength (H) was calculated from the equation (2) given below [17]:

$$H = 1.257\, ni/L\ (Oe) \tag{2}$$

where *n* is the number of turns, *i* is the applied current and *L* is the diameter of coil in centimeters. Calculated values of magnetic field strength (H) was 295.5 Oe (equivalent to 23.51 kA/m). Temperature was measured with fiber optic temperature sensor (Neoptix, Canada).

The efficiency of the heating potential of the magnetic nanoparticles was represented by the specific absorption rate (SAR) or specific loss power (SLP), which is defined as the heating power generated per unit mass [4, 22]. The magnitude of the SAR was calculated by the equation (3) [23]:

$$SAR(W/\,\mathrm{g}) = C\,\frac{m_{sol}}{m_{mag}}\,\frac{\Delta T}{\Delta t} \tag{3}$$

where the *C* is specific heat capacity for water (*C*= 4.18 J /g . °C), m_{sol} is the mass of entire sample, m_{mag} is the mass of IONs and $\Delta T/\Delta t$ is the initial slope of the time-dependent temperature curve (from 0 to 30 s).

3. RESULTS AND DISCUSSION

3.1. X-ray diffraction

XRD patterns of bare and OA coated IONs were shown in Fig. 1. The lattice planes represented by the diffraction peak at angles of 30.36°, 35.60°, 43.51°, 57.29° and 62.96°, respectively, (220), (311), (400), (511) and (440); the planes are consistent with Fe_3O_4 pattern with a cubic structure (JCPDS card no. 01-075-0449). The position and intensity of all peaks match well with standard Fe_3O_4 diffraction [24, 25]. As expected, the diffraction peaks of IONs disturbed and peak broadening was observed as the oleic acid concentration increases (Fig. 1b-d). This pattern was the most apparent on OA concentration of 1.0% v/v (Fig. 1d). In addition, the relative peak intensities of OA coated IONs with different concentrations was lower than bare IONs. Even though the peaks were weakened due to formation of oleic acid layer on the surface of IONs, but their relating lattice planes were still represented. This suggests that oleic acid coating did not much affect the crystal structure of the iron oxide nanoparticles. In addition, XRD also provide an estimate of average crystallite sizes based on Scherrer's equation [21]. The XRD graph was fitted with multiple Gaussian peaks and most intense peak (311) was used to calculate the average crystallite size of the nanoparticles. The average crystallite sizes for bare IONs and OA coated IONs with different concentrations of 0.2, 0.5 and 1.0% v/v were calculated as 8.30, 9.30, 10.40 and 11.10 nm, respectively. OA coating slightly increased the average crystallite size of IONs. Petcharoen et al., reported that the crystallite size of IONs decreased from 16.8 nm to 13.9 nm after coating of IONs with OA concentration of 0.8%, v/v [21]. Wang et al. synthesized IONs with higher OA concentrations than used in this study and they also showed size decrease from 19.8 nm to 15.3 nm [24]. However, Soares et al. denoted that OA coating did not change the average diameter and crystalline structure of IONs [26]. Also, Wulandari et al.,2019 showed that amount of OA elevated from 1.0 to 1.5 mL, the crystal size slightly increased from 4.73 to 5.69 nm after coating IONs [27].

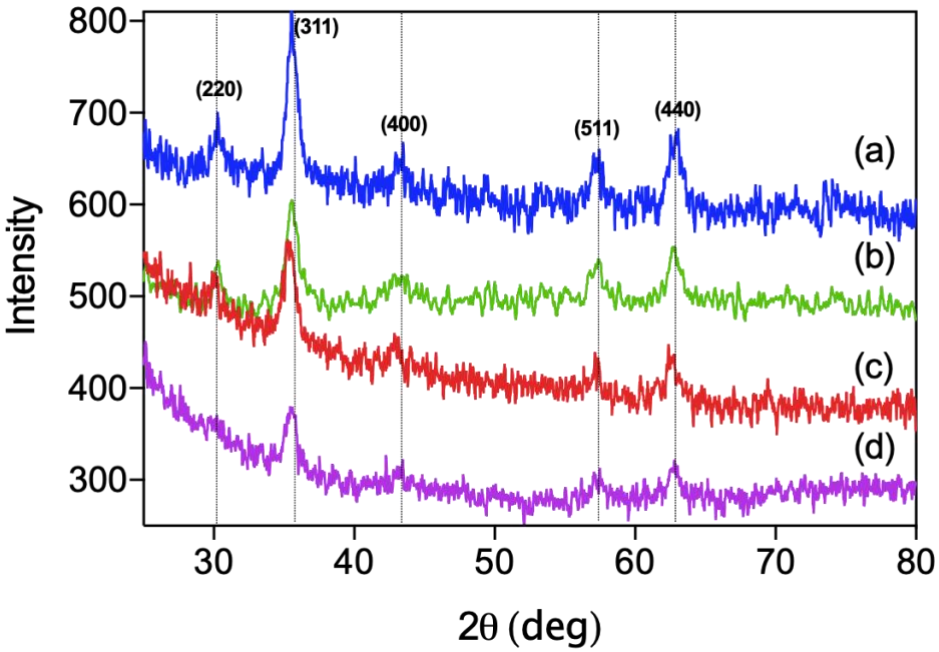

Figure 1. XRD patterns of a) IONs, b) IONs+0.2%OA, v/v c) IONs+0.5%OA, v/v and d) IONs+1.0%OA, v/v.

3.2. Infrared Spectroscopy (ATR-FTIR) analysis

The adsorption of oleic acid on the surface of IONs was determined by using ATR-FTIR spectroscopy. Fig. 2 shows the ATR-FTIR spectra of OA, bare IONs and OA coated IONs. As can be seen from Fig. 2a that pure OA shows two sharp bands at 2920 and 2855 cm^{-1} correspond to asymmetric and symmetric CH_2 stretchings, respectively. A sharp band seen at 1707 cm^{-1} corresponds to the stretching vibration of C=O and the band at 1286 cm^{-1} exhibited the presence of the C-O stretch present in OA [28-31]. Fig. 2b-d reveals the ATR-FTIR spectra obtained from the IONs coated with different concentration (0.2, 0.5, 1.0%, v/v) of OA. In a co-precipitation method, the surface of the IONs was covered by hydroxyl groups due to the synthesis accomplished in aqueous environment. Thus, the characteristic bands of the hydroxyl groups at 3357 and 1641 cm^{-1} were observed in the bare IONs (Fig. 2e). After OA coating, the displacement of asymmetric and symmetric CH_2 stretching peaks shifted to lower frequencies (2919 and 2852 cm^{-1}) for all coatings indicating the OA molecules adsorbed onto the surface of IONs (Fig. 2b-d). This means that the hydrocarbon chains surrounding the IONs were in a close-packed [29, 31-33]. The intense peak at 1707 cm^{-1} of pure oleic acid disappears in OA coated IONs and instead, the new peaks appear at 1523 and 1404 cm^{-1} correspond to asymmetric and symmetric vibrations of carboxyl group attached to Fe^{3+} ions [28, 29].

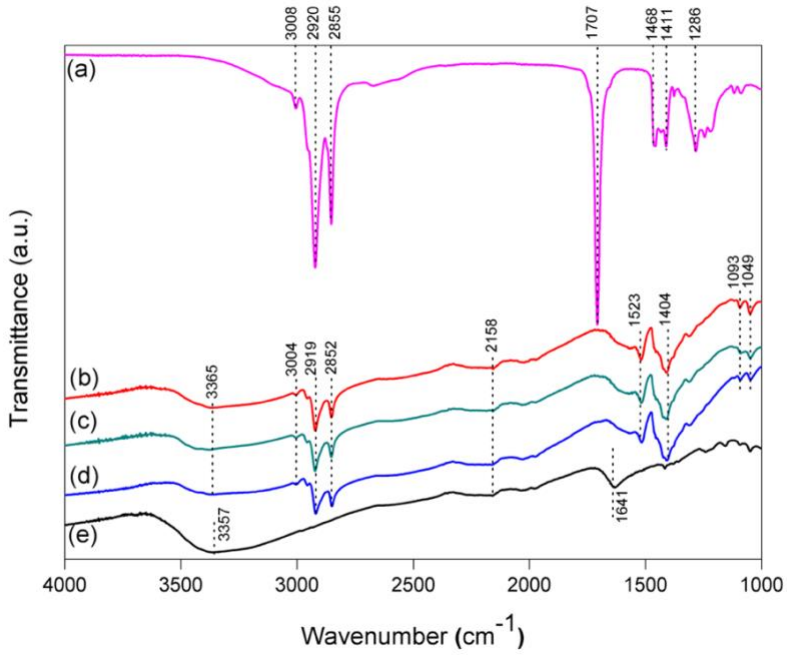

Figure 2. ATR-FTIR spectra of (a) oleic acid. (b) IONs+0.2%OA, v/v. (c) IONs+0.5%OA, v/v. (d) IONs+1.0%OA, v/v. (e) IONs.

3.3. Thermogravimetric analysis (TGA)

In order to quantify the amount of OA associated with IONs, thermogravimetric analysis was performed for bare and OA (0.2%, 0.5%, 1.0%, v/v) coated IONs from room temperature to 900 °C (Fig. 3). In general, an initial slight weight loss was reported due to evaporation of adsorbed water [21, 34]. For bare and OA coated IONs, the initial slight weight loss (1-2.5%) at temperature below 150 °C refers to the removal of moistures. The weight loss in the temperature range between 200-330 °C was attributed to removal of organic moieties from the surface of IONs as reported [35, 36]. Bare IONs showed exhibited

weight loss (2.09%) observed in the temperature range ~200-400 °C and this may be attributed to the removal of organic groups on the surface of IONs. It is reported in the literature that OA coated IONs show two prominent weight loss steps below 600 °C [21, 32]. Also, Mahdavi et al. showed four derivative mass loses in TGA curve, fourth weight loss above 742 °C is possibly due to deoxidation of FeO [37]. In our study, thermograms of different amounts of oleic acid exhibited three step weight loss. The first step (150-300 °C) is attributed to the free or loosely bound OA, while the second step (300-500 °C) may be due to OA chemically bound to IONs. The third weight loss between 500 and 750 °C was attributed to the oleic acid-coated layer. Our results (Table 1) showed that the bound OA fraction increased from 2.38 to 4.35% when the amount of OA used for capping increased from 0.2 to 1.0%, v/v.

Table 1. Results and analysis based on TGA curves (Fig. 3) of IONs.

NPs	Initial weight loss (%) (0-150 °C)	First weight loss (%) (150-300 °C)	Second weight loss (%) (300-500 °C)	Third weight loss (%) (500-750 °C)	Total Weight loss (%)
IONs (bare)	2.50	2.09 (200-400 °C)	----	----	4.59
IONs+0.2%OA	1.15	3.95	2.38	8.9	16.38
IONs+0.5%OA	2.50	3.64	3.36	8.32	17.82
IONs+1.0%OA	1.58	3.86	4.35	9.0	18.79

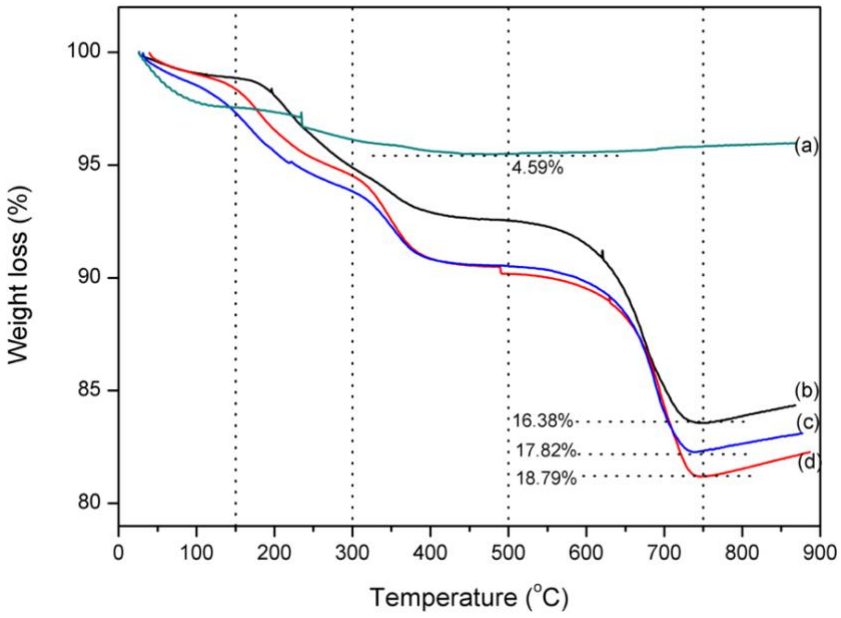

Figure 3. TGA curves of a) IONs b) IONs+0.2%OA, c) IONs+0.5%OA, d) IONs+1.0%OA.

3.4. Transmission electron microscopy (TEM) analysis

The size and the morphology of IONs were assessed by using transmission electron microscopy. TEM image of the bare IONs have a narrow size distribution with an average diameter of 8.0±1.9 nm (Fig. 4a); however, the particles tend to agglomerate. On the other hand, the IONs prepared with 0.2, 0.5 and 1.0% v/v OA concentrations have the average diameters of 9.3±2.0 nm, 8.3±1.6 nm and 10.0±2.0 nm, respectively. These results showed that OA coatings did not dramatically change the average diameters of IONs and their values were in good agreement with XRD size analyses. The morphology of the bare IONs showed irregular shape (Fig. 4a), on the other hand, IONs coated with OA changed their morphology to

spherical shape as the OA concentration increased. Moreover, IONs especially prepared in the presence of 1.0 % v/v OA were separated from its adjacent particles and adsorbed surfactant on the surface reduced agglomeration. These results suggested that IONs can be homogeneously coated with 1.0%, v/v OA and colloidal stability of IONs were improved with the OA concentration increased from 0.2 to 1.0%, v/v. Petcharoen et al. showed that the OA coating agents provided larger particle sizes due to the combination of the OA layer on the surface of magnetite. According to their SEM (scattering electron microscope) image, bare and OA (0.8%, v/v) coated magnetite nanoparticles have 15 and 27 nm average diameter, respectively [21]. Unlike the previous study, Madhavi et al. demonstrated that bare and OA (1.7%, v/v) coated Fe_3O_4 NPs sizes were 16.5 and 7.3 nm, respectively. And, bare Fe_3O_4 NPs were seriously aggregated according to TEM image [37]. It is notable that, there are many studies with different results about the effect of coating OA on the nanoparticle size.

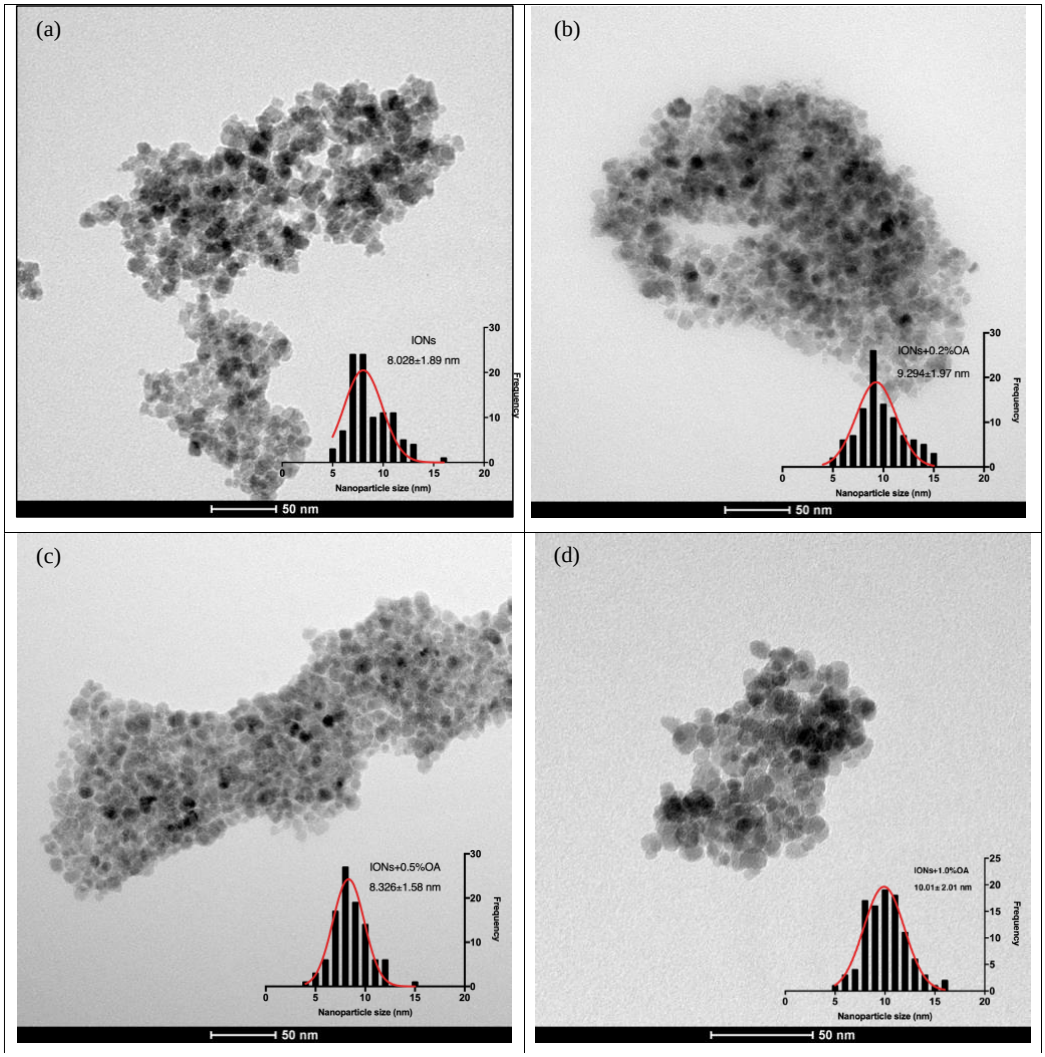

Figure 4. TEM images of a) IONs, b) IONs+0.2%OA, v/v. c) IONs+0.5%OA, v/v. d) IONs+1.0%OA, v/v. with size distribution histograms.

3.5. Dynamic light scattering (DLS) analysis

Hydrodynamic size and size distribution of the bare and OA coated IONs were measured by DLS as shown in Fig. 5. The average diameter of the bare and 0.2, 0.5 and 1.0%, v/v OA coated IONs were found

as 92.1±28.1, 92.5±36.2, 72.3±28.5 and 69.9±32.5 nm, respectively. Hydrodynamic size of the IONs decreased as the OA concentration reached to 1.0% and these data revealed that OA coatings tend to decrease the agglomeration of IONs especially in the case of OA concentration higher than 0.2%, v/v. As noted here and in the literature that hydrodynamic size dramatically differs from TEM identified static size, especially for nanoparticles [29]. In TEM images, the OA coating is not visible, therefore, the measured diameters are related to core iron oxide nanoparticles (IONs). Therefore, DLS gives the average hydrodynamic diameter rather than the actual diameter of nanoparticles [29, 38].

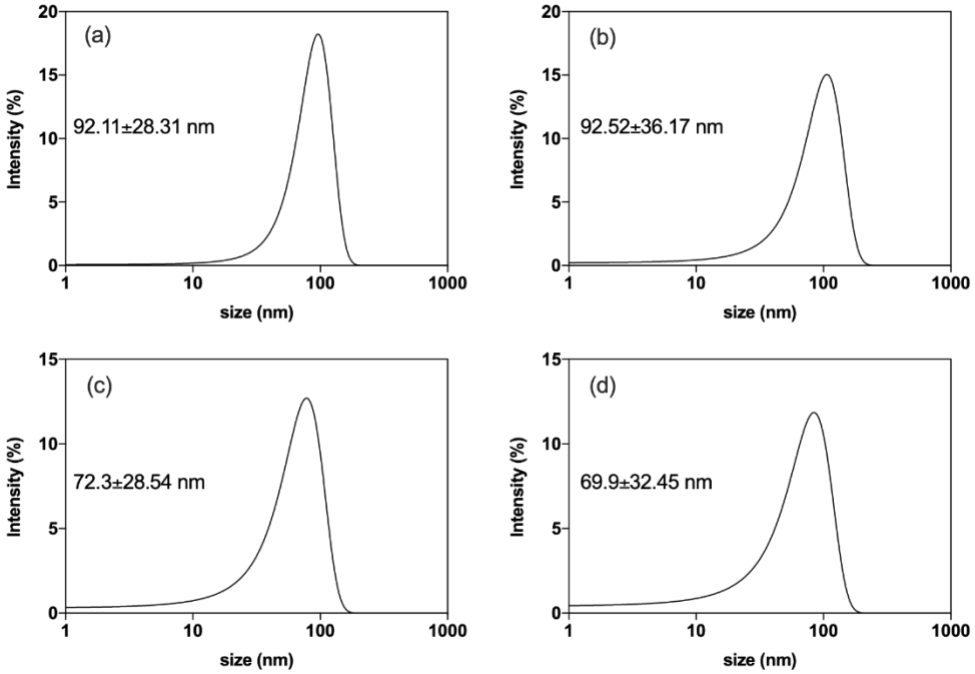

Figure 5. Particle size distribution of a) IONs, b) IONs+0.2%OA, v/v. c) IONs+0.5%OA, v/v. and d) IONs+1.0%OA, v/v. based on DLS measurements. (Data were fitted with non-linear Gaussian curve fit.)

3.6. Magnetic properties of IONs

The magnetic properties of IONs and OA coated IONs were measured at room temperature using quantum design physical property measurement system (PPMS), as shown in Fig. 6. It is clear to find that magnetization curves of all the samples exhibit superparamagnetic behavior, in which the coercivity are close to zero. The saturation magnetization for bare and 0.2, 0.5 and 1.0%, v/v OA coated IONs were 62.0, 61.5, 59.5 and 58.2 emu/g, respectively, and Ms values of the OA coated IONs did not dramatically change with increasing OA concentration. The change of magnetic properties due to the OA coating present in the literature is controversial. Petcharoen et al. showed that bare magnetite (IONs), IONs+0.8%OA, v/v and hexanoic acid coated IONs possessed 57.1, 33.3 and 58.7 emu/g, Ms values, respectively. That is, the coating layer (hexanoic acid) of IONs slightly effect (1-2 emu/g) to Ms value, but Ms value for 0.8% OA coating on IONs dramatically decreased [21]. A sharp decrease on Ms values of IONs after OA coating was also reported by other studies. Liu et al. showed that the amount of OA (2.16% v/v) decreased the Ms value of IONs from 58 emu/g to 46 emu/g [39]. Also, Tansık et al. observed that 4.5% (v/v) OA coating on IONs decreased Ms value from 62 to 55 emu/g [40]. On the other hand, Jovanovic et al. showed that OA coating on IONs did not affect Ms value up to 0.1 M, however, significant changes were observed at higher OA concentrations [41]. In this study, OA coating with different concentrations increased the colloidal stability of the IONs and did not affect the magnetic properties of the resultant nanoparticles. Therefore, these OA coated nanoparticles were found as good candidates for hyperthermia applications with these superior

properties and their heating potential and SAR values were investigated via alternating current (AC) magnetic field in subsequent heating experiments.

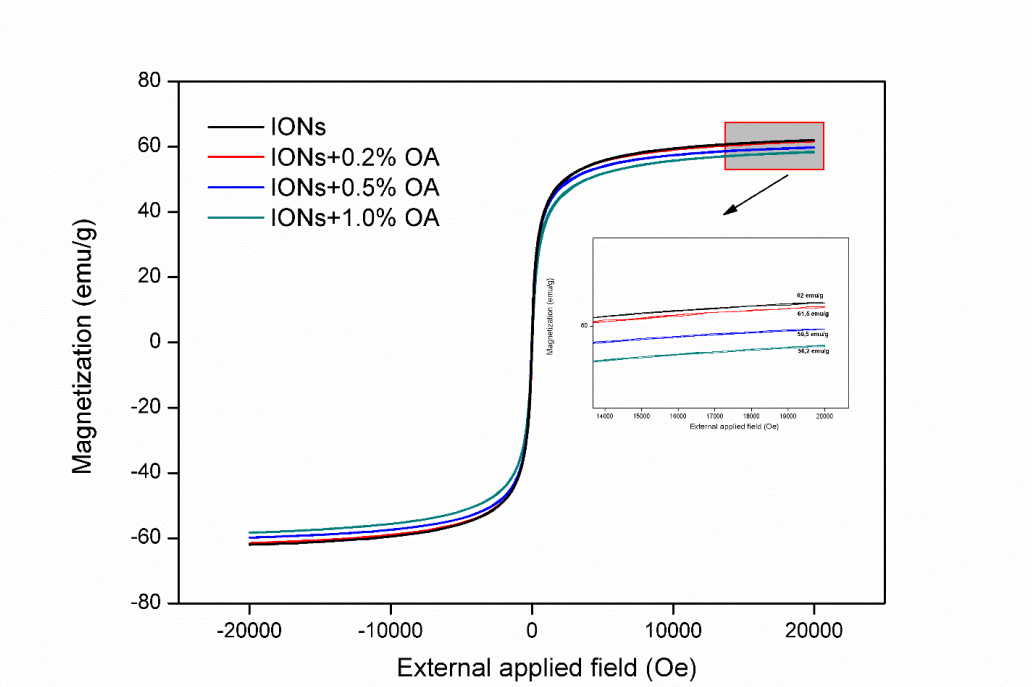

Figure 6. Magnetization (M) versus applied magnetic field (H) curve for IONs and IONs+OA (0.2%, 0.5%, 1.0%, v/v) at room temperature. Here, M is expressed in terms of emu/g.

3.7. Induction heating ability of IONs and SAR

The induction heating capabilities of bare IONs and OA coated IONs were measured after preparing their suspension in distilled water with different IONs concentrations. Figure 7a-b represents the dynamic temperature curves for IONs and IONs+1.0%OA, v/v under 100 A, 312 kHz frequency of alternating magnetic field during 10 min for different nanoparticle concentrations (1-10 mg/mL). As shown in Fig. 7a and b, 10 mg/mL of bare IONs and IONs+1.0%OA concentrations showed maximum temperature increase such as 26.7 °C and 25.2 °C, respectively. The increase of temperature has a linear relationship with the concentration of magnetic nanoparticles present in suspension medium. Thus, the temperature increase decreased as the nanoparticle concentrations was gradually lowered to 1 mg/mL. Besides, the temperature increases for IONs+0.2%OA, v/v and IONs+0.5%OA, v/v (10 mg/mL) were significantly lower than bare IONs and IONs+1.0%OA (16.4 °C and 19.0 °C, respectively) (Fig. 7c). In hyperthermia applications, the temperature of a tumor environment should reach the therapeutic temperature (41–45 °C) within few minutes [42]. In this study, the time needed for temperature to reach 45 °C from body temperature was less than 2 min for IONs and IONs+1.0%OA, v/v with concentrations higher than 5 mg/mL. Due to the insufficient colloidal stability and an extra OA layer, IONs+0.2%OA, v/v and IONs+0.5%OA, v/v samples did not show the same heating performance as compared to bare IONs and IONs+1.0%OA, v/v (Fig. 7d). Therefore, these findings suggest that OA coating with low concentrations was not sufficient to stabilize IONs in water indicating agglomeration and precipitation in the end. Our results revealed that IONs coated with 1.0% v/v OA, v/v showed similar heating performance with bare IONs and 1%, v/v found as optimum OA concentration for hyperthermia applications. SAR values reflect the magnitude of heat dissipation from NPs to surrounding medium. SAR values of bare IONs and IONs+OA (0.2%, 0.5%, 1.0%, v/v) were found as 39.50, 34.81, 23.36 and 45.98 W/g, respectively for nanoparticle concentrations of 10 mg/mL. Ghosh et al. investigated the heating effects of Fe_3O_4+OA (10%, v/v) under increasing induction heating conditions

(100-600 A) at 265 kHz for 10 min. 100 ampere (A) current was not sufficient for heating up to 42 °C for all tested IONs concentrations (2-20 mg) [17]. Jadhav et al. [34] prepared different concentrations of OA coated magnetic nanoparticles (MN-OA, ~20%, 10%, 5%, w/w) and induction heating was carried out at 400 A, 265 kHz radiofrequency for 10 min. The results revealed that MN-OA (10%, w/w) showed a maximum heating up (ΔT~23 °C). Soares et al. [16] synthesized magnetic nanoparticles coated with various OA (8%, 32%, 64%, 96%, w/w) concentrations under AC magnetic field (24 kA m^{-1}, 418.5 kHz for 10 min). Induced heating ability of 8.0% of OA coating was similar to uncoated magnetic nanoparticle, whereas the heating ability of nanoparticles dramatically decreased with OA concentrations (32%, 64%, 96%, v/v) increase. The results obtained in this study implied that low OA coatings on IONs can be successfully used for magnetic hyperthermia applications under relatively low frequency magnetic field.

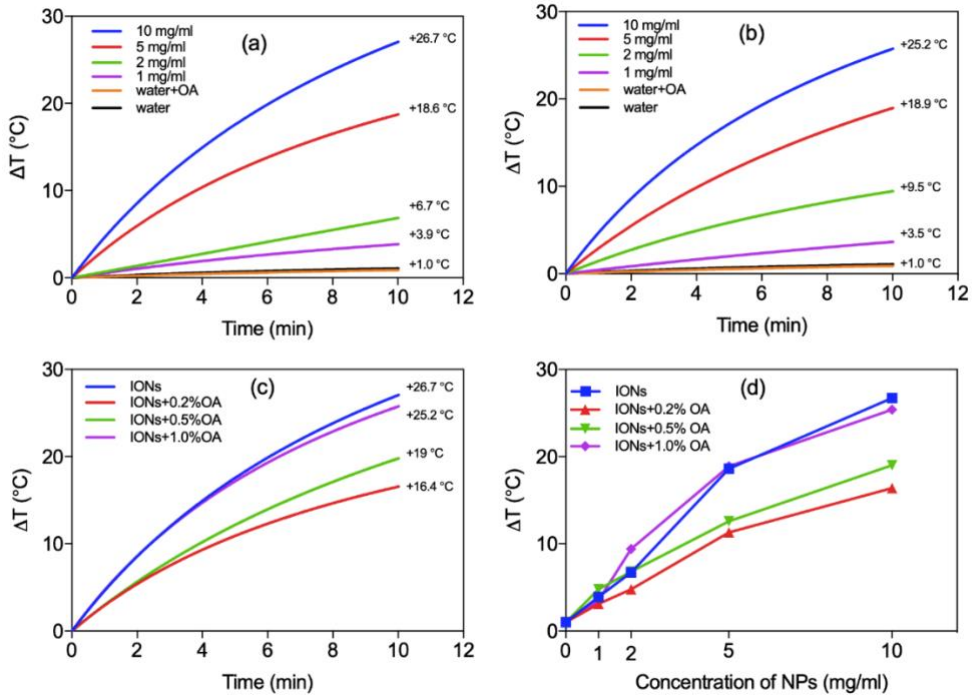

Figure 7. The time-dependent changes in the temperature of (a) IONs and (b) IONs+1.0%OA, v/v. with different IONs concentrations, c) bare IONs and IONs with different OA coatings (IONs concentration: 10 mg/mL) and d) The concentration-dependent changes in the temperature of all NPs (application time: 10 min).

4. CONCLUSION

Our results revealed that capping with 1.0%, v/v OA enhances the hyperthermia effect of IONs dramatically compared to 0.2%OA, v/v and 0.5%OA, v/v. The enhanced hyperthermia effect of IONs+1.0%OA, v/v was attributed to their high dispersion performance without formation of large agglomerates in water. IONs coated with low OA concentration can be successfully used in magnetic nano hyperthermia applications. As a result, the heating effect highly depends on physical and chemical properties of IONs, hyperthermia exposure systems, measurement conditions, nanoparticle size distributions and especially colloidal stability of IONs.

Acknowledgement

This work was supported by the Scientific and Technological Research and Technological Research Council of Turkey (TUBITAK), Grant no: SBAG-118S027. We are grateful to Dr. Mehmet Burak Kaynar for his help to the XRD, VSM and hyperthermia measurements.

REFERENCES

[1] J. Beik et al., "Nanotechnology in hyperthermia cancer therapy: From fundamental principles to advanced applications," Journal of controlled release : official journal of the Controlled Release Society, vol. 235, pp. 205-21, Aug 10 2016, doi: 10.1016/j.jconrel.2016.05.062.

[2] H. Liu et al., "Application of iron oxide nanoparticles in glioma imaging and therapy: from bench to bedside," Nanoscale, vol. 8, no. 15, pp. 7808-7826, 2016.

[3] K. El-Boubbou, "Magnetic iron oxide nanoparticles as drug carriers: Preparation, conjugation and delivery," Nanomedicine, vol. 13, no. 8, pp. 929-952, 2018.

[4] R. Wildeboer, P. Southern, and Q. Pankhurst, "On the reliable measurement of specific absorption rates and intrinsic loss parameters in magnetic hyperthermia materials," Journal of Physics D: Applied Physics, vol. 47, no. 49, p. 495003, 2014.

[5] H. A. Albarqi et al., "Biocompatible Nanoclusters with High Heating Efficiency for Systemically Delivered Magnetic Hyperthermia," ACS Nano, vol. 13, no. 6, pp. 6383-6395, Jun 25 2019, doi: 10.1021/acsnano.8b06542.

[6] A. E. Deatsch and B. A. Evans, "Heating efficiency in magnetic nanoparticle hyperthermia," Journal of Magnetism and Magnetic Materials, vol. 354, pp. 163-172, 2014, doi: 10.1016/j.jmmm.2013.11.006.

[7] W. Xie et al., "Shape-, size-and structure-controlled synthesis and biocompatibility of iron oxide nanoparticles for magnetic theranostics," Theranostics, vol. 8, no. 12, p. 3284, 2018.

[8] M. Cano et al., "Partial PEGylation of superparamagnetic iron oxide nanoparticles thinly coated with amine-silane as a source of ultrastable tunable nanosystems for biomedical applications," Nanoscale, vol. 9, no. 2, pp. 812-822, Jan 5 2017, doi: 10.1039/c6nr07462f.

[9] M. Liu et al., "Synthesis of magnetic molecularly imprinted polymers for the selective separation and determination of metronidazole in cosmetic samples," Anal Bioanal Chem, vol. 407, no. 13, pp. 3875-80, May 2015, doi: 10.1007/s00216-015-8592-7.

[10] F. Shubitidze, K. Kekalo, R. Stigliano, and I. Baker, "Magnetic nanoparticles with high specific absorption rate of electromagnetic energy at low field strength for hyperthermia therapy," J Appl Phys, vol. 117, no. 9, p. 094302, Mar 7 2015, doi: 10.1063/1.4907915.

[11] L. Xie, W. Jin, H. Chen, and Q. Zhang, "Superparamagnetic Iron Oxide Nanoparticles for Cancer Diagnosis and Therapy," J Biomed Nanotechnol, vol. 15, no. 2, pp. 215-416, Feb 1 2019, doi: 10.1166/jbn.2019.2678.

[12] J. Cai, Y. Q. Miao, B. Z. Yu, P. Ma, L. Li, and H. M. Fan, "Large-Scale, Facile Transfer of Oleic Acid-Stabilized Iron Oxide Nanoparticles to the Aqueous Phase for Biological Applications," Langmuir, vol. 33, no. 7, pp. 1662-1669, Feb 21 2017, doi: 10.1021/acs.langmuir.6b03360.

[13] L. H. Reddy, J. L. Arias, J. Nicolas, and P. Couvreur, "Magnetic nanoparticles: design and characterization, toxicity and biocompatibility, pharmaceutical and biomedical applications," Chemical reviews, vol. 112, no. 11, pp. 5818-5878, 2012.

[14] R. Gupta et al., "Effect of Oleic Acid Coating of Iron Oxide Nanoparticles on Properties of Magnetic Polyamide-6 Nanocomposite," JOM, vol. 71, no. 9, pp. 3119-3128, 2019.

[15] C. W. Lai, F. W. Low, M. F. Tai, and S. B. Abdul Hamid, "Iron oxide nanoparticles decorated oleic acid for high colloidal stability," Advances in Polymer Technology, vol. 37, no. 6, pp. 1712-1721, 2018.

[16] P. I. Soares et al., "Iron oxide nanoparticles stabilized with a bilayer of oleic acid for magnetic hyperthermia and MRI applications," Applied Surface Science, vol. 383, pp. 240-247, 2016.

[17] R. Ghosh et al., "Induction heating studies of Fe3O4 magnetic nanoparticles capped with oleic acid and polyethylene glycol for hyperthermia," Journal of Materials Chemistry, vol. 21, no. 35, 2011, doi: 10.1039/c1jm10092k.

[18] R. Araújo-Neto et al., "Monodisperse sodium oleate coated magnetite high susceptibility nanoparticles for hyperthermia applications," J Magn Magn Mater, vol. 364, pp. 72-79, 2014.

[19] S. Sánchez-Cabezas, R. Montes-Robles, J. Gallo, F. Sancenón, and R. Martínez-Máñez, "Combining magnetic hyperthermia and dual T 1/T 2 MR imaging using highly versatile iron oxide nanoparticles," Dalton Transactions, vol. 48, no. 12, pp. 3883-3892, 2019.

[20] R. Massart, "Preparation of aqueous magnetic liquids in alkaline and acidic media," IEEE transactions on magnetics, vol. 17, no. 2, pp. 1247-1248, 1981.

[21] K. Petcharoen and A. Sirivat, "Synthesis and characterization of magnetite nanoparticles via the chemical co-precipitation method," Materials Science and Engineering: B, vol. 177, no. 5, pp. 421-427, 2012, doi: 10.1016/j.mseb.2012.01.003.

[22] C. Iacovita et al., "Small versus large iron oxide magnetic nanoparticles: hyperthermia and cell uptake properties," Molecules, vol. 21, no. 10, p. 1357, 2016.

[23] I. Hilger, K. Frühauf, W. Andrä, R. Hiergeist, R. Hergt, and W. A. Kaiser, "Heating potential of iron oxides for therapeutic purposes in interventional radiology," Academic radiology, vol. 9, no. 2, pp. 198-202, 2002.

[24] F. Wang et al., "Synthesis and characterization of superparamagnetic Fe3O4 nanoparticles modified with oleic acid," Integrated Ferroelectrics, vol. 153, no. 1, pp. 92-101, 2014.

[25] Q. Zhang, C. Wang, L. Qiao, H. Yan, and K. Liu, "Superparamagnetic iron oxide nanoparticles coated with a folate-conjugated polymer," Journal of Materials Chemistry, vol. 19, no. 44, pp. 8393-8402, 2009.

[26] P. I. Soares et al., "Effects of surfactants on the magnetic properties of iron oxide colloids," J Colloid Interface Sci, vol. 419, pp. 46-51, Apr 1 2014, doi: 10.1016/j.jcis.2013.12.045.

[27] I. O. Wulandari, H. Sulistyarti, A. Safitri, D. J. H. Santjojo, and A. Sabarudin, "Development of synthesis method of magnetic nanoparticles modified by oleic acid and chitosan as a candidate for drug delivery agent," Journal of Applied Pharmaceutical Science, vol. 9, no. 07, pp. 001-011, 2019.

[28] K. S. Sharma et al., "Synthesis and characterization of monodispersed water dispersible Fe3O4 nanoparticles and in vitro studies on human breast carcinoma cell line under hyperthermia condition," Sci Rep, vol. 8, no. 1, p. 14766, Oct 3 2018, doi: 10.1038/s41598-018-32934-w.

[29] J. Ibarra et al., "Synthesis and characterization of magnetite/PLGA/chitosan nanoparticles," Materials Research Express, vol. 2, no. 9, 2015, doi: 10.1088/2053-1591/2/9/095010.

[30] L. Zhang, R. He, and H.-C. Gu, "Oleic acid coating on the monodisperse magnetite nanoparticles," Applied Surface Science, vol. 253, no. 5, pp. 2611-2617, 2006, doi: 10.1016/j.apsusc.2006.05.023.

[31] N. Wu, L. Fu, M. Su, M. Aslam, K. C. Wong, and V. P. Dravid, "Interaction of fatty acid monolayers with cobalt nanoparticles," Nano letters, vol. 4, no. 2, pp. 383-386, 2004.

[32] K. Yang, H. Peng, Y. Wen, and N. Li, "Re-examination of characteristic FTIR spectrum of secondary layer in bilayer oleic acid-coated Fe3O4 nanoparticles," Applied Surface Science, vol. 256, no. 10, pp. 3093-3097, 2010, doi: 10.1016/j.apsusc.2009.11.079.

[33] L. N. Okassa et al., "Optimization of iron oxide nanoparticles encapsulation within poly(d,l-lactide-co-glycolide) sub-micron particles," Eur J Pharm Biopharm, vol. 67, no. 1, pp. 31-8, Aug 2007, doi: 10.1016/j.ejpb.2006.12.020.

[34] N. V. Jadhav et al., "Synthesis of oleic acid functionalized Fe3O4 magnetic nanoparticles and studying their interaction with tumor cells for potential hyperthermia applications," Colloids Surf B Biointerfaces, vol. 108, pp. 158-68, Aug 1 2013, doi: 10.1016/j.colsurfb.2013.02.035.

[35] G. Sharma and P. Jeevanandam, "Synthesis of self-assembled prismatic iron oxide nanoparticles by a novel thermal decomposition route," RSC Adv., vol. 3, no. 1, pp. 189-200, 2013, doi: 10.1039/c2ra22004k.

[36] Z. Shan, W.-S. Yang, X. Zhang, Q.-M. Huang, and H. Ye, "Preparation and characterization of carboxyl-group functionalized superparamagnetic nanoparticles and t he potential for bio-applications," Journal of the Brazilian Chemical Society, vol. 18, no. 7, pp. 1329-1335, 2007.

[37] M. Mahdavi et al., "Synthesis, surface modification and characterisation of biocompatible magnetic iron oxide nanoparticles for biomedical applications," Molecules, vol. 18, no. 7, pp. 7533-48, Jun 27 2013, doi: 10.3390/molecules18077533.

[38] S. Prabha, W.-Z. Zhou, J. Panyam, and V. Labhasetwar, "Size-dependency of nanoparticle-mediated gene transfection: studies with fractionated nanoparticles," Int J Pharmaceut, vol. 244, no. 1-2, pp. 105-115, 2002.

[39] X. Liu, M. D. Kaminski, Y. Guan, H. Chen, H. Liu, and A. J. Rosengart, "Preparation and characterization of hydrophobic superparamagnetic magnetite gel," Journal of magnetism and magnetic materials, vol. 306, no. 2, pp. 248-253, 2006.

[40] G. Tansık, A. Yakar, and U. Gündüz, "Tailoring magnetic PLGA nanoparticles suitable for doxorubicin delivery," Journal of nanoparticle research, vol. 16, no. 1, p. 2171, 2014.

[41] S. Jovanović, M. Spreitzer, M. Tramšek, Z. Trontelj, and D. Suvorov, "Effect of oleic acid concentration on the physicochemical properties of cobalt ferrite nanoparticles," The Journal of Physical Chemistry C, vol. 118, no. 25, pp. 13844-13856, 2014.

[42] T.-C. Lin, F.-H. Lin, and J.-C. Lin, "In vitro feasibility study of the use of a magnetic electrospun chitosan nanofiber composite for hyperthermia treatment of tumor cells," Acta biomaterialia, vol. 8, no. 7, pp. 2704-2711, 2012.

DOI: 10.38061/idunas.632709

IDUNAS	NATURAL & APPLIED SCIENCES JOURNAL	2019 Vol. 2 No. 2 (30-37)

Comparison of CNN and SVM in detection of activation in malaria cell images

Research Article

Jale BEKTAŞ [1*]

[1] Mersin University, School of Applied Technology And Management Of Erdemli, Department of Computer Technology and Information Systems, Erdemli, Mersin, TURKEY

Author E-mail:
bektasjale@mersin.edu.tr
Tel: +90 324 361 00 01
Fax: + +90 324 361 00 73
*Correspondence to: J. Bektaş, Mersin University, School of Applied Technology And Management Of Erdemli, Department of Computer Technology and Information Systems, Erdemli, Mersin, TURKEY
DOI: 10.38061/idunas.632709

Received: October 14, 2019; Accepted: December 31, 2019

Abstract

Malaria is a disease caused by parasites that are transmitted through the enzymes of Anophele mosquito and cause symptoms in fatal danger. Thick and thin film microscopic examination of smears taken from blood is the most reliable method for diagnosis. In the manual examination of the smears, the expertise of the examiner and the quality of the smear significantly affect the accuracy of the diagnosis. Pattern recognition, classification techniques on blood smear images of Malaria and Malaria automatic diagnosis are among the subjects of research. In this study, Convolutional Neural Networks including InceptionV3, GoogLeNet, AlexNet, Resnet50, Vgg16 networks by using six-fold cross validation were applied and performance evaluations were performed with Support Vector Machine (SVM) which is a Machine Learning method. Support Vector Machine. It was found out that Deep Learning methods achieved at least 9.43% of accuracy difference performance compared to SVM method based on the features of the input sample images. This difference was 0.08 for F-Score and 0.16 for Youden's index.

Keywords: classification, convolutional neural network, support vector machines, Pattern recognition

1.INTRODUCTION

Malaria is an infectious disease caused by the infection of erythrocytes by Plasmodium parasites, in which female anopheles mosquitoes carrying parasites inoculate humans during feeding. Since the treatment of malaria patients varies according to the detected Plasmodium species, it is extremely important to distinguish Plasmodium species in the diagnosis of malaria. The most widely used method in the microbiological diagnosis of malaria all over the world is to examine the preparations prepared by staining the blood taken from the fingertip of patient under a light microscope (Who, 2019). Thick smear and thin smear in this examination made by diagnosis of plasmodium infected or non-infected is diagnosed. When investigating the presence of parasites with thick drops, the species causing infection by fine smear is

identified. Support can be obtained from pathology departments in terms of species separation. Malaria can be treated if appropriate diagnostic and therapeutic methods are used, but alternative solutions can be produced by machine learning Since rapid diagnostic methods are expensive and underdeveloped areas are affected by the disease alternative solutions get more attraction.

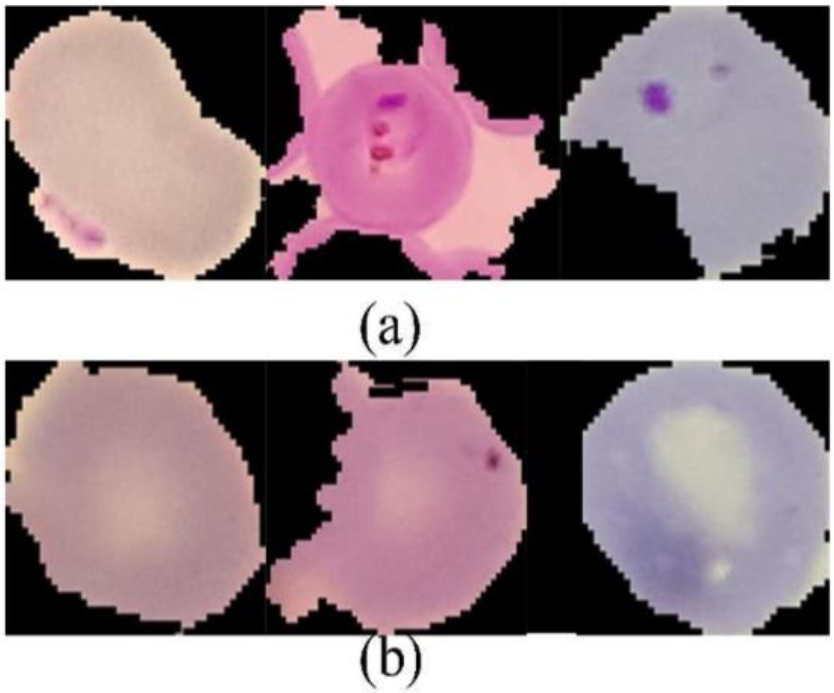

Figure 1. Red blood sample images. (a) the top three images are parasitized.(b) bottom three images are uninfected samples.

There are several studies which were applied to both thick and thin blood smear images by using machine learning methods. Support Vector Machines (SVM) and Multilayer Perceptron neural network (MLP) are used for quantification of infected erythrocytes in thin blood films as well as a precise determination of their infection stage in (Diaz, et al., 2009). Bayesian classifier and SVM are used for automated detection of malaria infected erythrocyte images using light microscopy and 84% of accuracy is achieved with bayesian learning (Das, et al., 2013). In another study, to classify all features on malaria parasites in thin blood smear MLP method is used and achieves accuracy of 87.8% (Nugroho, et al., 2015). Backpropagation feed forward neural network is used with image processing techniques to distinguish parasite infected images from non-infected blood images by segmenting and classfying respectively (Ahirwar, et al., 2012). The Hessian based edge detection filter is used to segment red blood cells and decision tree is used for malaria parasite classification and viability quantification (Moon, et al., 2013). Authors in (Prasad, et al., 2012) developed a decision support system for malaria parasite detection. In addition to this a mobile application has been developed which provides expert support offline.

Deep learning researchs have been a rising trendy subject with the routine methods on images and videos. The capabilities of particularly designed transfer learning paradigms, convolutional neural networks (CNN) have been very popular on pattern recognition and image classification. CNN network with 16-layers is used for analysing images for malaria diagnosis by comparing the network with AlexNet-SVM transfer learning implementation (Liang, et al., 2016). Another work compares transfer learning methods such as AlexNet, GoogleNet, LeNet with SVM and compares the performances for diagnosis of malaria (Dong, et al., 2017). Red blood cell detection and segmentation problems are examined by using malaria image

acquisition techniques by comparing with approximately 50 image processing and classification techniques (Poostchi, et al., 2018).

In this work, five CNN networks such as AlexNet, VGG16, InceptionV3, GoogleNet, ResNet50 are used for detecting infected malaria red blood cells. The selected state-of-the-art networks are used in different studies particularly. They have different architectures of depth, and when the parameters are optimized, there is a variety in which we can measure its impact in comparison. CNN networks are compared with SVM which is one of the most popular image recognition and classification machine learning algorithm. SVM is applied by using HOG method to extract the features of the images and two kernel selection options in the classification stage are tried.

2. EXPERIMENTAL SECTION

2.1. Convolutional Neural Networks

Basically, it is a Deep Learning model that uses the standard Neural Network to solve the classification problem but uses other layers to identify information and identify certain features. Such neural networks, first performed by Yann LeCun in 1990, became widespread after 2012 (Krizhevsky, et al., 2012).

In CNNs a filter is indicated by a vector. The filter allows us to measure how much an input segment looks like a property. The image classification process takes an input image and determines the probability that it is in a predetermined class as output. RGB images such any of size 480X480 will be represented by a series of 480X480X3 pixels and each number in that sequence will be identified by a number between 0-255 representing the pixel density at that point. As a result, when training the CNN an image is taken, passed through a series of nonlinear, convolutional, size-reducing and fully connected layers. The output that will give a class or probability for this input is obtained (LeCun, et al., 2010). Fig.2. shows an example of the layer hierarchy and ordering in any CNN networks. Network architecture begins with an input layer and finalised with a fully connected layer. Classification is performed via Softmax. The weights on which layers should not be used and the adjustment on the output layer are explained in detail in Section 2.1.1.

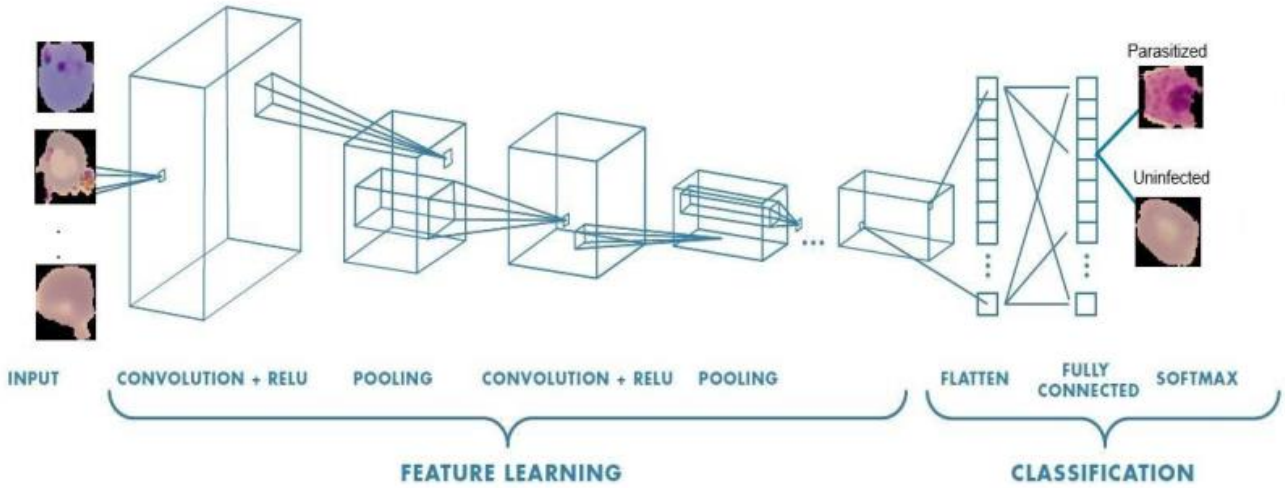

Figure 2. CNN Network Architecture

Transfer learning is a machine learning technique in which a model trained for a task is redesigned in a related second task and an optimization that provides rapid progress or improved performance in modeling is the second task. To construct a new CNN network using Malaria dataset which has the compilation of 27558 images can take up to a number of weeks. However, training the state-of-the-art networks with pre-trained weights can speed up the learning process. For this reason, the use of state- of-the-art network

architectures are practical and responsive for classification with pretrained weight values in specific layers. Some of networks which were used in this study are shown in Table 1.

Table 1. Properties of CNN Networks

CNN Architecture	Year	Layers Deep	Input Size	Developed by
AlexNet	2012	8	227x227	Alex K et al
VGGNet	2014	16	224x224	Simonyan, Zisserman
GoogleNet	2014	22	224x224	Google
Inception V3	2015	42	299x299	Szegedy et al.
ResNet	2015	50	224x224	Kaiming He

2.1.1. Parameters of Networks

Network architectures at different depths may react differently depending on the nature of the dataset to which it is applied. Therefore, some changes must be made to the input dataset before each application and its parameters must be optimized. In this study, The Malaria image dataset is re-organized according to the image size required by the classifiers as an initial step. While input dataset pixel sizes for VGGNet and ResNet is resized to 224X224, GoogLeNet, InceptionV3 and AlexNet are resized to 227X227.

After the input image set is presented to the networks, they are progressed to the classifier layer in line with the architecture. Some arrangements are made in the architecture. In this respect:

- The Fully Connected Layer is re-arranged according to the Class Number; and the Connected Class Layer is re-arranged for Binary Output (not according to the 1000-class).
- According to the transfer learning strategy, pre-trained weight values are loaded. However, since the networks are conducted on object recognition, the weight values of the first four layers are frozen. In this way, the dominant effects for the general characteristics of the images on the network are avoided. Classification of skin lesions may be more specific only by training of the last layers.
- The connections between the layers are created again.
- 10 -6 learning rate and 0.9 momentum value is used.
- 6-fold cross validation is executed.

2.2. Support Vector Machines (SVM)

Linear kernel applications of SVM are very common and can be integrated with other machine learning algorithms that can result in having both good interpolation ability (Bektaş & Ibrikçi, 2017). However, instead of making linear kernel mixture, Radial based functions (RBF) and polynomial kernel usages are considerably popular among other kernels. SVM has a very powerfull potential for approximation of kernels such as RBF and polynomial kernel functions with their estimated optimised parameters to analyze and classify image set (Kavzoglu & Colkesen, 2009; Ring & Eskofier, 2016). In these kernels, training samples in R N are seperated by hyperplane which are considered to be preassigned to two classes A or B.

Mathematically notation of SVM is $K(x_i, x_j) = \varphi(x).\varphi(x_j)$ which is identified as kernel functions. RBF is easy to apply and may be faster among all kernel functions. Whenever mathematical notation is seeming to be easy, when kernel dimension (γ) increases the process of algorithm to be more complicated. For a RBF kernel SVM, the function is,

$$e^{-\gamma\|(x-xi)\|^2} \quad (1)$$

Evaluated for each x_i.

For the RBF kernel, the *C* parameter was varied from 0.1 to 2 with increment steps of 0.1. For the Polynomial kernel, d parametes is considered as important. In this study, 2 for *d* is given for Malaria image set classification. Polynomial kernel function is given in Eq.2.

$$\frac{((x.y)+1)^d}{\sqrt{((x.x)+1)^d((y.y)+1)^d}} \quad (2)$$

Selection of the best parameters was carried out through a 6- fold cross validation and performed for every parameter combination.

2.2.1. HOG Feature Extraction Method

SVM needs a feature extracture when used in image classification. In this study, Histogram of Oriented Gradients (HOG) feature extraction method is preferred because of its capabilities on object detection (Lin, et al., 2011). HOG divides an image into small square cells, calculates the histogram of directed gradients in each cell and focuses on shape information within each patch. Block-shaped pattern supports the normalization process, and finally and identifier is obtained for each cell. In experiments, the best performance of SVM classifier is obtained with 4X4 cell size of HOG. Training samples with different cell sizes are given in Figure 3.

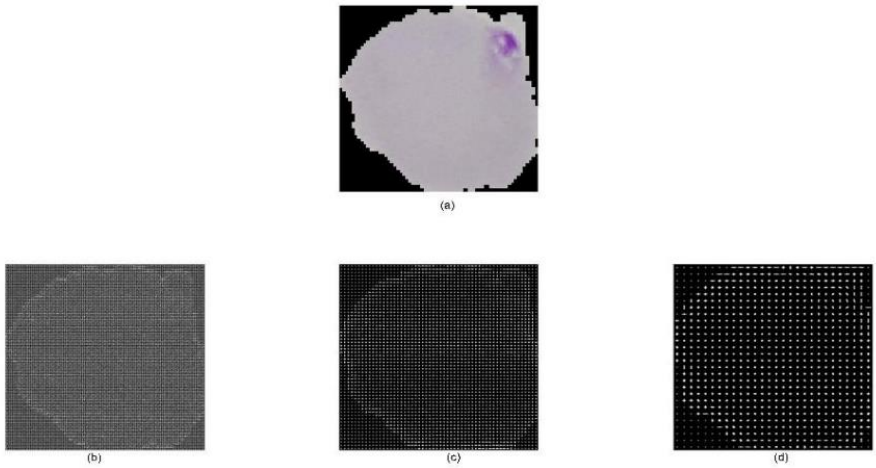

Figure 3. (a)Parasitized sample original image. (b) 2X2 ell Size with 443556 training features. (c) 4X 4 Cell size with 108900 training samples. (d) 8X8 Cell size with 26244 training samples.

2.3. Malaria Cell Images Dataset Compilation for Training

The dataset is from collections found at the National Library of Medicine and the National Institutes of Health. Whole images consist of segmented cells from the thin blood smear slide images from the Malaria Screener research activity and available from (U.S. National Library). Sample folder contains two subfolder, while Parasitized has 13779 infected thin blood smear images uninfected has 13779 images. Ratio of two classes samples is 1:1. Malaria Cell Images Dataset can be download from https://www.kaggle.com/iarunava/cell-images-for-detecting-malaria. The image compilation dataset consists of segmented images, so no preprocessing operation is performed.

3. RESULTS AND DISCUSSION

The state-of-the-art networks are constructed on ImageNet dataset and based on object recognition concept. Unlike 1000-class output label structure of imagenet Dataset, the dataset used in this study has 2 classes, which required a class number adjustment in Softmax Layer.

Transfer learning is used for all five CNN's using 6-fold cross validation method. Loss functions are given for the networks in Figure 4. which have the highest performance-lowest performance. GoogleNet converged at the 20 th epoch and seems to be same. For InceptionV3, the error tends to fall until the last iteration. As the number of layers was less such as 22 layers of deep for GoogleNet, there was a possibility of overfitting depending on the number of samples being trained. No doubt larger size networks requires longer computational time, unfortunately long training-validation times may not result in good performance. We can observe this in Resnet50 results in Table 2. Although it is thenetwork with the maximum depth of 50 layers in the study, there is a ratio of 5.46 between the best results which is InceptionV3.

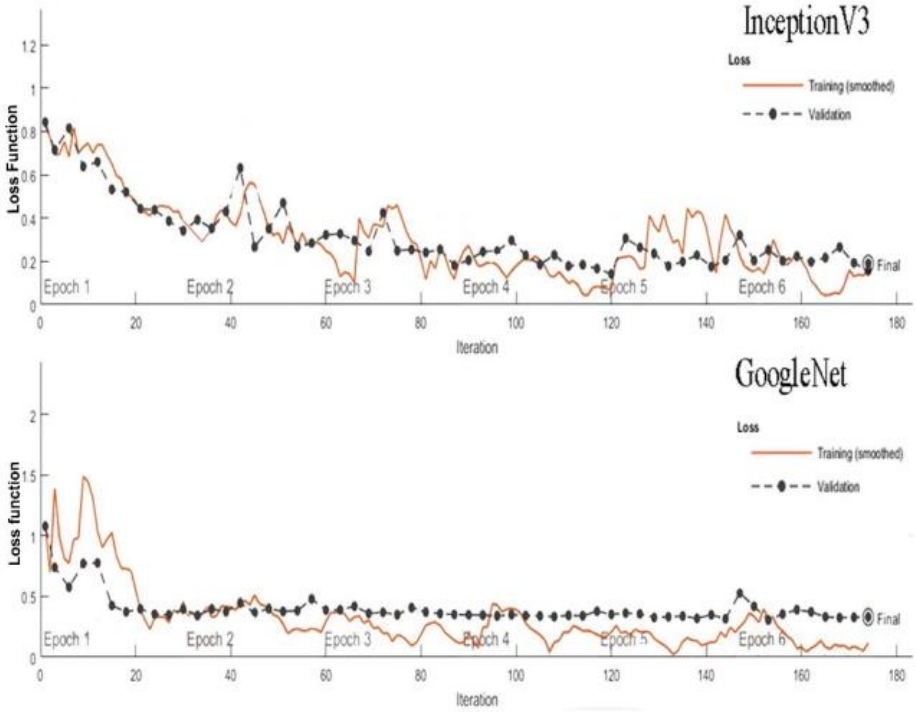

Figure 4. The loss functions of the lowest performed network GoogleNet and highest performed network InceptionV3.

After the validation, the CNNs are tested. As for the results InceptionV3 outperformed other models with the accuracy of 96.09% and the F-Score of 0.97%. SVM placed the 6th and 7th with two kernel selections between other methods which is shown in Table 2. SVM with polynomial kernel outperformed by a small margin SVM with RBF kernel with about 0.4% improvement. SVM algorithm is analyzed on MATLAB environment for feature learning and classification. Nevertheless, SVM far behind the CNNs.

Table 2. Performance metrics of individual models.

Model	Accuracy	Sen	Spec	LR +	Youden's index	F-Score	ErrRate	Process Time
Inceptionv3	96.09	0.96	0.92	12	0.88	0.97	0.031	29017
AlexNet	93.75	0.93	0.95	18.6	0.88	0.94	0.062	330
Vgg16	92.97	0.92	0.94	15.33	0.86	0.93	0.07	2598
Resnet50	90.63	0.98	0.8	4.9	0.78	0.92	0.09	38439
GoogleNet	89.06	0.9	0.87	6.92	0.77	0.9	0.1	774
SVM (polynomial)	86.50	0.88	0.84	5.51	0.72	0.89	0.14	4400
SVM (RBF)	86.01	0.88	0.83	5.18	0.71	0.85	0.17	4200

The performance of the models are evaluated with metrics including accuracy, ACC, Sen, Spec, LR+, Youden's index, F-Score, ErrorRate, Process Time(seconds).

4. CONCLUSION

Many studies have been performed in the past for diagnosis over malaria cell blood images and machine learning methods have been evaluated on different image sets in each study. The dataset which is used in this study is from collections found at the National Library of Medicine and the National Institutes of Health. Whole images consist of segmented cells from the thin blood smear slide images from the Malaria Screener research activity and available from (U.S. National Library). Ratio of two classes samples is 1:1, so 1:1 ratio and 1000 samples were selected for each class and used for train. . The state-of-the-art CNN networks have different depth architectures, and when the parameters are optimized, there is a variety in which we can measure its impact in comparison. Parameters of the networks are optimized, and CNN networks are compared with SVM which is one of the most popular image recognition and classification machine learning algorithms. Simulation results showed that high recognition accuracy and F-Score could be achieved by CNN's with very small parameter adjustments. We have demonstrated that deep learning techniques have achieved better results than SVM, which is one of the best classifiers in image recognition.

REFERENCES

Ahirwar, N., Pattnaik, S., & Acharya, B., Advanced image analysis based system for automatic detection and classification of malarial parasite in blood images. International Journal of Information Technology and Knowledge Management, 5(2012), pp.59-64.

Bektaş, J., Ibrikci, T., Hybrid classification procedure using SVM with LR on two distinctive datasets, In Proceedings of the 6th International Conference on Software and Computer Applications, Bangkok, Thailand, February 26 - 28, 2017, pp. 68-71, ACM.

Das, D. K., Ghosh, M., Pal, M., Maiti, A. K., & Chakraborty, C., Machine learning approach for automated screening of malaria parasite using light microscopic images. Micron, 45(2013), pp.97-106.

Díaz, G., González, F. A., & Romero, E., A semi-automatic method for quantification and classification of erythrocytes infected with malaria parasites in microscopic images. Journal of Biomedical Informatics, 42((2009), pp.296-307.

Dong, Y., Jiang, Z., Shen, H., Pan, W. D., Williams, L. A., Reddy, V. V., et.al, Evaluations of deep convolutional neural networks for automatic identification of malaria infected cells, In 2017 IEEE EMBS International Conference on

Biomedical & Health Informatics (BHI), 16-19 Feb. 2017, Orlando, FL, USA, pp. 101-104, IEEE.

Kavzoglu, T., & Colkesen, I., A kernel functions analysis for support vector machines for land cover classification. International Journal of Applied Earth Observation and Geoinformation, 11(2009), pp.352-359.

Krizhevsky, A., Sutskever, I., Hinton, G. E., Imagenet classification with deep convolutional neural networks, In Advances in neural information processing systems, (2012), pp.1097-1105.

LeCun, Y., Kavukcuoglu, K., Farabet, C., Convolutional networks and applications in vision, In Proceedings of 2010 IEEE International Symposium on Circuits and Systems, 30 May-2 June 2010 ,Paris, France, pp. 253-256, IEEE, 10.1109/ISCAS.2010.5537907.

Liang, Z., Powell, A., Ersoy, I., Poostchi, M., Silamut, K., Palaniappan, K., et.al, CNN-based image analysis for malaria diagnosis, In 2016 IEEE International Conference on Bioinformatics and Biomedicine (BIBM), 15-18 December 2016, Shenzhen, China, pp. 493-496, IEEE.

Lin, Y., Lv, F., Zhu, S., Yang, M., Cour, T., Yu, K., ... & Huang, T., Large-scale image classification: fast feature extraction and svm training, In CVPR 2011, June 2011, pp. 1689-1696, IEEE.Moon, S., Lee, S., Kim, H., Freitas-Junior, L. H., Kang, M., Ayong, L., & Hansen, M. A., An image analysis algorithm for malaria parasite stage classification and viability quantification. PloS one, 8(2013), e61812.

Nugroho, H. A., Akbar, S. A., & Murhandarwati, E. E. H., Feature extraction and classification for detection malaria parasites in thin blood smear, In 2015 2nd International Conference on Information Technology, Computer, and Electrical Engineering (ICITACEE), October 2015, Indonesia, pp.197-201,
IEEE.

Poostchi, M., Silamut, K., Maude, R. J., Jaeger, S., Thoma, G., Image analysis and machine learning for detecting malaria, Translational Research, 194 (2018), pp.36-55.

Prasad, K., Winter, J., Bhat, U. M., Acharya, R. V., & Prabhu, G. K., Image analysis approach for development of a decision support system for detection of malaria parasites in thin blood smear images. Journal of digital imaging, 25 (2012), pp.542-549.

Ring, M., Eskofier, B. M., An approximation of the Gaussian RBF kernel for efficient classification with SVMs, Pattern Recognition Letters, 84(2016), pp.107-113.

U.S. National Library of MedicineLister Hill National Center for Biomedical Communications, Accessed on (https://lhncbc.nlm.nih.gov/publication/pub9932)
.
World Health Organisation, https://www.who.int/malaria/areas/diagnosis/en/ "MalariaDiagnostic testing"

DOI: 10.38061/idunas.629389

IDUNAS	NATURAL & APPLIED SCIENCES JOURNAL	2019 Vol. 2 No. 2 (38-50)

Synthesis, Characterization, Antimalarial and Antimicrobial activities of Mixed Ibuprofen-Pyrimethamine M(II) Complexes [M = Cd, Co, Zn, Mn]

Research Article

Mercy O. Bamigboye[1*], Ikechukwu P. Ejidike[2]

[1] *Department of Industrial Chemistry, Faculty of Physical Sciences, University of Ilorin, P.M.B. 1515, Ilorin, Kwara State, Nigeria*
[2] *Department of Chemical Sciences, Faculty of Science and Science Education, Anchor University, P.M.B. 001, Ipaja, Lagos, Nigeria*

Author E-mails:
obaleye.mo@unilorin.edu.ng
iejidike@aul.edu.ng
*Correspondence to: BAMIGBOYE, M.O., Department of Industrial Chemistry, Faculty of Physical Sciences, University of Ilorin, P.M.B. 1515, Ilorin, Kwara State, Nigeria, EJIDIKE, I.P., Department of Chemical Sciences, Faculty of Science and Science Education, Anchor University, P.M.B. 001, Ipaja, Lagos, Nigeria
DOI: 10.38061/idunas.629389

Received: October 04, 2019; Accepted: December 31, 2019

Abstract

Mixed complexes of Ibuprofen-Pyrimethamine were synthesized using Cd(II) Co(II), Zn(II), and Mn(II). The mixed complexes were characterized based on some physicochemical and spectroscopic techniques such as infrared, elemental analysis, conductivity measurements, and magnetic moment. Based on the results obtained, the complexes were formulated as $[M(L_1)(L_2)]Cl_2$, where M = metal ion, L_1 = Pyrimethamine, L_2 = Ibuprofen). The complexes were found to be non-electrolytes. The ligands act as bidentate towards the central metal ions with deprotonation occurring at the carboxylic group. The complexes were also analyzed by conductometric titration. Antimicrobial screening against the selected organisms: *Escherichia coli*, *Pseudomonas aeruginosa*, *Staphylococcus aureus*, *Bacillus substilis*, *Bacillus megaterium and Serratia marcescens* for the complexes alongside the free ligands were investigated. The antimalarial study was investigated for the compounds against *Plasmodium berghei* (NK 65 strain). It was observed that the complexes showed significant potentials against the studied organisms.

Keywords: Ibuprofen, Antimicrobial, Pyrimethamine, Metal Complexes, Antimalarial.

1. INTRODUCTION

Research towards improving the therapeutic effects of drugs has become the frontiers of numerous inorganic researchers towards synthesizing potent drugs with better therapeutic effects on microorganisms with resistance to previous drugs (Triathi and Aarti, 2015). Metal-drug complexes are of great interest to researchers due to their different medicinal use for the treatment of diseases (Alaghaz et al., 2013). It was discovered recently that some gold complexes had been investigated for the treatment of Rheumatoid arthritis. Some ruthenium compounds have shown antitumor activity due to the protein and DNA binding capacity of the metal ion (Cassells et al., 2018). Many kinds of research have been carried out on the

combination of some antimalaria drugs which are effective in the treatment of the disease. Mixed Artesunate and Lapdap (Chlorproguanil/dapsone) drugs have been confirmed to be an improvement in the Treatment of malaria through combined therapy and the elimination of the parasites from the body system (Waziri et al., 2018).

A few years back, the formation of mixed antimalarial drug complexes attracted great attention as a result of their interesting molecular structures (Huang et al., 2016), catalytic abilities and especially their potential uses in the area of the biomedical field (Raheem et al., 2014). Chemotherapy is one of the methods used in the treatment of diseases such as cancer. The spread of parasites resistant to some drugs has become a cause for concern to researchers, and the recommendation to use a combination of drugs for full treatment has received wide attention (Enermose et al., 2014). Synthesis of novel metal-drug complexes depends on the capability of the central metal ions to enhance the therapeutic ability of the drug. Hence, some drugs are more effective upon coordination to the central metal ions (Recio Despaigne et al., 2014). Some metal complexes have been reported to be more effective than their parent ligand, such as bleomycin (Li-June, 2003). Many biologically active compounds used as drugs possess enhanced modified pharmacological and toxicological potentials when administered in the form of metal-based compounds (Ibrahim et al., 2015; Babamale et al., 2016). More research has been carried out on the application of antimalaria drug metal complexes which has which are more recognized as a leading candidate for the treatment of different infectious diseases (Padman et al., 2016)**.** The preparation of antimalaria drug metal complexes has led the research into the effect of the coordinated metal ion on the pharmacological properties of the ligand (Ramachandran et al., 2017; Safila and Lailoona, 2014). In continuation of this work, we envisage that the synthesis of mixed Ibuprofen- Pyrimethamine metal complexes would lead to enhanced therapeutic ability on micro-organisms that have developed resistance to these drugs.

2. MATERIALS AND METHODS

All reagents and chemicals used for this research work were of analytical grade and utilized without further purification. Ibuprofen and Pyrimethamine were obtained from Rajrab Pharmaceutical company (Ilorin, Nigeria), while cadmium(II) chloride, zinc(II) chloride, cobalt(II) chloride, manganese(II) chloride were obtained from Sigma-Aldrich (USA). The melting point of the synthesized complexes was recorded on the Gallenkamp melting point apparatus (Melting point SMP 10) and conductivity measurements were carried out using Jenway 4510 conductivity meter at the Department of Chemistry, University of Ilorin, Ilorin, Nigeria. The IR spectra were recorded in KBr pellets within the range of 4000-400 cm^{-1} on the Buck Scientific M500 IR spectrometer at the Redeemer University, Sango-Ota, Nigeria. All organisms used for screening purposes of the complexes were obtained from the Department of Microbiology, University of Ilorin, Nigeria.

2.1. Synthesis of the complexes

The metal complexes were synthesized in line with the method adopted from Lawal and Obaleye (Lawal and Obaleye, 2007) with some modifications. 1 mmol of $CdCl_2$, $ZnCl_2$, $CoCl_2$, $MnCl_2$, each dissolved in warmed aqueous solution (15 ml) was mixed to a cold solution of ibuprofen (1 mmol, 15 ml of ethanol) and solution of pyrimethamine (1 mmol, 15 ml of DMSO). The resulting mixture was stirred thoroughly and refluxed for 2 hours. It was left and allowed to stand for 24 hours. Immediately, the coloured precipitate was formed and isolated by filtration under vacuum. They were washed with mixed distilled water and ethanol and then dried in a desiccator using silica gel for further analysis.

2.2. Antimicrobial Screening

The antimicrobial screening was carried out by adopting the procedure reported by Ahmed et al. (**2009**) was adopted. The complexes were screened against the following selected organisms such as Gram-positive bacteria: *Staphylococcus aureus, Bacillus substilis, Bacillus megaterium*, and Gram-negative bacteria:

Serratia marcescens, *Escherichia coli*, *Pseudomonas aeruginosa*. The complexes were dissolved in their suitable solvent at certain concentrations. Filter paper discs were used for screening by saturating the discs with the solution of the complexes. The filter paper discs were positioned on the surface of the prepared solidified nutrient agar plates. Afterwards, they were seeded by the organisms and then incubated for twenty-four hours at a temperature of 37 °C for bacteria.

2.3. Antimalarial activities

The antimalarial study was investigated following the procedure. (Tella and Obaleye, 2010). *Plasmodium berghei* (NK 65 strain) was collected from Nigeria Institute of Medical Research and the parasites were maintained weekly by blood passage in mice.

2.3.1. Inoculation of experimental mice

The infection of the mice was performed within the cavity of the peritoneum with standard inoculum (0.2 ml of $1x10^{-7}$ parasitized Red blood cell). The inoculum was from a single donor mouse previously infected with *Plasmodium berghei* (33 percent *parasitaemia*).

2.3.2. Animal grouping and extract administration

After confirmation of *parasitaemia* in the animals, the animals were divided into six groups containing five mice, seventy-two hours post-inoculation. Test agents were orally given to the first four groups with different concentrations for five days while group 5 was given a standard drug for five days while group 6 (control) was left untreated but was administered an appropriate volume of distilled water (Adibi et al., 2012).

2.3.3. Determination of percentage *parasitaemia*

After twenty-eight days of investigation, the percentage of *parasitaemia* was evaluated using the formula below:

$$\%\ Parasitaemia\ = \frac{\text{Parasitized RBC}}{\text{Parasitized RBC + Non parasitized RBC}}\ \ X\ 100$$

2.3.4. Determination of percentage chemosuppression

The percentage chemosuppression was calculated using the formula:

$$\%\ Chemosuppression\ A\ = \frac{\mathrm{B-C}}{\mathrm{AC}}$$

Where B = Parasitaemia in the study group, C = Parasitaemia in control

2.4. Conductometry titration

This type of conductometric titration was performed following the method reported by (Abdel-Nasser et al., 2009). The solution of ibuprofen (0.01 M) was prepared in a 4:1 mixture of methanol and water. Metal ions were prepared using the same solvents with a concentration of 0.02 M. The Ibuprofen ligand was titrated against metal salts solution using a mono variation method and each conductance reading was taken after every 1 ml of Ibuprofen was added. The graph of conductance against volume was plotted.

2.5. Metal-chelation studies

The procedure followed by (Renny et al., 2013) was adopted for the continuous variation and the determination of the composition of metal-chelation studies. Three series (C1, C2, C3) of an equimolar solution of ibuprofen ligands and metal salt solution were prepared.C1, 0-12 ml of metal salt was measured, and the total volume was made up to 12 ml in each case. Also, in C2 ligand solution was measured and C3 metal salt was prepared by mixing of 0-12 ml ligand solution. Conductance was taken and recorded for each solution and calculated using the C1+C2-C3 formula.

3. RESULTS AND DISCUSSION

3.1. Characterization of the compounds

The analytical result of the metal complexes is presented as shown in Table 1. From the elemental analysis, the formation and stoichiometry of the complexes in ratio 1:1 was confirmed. The estimated metal contents of the complexes were observed and compared with the experimental data, as presented in Table 1 (Abdel-Nasser et al., 2009). It indicates that they are in good agreement with each other (Fig. 1). The complexes do not decompose in air. It was also observed that the melting point of the metal drug complexes was higher than their free ligands. This is due to the formation of coordination compounds; hence, the complexes are electrolyte in nature (Shaker et al., 2009).

3.2. Infrared spectra analysis

The IR spectra of the mixed complexes of Ibuprofen and Pyrimethamine are presented in Table 2. The broadband at 3300 cm^{-1} in Ibuprofen was attributed to ν(OH) band. There was shifted to a higher frequency within the regions 3346 - 3399 cm^{-1} in the complexes (Fig. 2). This is attributable to intra-hydrogen bonding interaction between the H-atom of the hydroxyl group and its carbonyl group. The sharp band at 1720 cm^{-1} in Ibuprofen was assigned as ν(C = O) stretching vibrations. This was shifted to a lower frequency between 1650 – 1696 cm^{-1} in all the complexes, an indication of the coordination of the oxygen of the carbonyl group in Ibuprofen (Ayad, 2002). The ν(N-H) frequency in the free Pyrimethamine was shifted in all the complexes. It was observed in the same region between 3306 – 3478 cm^{-1} as in the free parent ligand. The ν(C = O), which occurs at 1720 cm^{-1} in Ibuprofen, is shifted to lower frequencies in all the complexes. It indicates that the central metal ions are directly coordinated to the oxygen of the carbonyl group (Shaker, 2009). The band at 519 – 647 cm^{-1} was observed in all the complexes which are attributed to metal to nitrogen. Formation of new bands between 710 – 725 cm^{-1} as assigned to ν(M–O) and ν(M–Cl) respectively. Pyrimethamine has four active coordinating sites. It was observed that Pyrimethamine and its complexes confirmed that the frequency bands which are attributed to the symmetrical and asymmetrical stretching mode of NH_2, change the complexes. It signifies that coordination occurs through the nitrogen of the pyrimidine group. All the complexes were observed to be in octahedral geometry except Zn(II) complex (Bamigboye et al., 2015). All complexes were tested using the $AgNO_3$ solution to determine the presence of chloride. A white precipitate of AgCl was formed and this showed the presence of chloride ion outside the co-ordination sphere (Aragoni et al., 2002).

3.3. Antimalarial activity

The complexes of mixed Pyrimethamine-Ibuprofen showed the antimalarial activity against the ligands based on the antimalaria activity, as shown in Table 3. Pyrimethamine was found to be effective than Ibuprofen. The average percentage for pyrimethamine is 31. The ligands and the complexes were compared which indicated that the complexes are more effective than their parent ligands. It could be a result of the coordination of the ligands to the metal ions which improve the effectiveness of the drug. It could also be observed that Co(II) and Zn(II) complexes exhibited the same antimalaria activity at 70 percent (Tella and Obaleye, 2010). The *parasitemia* level was determined by the number of erythrocytes that are being infected with the organisms: *Plasmodium berghei*. Based on the result, it was observed that the *parasitemia* indicates a high presence of trophozoite; hence, complexes showed potent antimalarial activity (Osowole et al., 2015). Antimalarial activities of the complexes with respect to the percentage reduction in parasitaemia can be ranked as follows: $[Mn(Pyr)(Ibu)Cl_2]$ > $[Cd(Pyr)(Ibu)Cl_2]$ > $[Co(Pyr)(Ibu)Cl_2]$ = $[Zn(Pyr)(Ibu)Cl_2]$ > [Ibuprofen] > [Pyrimethamine]. Following the results obtained in this studies, percentage (%) reduction in *parasitemia* for the synthesized compounds were more potent or active as compared to similar complexes reported by Tella and Obaleye (2010) with activities less than 70% as obtained in this study.

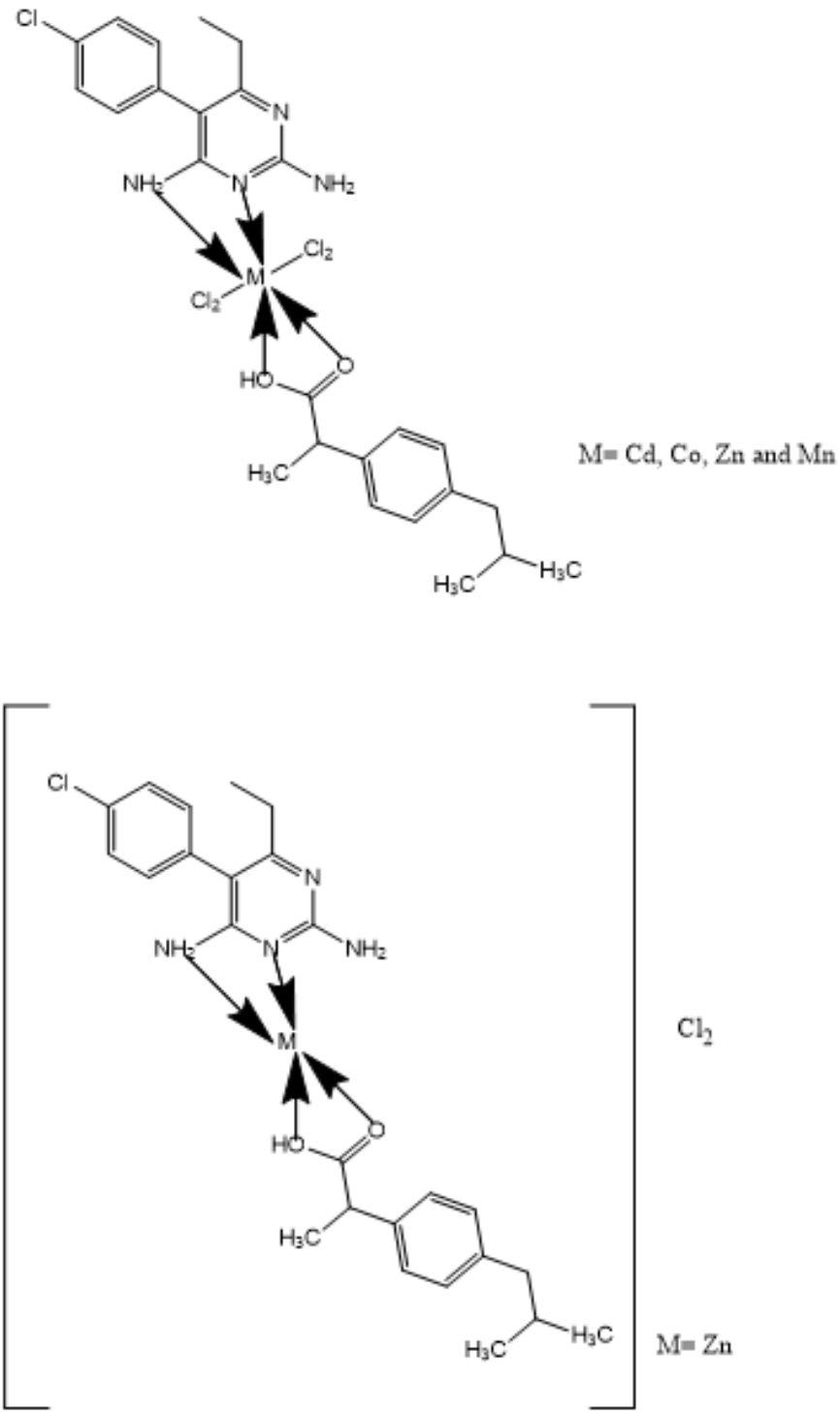

Figure 1. The proposed structure of the synthesized complexes.

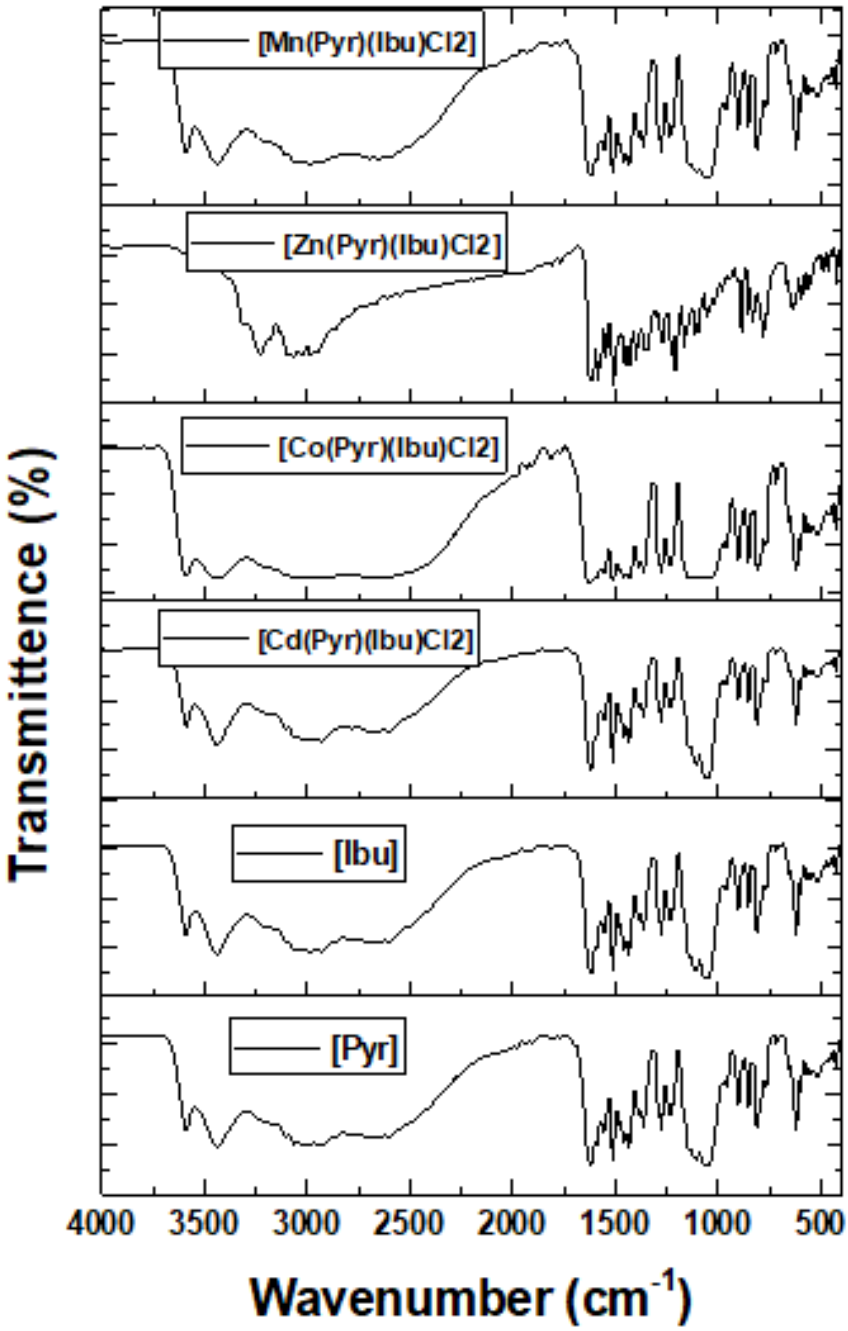

Figure 2. FT-IR of the ligands and the metal complexes.

Table 1. Analytical data of complexes.

Ligand/Complexes	Melting Point (°C)	Conductivity $\Omega^{-1}cm^2\ mol^{-1}$	Elemental Analysis (Theo/ Exp)			
			% C	% H	% N	% O
Ibuprofen	76	-	-	-	-	-
Pyrimethamine	233	-	-	-	-	-
$[Cd(Pyr)(Ibu)Cl_2]$	251	15	47.02/47.00	4.86/4.82	8.77/8.21	5.02/5.21
$[Co(Pyr)(Ibu)Cl_2]$	249	17	51.30/51.45	5.30/5.37	9.58/9.52	5.47/5.83
$[Zn(Pyr)(Ibu)Cl_2]$	255	12	50.74/50.65	5.24/5.44	9.47/9.00	5.41/5.32
$[Mn(Pyr)(Ibu)Cl_2]$	243	14	51.65/50.99	5.34/5.39	9.64/9.21	5.51/5.67

Table 2. Infrared data of the complexes.

Ligand/Complexes	υ(O-H)	υ(C=O)	υ(N-H)	υ(C=N)	υ(M-Cl)	υ(M-N)	υ(M-O)
Ibuprofen	3300	1720	-	-	-	-	-
Pyrimethamine	-	-	3450	1640	-	-	-
[Cd(Pyr)(Ibu)Cl_2]	3399	1674	3478	1679	795	605	725
[Co(Pyr)(Ibu)Cl_2]	3346	1650	3306	1698	754	519	710
[Zn(Pyr)(Ibu)Cl_2]	3368	1672	3325	1672	791	625	713
[Mn(Pyr)(Ibu)Cl_2]	3358	1696	3306	1653	799	647	718

Table 3. Antimalarial activities of the complexes (Percentage reduction in *parasitaemia*).

Ligand/Complexes	% Average *parasitaemia* before administration	% Average *parasitaemia* after administration	% reduction in *parasitaemia*
Pyrimethamine	42	44	31
Ibuprofen	40	58	45
[Cd(Pyr)(Ibu)Cl_2]	85	90	77
[Co(Pyr)(Ibu)Cl_2]	72	79	70
[Zn(Pyr)(Ibu)Cl_2]	60	63	70
[Mn(Pyr)(Ibu)Cl_2]	76	85	85

3.4. Conductometric Titration Study

The plotted graph between corrected conductance against the volume of mole-metal ligand shows the equivalent point in the graph and it was concluded that complex formation had taken place in ratio 2:1 (Figs. 3 and 4). The conductance of the reaction mixture increased continuously with complexes under investigation and this could be attributed to the presence of the ligand in ionic form (Tables 4 and 5). From the results, the method of continuous variation of the complexes (Tables 6 and 7) the stoichiometry reaction for the formation of a metal ion complex between Pyrimethamine and Ibuprofen, it also determines the concentration of colored central metal ion complex in solution (Shivankar et al., 2012).

Table 4. Conductometric titration between Pyrimethamine and $CoCl_2$.

Volume of metal ions	**Observed conductance (mS)**	**Corrected conductance (mS)**
0	0.098	0.990
1	0.113	0.114
2	0.125	0.123
3	0.138	0.221
4	0.216	0.265
5	0.260	0.315
6	0.314	0.319
7	0.317	0.320
8	0.319	0.440
9	0.436	0.503
10	0.492	0.500

Table 5. Conductometric titration between Ibuprofen and $CoCl_2$.

Volume of metal ions	Observed conductance (mS)	Corrected conductance (mS)
0	0.019	0.019
1	0.148	0.150
2	0.204	0.218
3	0.213	0.219
4	0.309	0.311
5	0.346	0.350
6	0.415	0.418
7	0.436	0.436
8	0.518	0.519
9	0.523	0.528
10	0.492	0.500

Table 6. Job's method (Concentration of Pyrimethamine 0.01M and concentration of $CoCl_2$ 0.01M).

Ratio	Conductance (mS)			
	M:S(C1)	S:L(C2)	M:L(C3)	Δ(C1+C2-C3)
0:10	0.008	0.013	0.012	0.009
1:9	0.012	0.014	0.016	0.010
2:8	0.025	0.019	0.021	0.023
3:7	0.037	0.024	0.025	0.036
4:6	0.041	0.030	0.034	0.037
5:5	0.038	0.032	0.040	0.030
6:4	0.029	0.028	0.035	0.022
7:3	0.025	0.025	0.026	0.024
8:2	0.022	0.018	0.016	0.042
9:1`	0.011	0.015	0.014	0.012
10:0	0.010	0.012	0.011	0.011

Table 7. Job's method (Concentration of Ibuprofen 0.01M and concentration of $CoCl_2$ 0.01M).

Ratio	Conductance (mS)			
	M:S(C1)	S:L(C2)	M:L(C3)	Δ(C1+C2-C3)
0:10	0.010	0.013	0.014	0.009
1:9	0.015	0.016	0.020	0.011
2:8	0.020	0.021	0.028	0.013
3:7	0.031	0.026	0.034	0.023
4:6	0.038	0.031	0.036	0.033
5:5	0.043	0.040	0.043	0.040
6:4	0.035	0.035	0.038	0.032
7:3	0.032	0.030	0.035	0.027
8:2	0.023	0.021	0.033	0.011
9:1`	0.018	0.020	0.030	0.008
10:0	0.015	0.017	0.026	0.006

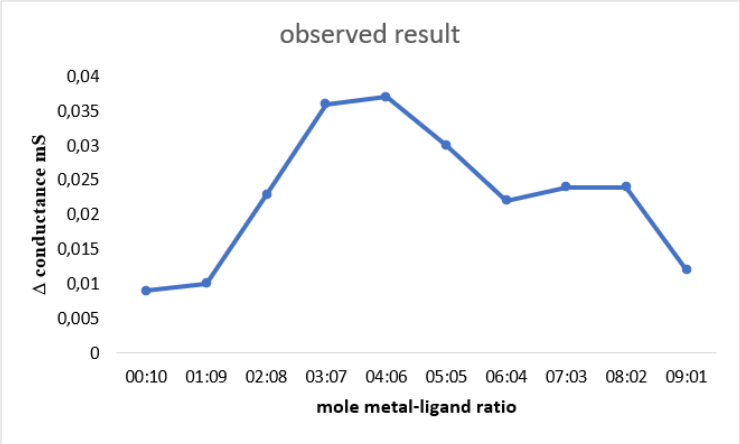

Figure 3. Graph of Job's method (Concentration of Pyrimethamine 0.01M and concentration of $CoCl_2$ 0.01M).

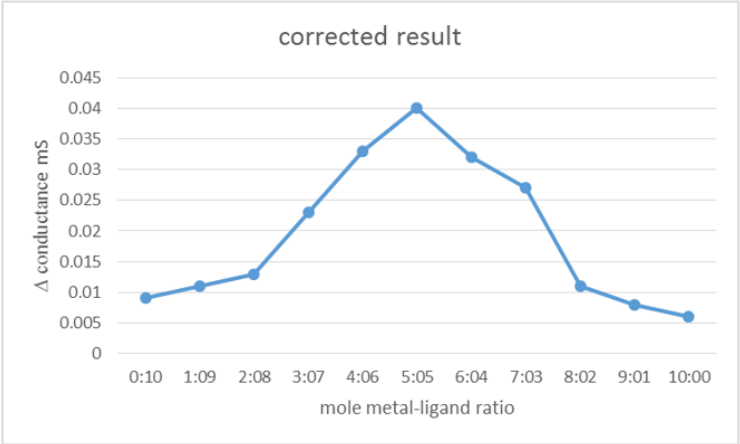

Figure 4. Graph of Job's method (Concentration of Ibuprofen 0.01M and concentration of $CoCl_2$ 0.01M).

Table 8. Antimicrobial activities of the complexes.

Ligands/Complexes	**Zone of Inhibition (mm)**					
	Sm(-ve)	**Bs(+ve)**	**Ec(-ve)**	**Sa(+ve)**	**Pa(-ve)**	**Bm(+ve)**
Pyrimethamine	-	-	9	-	11	13
Ibuprofen	2	-	5	-	2	4
[Cd(Pyr)(Ibu)Cl_2]	14	25	29	15	19	27
[Co(Pyr)(Ibu)Cl_2]	21	32	21	45	23	31
[Zn(Pyr)(Ibu)Cl_2]	33	28	14	24	17	20
[Mn(Pyr)(Ibu)Cl_2]	16	22	18	15	20	26

Footnote: Sm(-ve)= *Serratia marcescens*, Bs(+ve)= *Bacillus substilis*, Ec(-ve)= *Escherichia coli*, Sa(+ve)= *Staphylococcus aureus*, Pa(-ve)= *Pseudomonas aeruginosa*, Bm(+ve)= *Bacillus megaterium.*

3.5. Antimicrobial activity

Careful observation of the results obtained on antimicrobial activities of the ligands and complexes, it is evident that the complexes indicate higher activities against the studied organisms as compared with the free ligands at 20 µg/ml (Table 8). Antimicrobial resistance against some antimalarial and antibiotic drugs

are common in most countries. Several studies have reported that coordination enhances the effectiveness of metal complexes, thereby acting as potent bacterial agents (Srinivasan et al., 2003). Mixed-ligand complex [Co(Pyr)(Ibu)Cl_2] exhibited antimicrobial activities against both *S. marcescens* and *E. coli* bacteria tested with inhibition zone valve of 21 mm, and highest inhibition against *S. aureus* with zone value of 45 mm (Table 8; Fig. 5). Antimicrobial activities of the compounds against *P. aeruginosa* (gram -ve) is in the order: [Co(Pyr)(Ibu)Cl_2] > [Mn(Pyr)(Ibu)Cl_2] > [Cd(Pyr)(Ibu)Cl_2] > [Zn(Pyr)(Ibu)Cl_2] > [Pyrimethamine] > [Ibuprofen], while the compounds activities against *B. megaterium* (gram +ve) can be ranked as follows: [Co(Pyr)(Ibu)Cl_2] > [Cd(Pyr)(Ibu)Cl_2] > [Mn(Pyr)(Ibu)Cl_2] > [Zn(Pyr)(Ibu)Cl_2] > [Pyrimethamine] > [Ibuprofen]. However, due to aromaticity within the ligands, the coordination significantly increases the antimicrobial activity of the complexes. It has been discovered and reported that the ligands with nitrogen and oxygen donor active sites can inhibit enzyme production (Ejidike, 2018). The enzymes need these groups for their activity to be more susceptible to deactivation by the central metal ions upon coordination. It has been reported that coordination helps to lower the metal ion polarity also known as Tweedy chelation theory (Ejidike, 2018; Mosiniewicz-Szablewska et al., 2003) of the central metal ions due to donating of its positive charge through the donor atoms. The reaction of coordination helps to increases the lipophilic character of the metal ions which help its permeation through the lipid layer of the membrane. This increase in the hydrophobic behaviour and liposolubility of the complexes bring about crossing in the cell membrane of the organism leading to cell respiratory activity disruption and restricts further organism growth (Ejidike and Ajibade, 2017).

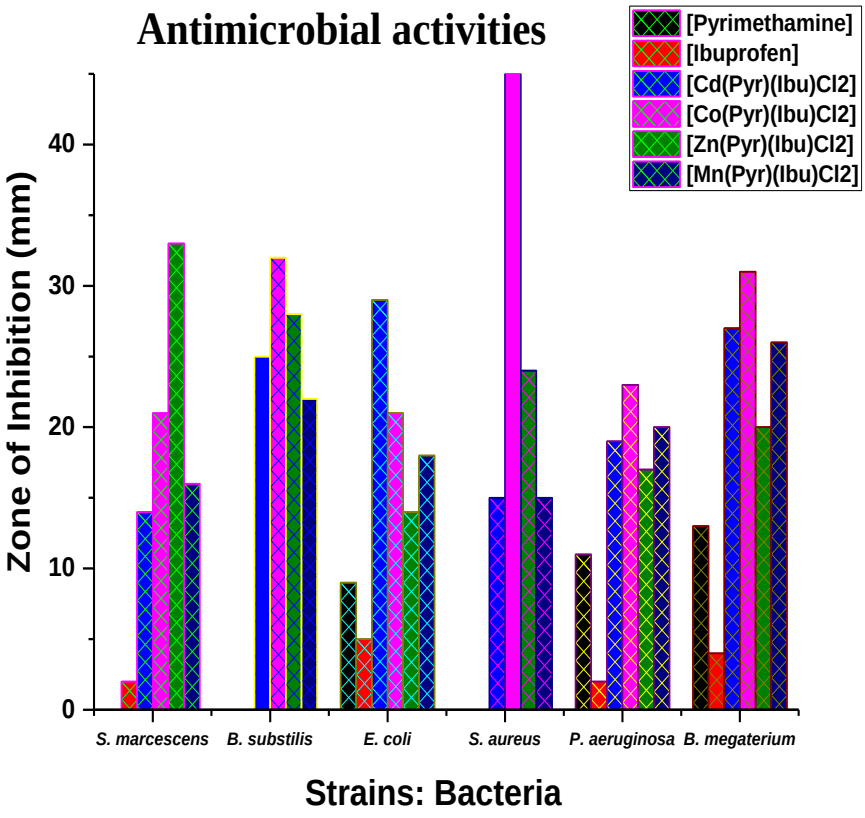

Figure 5. Zone of Inhibition of the compounds against studied bacteria strains.

.

4. CONCLUSION

Cd(II), Co(II), Zn(II), and Mn(II) complexes of mixed Pyrimethamine and Ibuprofen has been synthesized and characterized. Based on the results obtained, octahedral geometry has been proposed for the complexes except for Zn(II) complex which is in a tetrahedral geometry. Antimalarial and antimicrobial activities of mixed ibuprofen-pyrimethamine M(II) complexes [M = Cd, Co, Zn, Mn] indicated that the complexes exhibited higher activity as compared to the parent ligands. The multi-potential activities of the synthesized compounds support its usage for the development of chemotherapeutic agents useful for microbiological related ailments treatment.

Acknowledgments
The authors acknowledged that no financial support was received from any research organization in support of this work.

REFERENCES

Abdel-Nasser, M.A., Alaghaz, R.A., Ammar – Hany, M. (2009). Studies on the chelation of cyclodiphosph (V) azane complexes of Co(II), Ni(II), Cu(II), and Pd(II): Preparation, characterization, thermal, solid-state electrical conductivity, and biological activity studies. J. Phosphorus, Sulfur, and Silicon and the Related Elements. 184(9), 2472-2490.

Adibi, H., Zaker, S., Monkaresi, H. (2012). Synthesis and characterization of hydrazide-hydrazone derivatives of 3-pyridine carboxylic acid as antimycobacterial tuberculosis agents. J. Rep. Pharma. Sci. 1(1), 60-66.

Ahmed, R.N.**,** Sani, A., Igunnugbemi, O.O. (2009). Antifungal profiles of extracts of *Vitellaria paradoxa* (shea-butter) bark. *Ethnobot. Leaflets* 13, 679-688.

Alaghaz, A.N.M.A., Farag, R.S., Elnawawy, M.A., Ekawy, A.D.A. (2013). Synthesis and spectral characterization studies of new trimethoprim-diphenylphosphate metal complexes. Int. Jour. Sci. Res. 5(1), 1220-1229.

Aragoni, M.C., Arca, M., Demartin, F. (2002). Fluorometric chemosensors. Interaction of toxic heavy metal ions Pb(II), Cd(II), and Hg(II) with novel mixed-donor phenanthroline-containing macrocycles: spectrofluorometric, conductometric, and crystallographic studies," Inorg. Chem. 41(1): 6623-6632.

Ayad, M.M. (2002). Spectrophotometric and AAS determination of ramipril and enalapril through ternary complex formation. J. Pharm. Biomed. Anal. 28(1), 311-321.

Babamale, H.F., Lawal, A., Rajee, O.A., Oloyede, E.A. (2006). Synthesis, characterization and biological activity studies of mixed paracetamol - ascorbic acid metal complexes. J. Appl. Sci. Environ. Manage. 20(4), 1157-1161.

Bamigboye, M.O., Tella, A.C., Gbadebo, T.E., Eke, U.B., Obaleye, J.A. (2015). Amodiaquine-Ibuprofen mixed metal complexes: synthesis, characterization and antimicrobial activities. Centrepoint Journal (Science Edition). 21(2), 84-93.

Cassells, I., Stringer, T., Smith, G.S. (2018). Impact of various lipophilic substituents on ruthenium(II), rhodium(III) and iridium(III) salicylaldimine-based complexes: synthesis, *in vitro* cytotoxicity studies and DNA interactions. J. Bio. Inorg. Chem. 23(5), 763-774.

Ejidike, I.P. (2018). Cu(II) Complexes of 4-[(1*E*)-*N*-{2-[(*Z*)-Benzylidene-amino]ethyl}ethanimidoyl] benzene-1,3-diol Schiff base: Synthesis, spectroscopic, *in-vitro* antioxidant, antifungal and antibacterial studies. Mol. 23(7), 1581.

Ejidike, I.P., Ajibade, P.A. (2017). Synthesis, spectroscopic, antibacterial and free radical

scavenging studies of Cu(II), Ni(II), Zn(II) and Co(II) complexes of 4,4'-{ethane-1,2-diylbis[nitrilo(1*E*)eth-1-yl-1-ylidene]}dibenzene-1,3-diol Schiff base. J. Pharm. Sci. Res. 9(5), 593-600.

Enermose, E.A., Akporhnonor, E.E., Osakwe, S.A. (2014). Cu(ll) and Ni(lI) complexes of sulphamethazine mixed with pyrimethamine: synthesis, characterization and antimicrobial study. Chem. Mat. Res. 6(6), 9-14.

Huang, T.H., Yan, J., Yang, H., Tan, C., Yang, Y. (2016). Synthesis, structures, and properties of polynuclear silver complexes containing tetra-phosphine ligand with Ag ·C interactions. Austr. J. Chem. 69(3), 336-342.

Ibrahim, N.M., Yosef, H.A.A., Ewies, E.F., Mahran, M.R.H., Ali, M.M., Mahmoud, A.E. (2015). Synthesis and antitumor evaluation of new heterocycles derived from 3-Methyl-2-benzothiazolinone hydrazone. J. Braz. Chem. Soc. 26(6), 1086-1097.

Lawal, A., Obaleye, J.A. (2007). Synthesis, characterization and antibacterial activity of aspirin and paracetamol metal complexes. Nigerian Society for experimental biology. Biokemistri. 19(1), 9-15.

Li-June, M. (2003). Structure and function of metallo-antibiotics. Med. Res. Rev. 23(6), 697-762.

Mosiniewicz-Szablewska, E., Slawska-Waniewska, A., Swiatek, K., Nedelko, N., Golebiewski, N. (2003). Magnetic properties of Ni-complexes in a hydrazone structure. Phy. Stat. Solid. (A) Appl. Res. 196(1), 213-216.

Osowole, A.A., Wakil, S.M., Alao, O.K. (2015). Synthesis, characterization and antimicrobial activity of some mixed trimethoprim-sulfamethoxazole metal complexes. World Appl. Sci. J. 33(2), 336-342.

Padman, S., Sapna, T., Sing, A.P. (2016). Synthesis, spectral characterization and antimicrobial studies of Schiff bases and their mixed ligand metal complexes of Co(II), Ni(II), Cu(II) and Zn(II). Am. J. Chem. 6(5), 119-125.

Mahdi, R.T., Al-Noor, T.H., Ismail, A.H. (2014). Preparation, characterization, and antibacterial properties of mixed ligand complexes of L-leucine and Sulfamethoxazole with Mn(II), Co(II), Ni(II), Cu(II), Zn(II), Cd(II) and Hg(II) ions. Advances in Physics Theories and Applications 27(1), 8-19.

Ramachandran, R., Prakash, G., Vijayan, P., Viswanathamurthi, P., Malecki, J.G. (2017). Synthesis of heteroleptic copper(I) complexes with phosphine-functionalized thiosemicarbazones: an efficient catalyst for regioselective *N*-alkylation reactions. Inorganica Chim. Acta. 464(5), 88-93.

Recio Despaigne, A.A., Da Silva, J.G., da Costa, P.R., Dos Santos, R.G., Beraldo, H. (2014). ROS-mediated cytotoxic effect of copper(II) hydrazone complexes against human glioma cells. Molecules 19, 17202-17220.

Renny, J.S., Tomasevich, L.L., Tallmadge, E.H., Collum, D.B. (2013). Method of continuous variations: Applications of job plots to the study of molecular associations in organometallic chemistry. Angew. Chem. Int. Ed. Engl. 52(46), 11998-12013.

Naveed, S., Jaweed., L. (2014). UV spectrophotometric assay of different brands of cephradine. Health Sciences Research 1(4), 84-87.

Shaker, S.A., Farina, Y. (2009). Preparing and characterization of some mixed ligands complexes of 1,3,7-trimethylxanthin, γ-picoline and thiocyanate with some metal ions. Am. J. Sci. Res. 5, 20-26.

Shaker, S.A., Farina, Y., Mahmmod, S., Eskendar M. (2009). Preparation and study of mixed ligand complexes of caffeine and cyanate with some metal ions. Aust. J. Basic Appl. Sci. 3(4), 3337-3340.

Shivankar, V.S., Burungale, A.S., Rajmane, M.M., Gavali, L.V. (2012). Synthesis, characterization and catalytic activity of mixed ligand transition metal complexes. Arch. Appl. Sci. Res. 4(5), 2289-2298.

Srinivasan, R., Sougandi, I., Venkatesan, R., Sambasiva Rao, P. (2003). Synthesis and room temperature single crystal EPR studies of a dinickel complex having an $Ni_2(\mu\text{-phenoxide})_2^{2+}$ unit supported by a macrocyclic ligand environment $[Ni_2(L)_2(OClO_3)_2]$ [L = 2-[(4-methyl-pyridin-2-ylimino)-methyl]-phenol]. Proceedings of the Indian Academy of Sci. 115(2), 91–102.

Tella, A.C., Obaleye, J.A. (2010). Synthesis and biological studies of Co(II) and Cd(II) 5-(3,4,5-trimethoxybenzyl)pyrimidine-2,4-diamine (Trimethoprim) complexes. Int. J. Biol. Chem. Sci. 4(1), 2181-2191.

Triathi, I.P., Aarti, K. (2015). Synthesis and characterization of some complexes of copper(II) with L-Asparginine, L-Histidine, L-Lysine. Am. J. Alzh. Dis. Dem. 3(1), 95-103.

Waziri, M.B., Fugu, N.P. (2018). Solvent-free synthesis, characterization and antimicrobial studies of calcium and potassium complexes with some cephalosporin antibiotics. Res. J. Chem. Sci. 8(6), 8-15.

DOI: 10.38061/idunas.631229

IDUNAS | NATURAL & APPLIED SCIENCES JOURNAL | 2019 Vol. 2 No. 2

Antibacterial activities of Some Mixed Isoniazid-Ibuprofen Metal Complexes: Chelation and Characterization

Research Article

Mercy O. Bamigboye *[1], Ikechukwu P. Ejidike[2], R. N. Ahmed[3]

[1]*Department of Industrial Chemistry, University of Ilorin, Ilorin, Nigeria*
[2]*Department of Chemical Sciences, Faculty of Science and Science Education, Anchor University, Lagos, Nigeria*
[3]*Department of Microbiology, University of Ilorin, Ilorin, Nigeria*

Author E-mail:
seymercyx@yahoo.com
Tel: +2347033328218
*Correspondence to: M. O. Bamigboye, Department of Industrial Chemistry, University of Ilorin, Ilorin, Nigeria
DOI: 10.38061/idunas.631229

Received: October 09, 2019; Accepted: December 31, 2019

Abstract

The input of metallo-pharmaceutical to biomedical research is of high remarkable effect in drug design either as therapeutic, diagnostic or MRI imaging agents to mention few. Ranges of d - orbital transition metals: Cu(II), Zn(II), Mn(II), Ni(II), and Cd(II) complexes bearing Isoniazid-Ibuprofen mixed ligands have been synthesized. The prepared complexes were characterized by using microanalytical, infrared spectroscopy and CHN elemental analysis. FT-IR spectroscopic data showed that the ligands coordinate to the metal ion via the oxygen and nitrogen donor atoms from Isoniazid and oxygen of the carboxylic group and oxygen of the hydroxyl group of Ibuprofen. The elemental analysis measurement supports an octahedral geometry complexes proposed in line with the electronic structures of the metal ions. Comparative antibacterial study of the synthesized metal complexes and their parent ligands against *Escherichia Coli*, *Staphylococcus aureus*, and *Pseudomonas aeruginosa* microorganisms were carried out. [Ni(ISO)(IBR)Cl_2] and [Co(ISO)(IBR)Cl_2] exhibited the highest antibacterial activities than other complexes, however, the metal complex activities were found higher than the free ligands.

Keywords: spectroscopic, isoniazid, ligands, antibacterial, metal Complex

1.INTRODUCTION

The use of metal complexes and their applications in medicine have continued to increase. Metal complexes have found application as medicinal agents in the treatment of various diseases. Recently, platinum (II) complexes have been screened as antitumor drugs, while silver and gold complexes have been used as antibacterial and antiarthritic agents with gold compounds (auranofin, solganol and miochrysine) found to be very important in treatment of arthritis (Naglah et al., 2015).

Tuberculosis (TB) has been known to be a disease that produces millions of deaths annually, being the leading cause of mortality in developing countries. The number of persons infected with tuberculosis is also growing in developing countries, especially in persons infected with the human immunodeficiency virus (HIV) (Maria et al.,2013; Arounaguiri et al., 2000; Adadey and Sarfo, 2016; Poggi et al., 2013).

Isoniazid has been known to be an antimycobacterial drug effective in the prevention and treatment of tuberculosis (Mukherjee, 2000; Diana et al., 2012). It is also of considerable interest due to its ability to coordinate with metals via the heterocyclic nitrogen atom of the pyridine ring and/or the carbonyl oxygen and nitrogen atoms of the hydrazide group (Obaleye et al., 2011). Ibuprofen (α,α-methyl-4-(2-methylpropyl) benzenaceticacid) is known to be an important non-steroidal anti-inflammatory drug (NSAID). It has finds application in the treatment of inflammatory and painful rheumatic and non-rheumatic diseases (Amolegbe et al., 2012). The carboxylate group in its structure makes it possible for metal-ligand interactions.

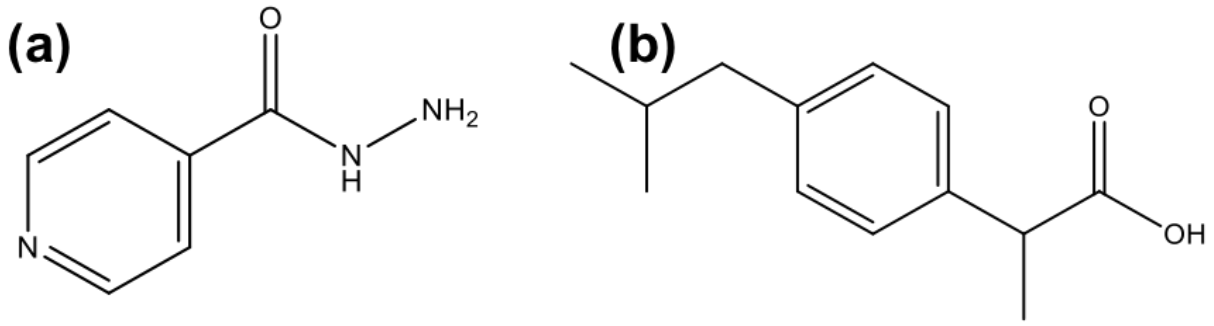

Fig. 1: Structure of (a) Isoniazid; (b) Ibuprofen

An increase in drug-resistant microbial strains of the disease (MDR-TB) has been of alarming rate making it difficult for the control of the disease effectively. In addition to this, drug-drug interactions have been observed between TB drugs and anti-HIV treatments and other medications used in treatment of chronic disease such as diabetics (Obaleye et al., 2011).

Research into synthesis and application of drug-metal complexes for the purpose of new drug synthesis is of great interest in inorganic, pharmaceutical and medicinal chemistry. Isoniazid is a front-line drug used in the treatment of Tuberculosis. ‘’The major route of isoniazid resistance relies on KatG enzyme disruption, which does not promote an electron transfer reaction’ (Chaudhary et al., 2005). Schiff bases of metal complexes of nitrogen and oxygen donor is of great interest due to different biological activities of pharmacological, antitumour, fungicide, bactericide, anti-inflammatory, and antiviral activities (Prasad and Agarwal, 2007; Mewis and Archibald, 2010). Metal complexes have been greatly known as medicinal agents in the treatment of diseases. There are some platinum (II) complexes used clinically as antitumor drugs (Diana et al., 2012). It has been observed that Ibuprofen -copper and zinc complexes are used as preservative solutions which penetrate wood. With the absence of the ammonia from the wood, the complexes are retained in the wood providing a long-lasting preservative (Tella and Obaleye, 2010).

2. EXPERIMENTAL SECTION

Isoniazid and Ibuprofen were purchased from Sigma Aldrich. All the reagents and chemicals used for this research work were of analytical grade. They were purified by standard procedure. The IR spectra of the complexes were carried out and reported using FT-IR Spectrophotometer at Redeemer University, Nigeria. The elemental analysis was carried out and reported at Medac Limited, Brunel Science, Egham, United Kingdom for the determination of percentage chemical elements (CHN) present in the complexes.

2.1 Synthesis of the complexes [M(IBR)(ISO)Cl_2]

The procedure described by (Tella and Obaleye, 2010)was followed with little modification in the synthesis of these complexes. 0.14 g (1 mmol) of Isoniazid in 20 ml of methanol and 0.21 g (1 mmol) of Ibuprofen in 20 ml of ethanol were mixed together with the chloride salts of the metals (M = Cu^{2+}, Zn^{2+}, Mn^{2+}, Ni^{2+}, Cd^{2+}) dissolved in the suitable solvents. The mixture was refluxed for three hours at a determined temperature and allowed to cool at room temperature. A precipitate was obtained, filtered and washed with the mixed solvent used to remove any unreacted substances. It was dried in a desiccator and stored in a sample bottle for further analysis.

2.2 Antimicrobial screening

Nutrient broth was used in this study to activate the growth of the selected organisms. It was prepared by weighing 4 g of the Nutrient broth in 250 ml of the conical flask containing distilled water to dissolve. The conical flask was plugged with a well fitted cotton wool and wrapped with an aluminum foil. It was then sterilized in an autoclave at 121 °C for fifteen minutes. It was transferred into petri- dish and allowed to cool. Hole borer was used to form a hole at the center of the solidified agar. The selected organisms were introduced at the hole and incubated at 37 ^{o}C for twenty-four hours. The plates were checked for possible zones of inhibition (Tella and Obaleye, 2013).

2.3 Determination of Minimum Inhibitory Concentration (MIC)

Procedure followed by (Collins et al., 1995) was adopted. The free ligands and their complexes were prepared at concentration of 20 and 40 mg/ml and were transferred into different test tube. The test tube was inoculated with some selected isolated organisms such as *Escherichia Coli, Staphylococcus aureus* and *Pseudomonas aeruginosa.* They were diluted to obtain a final concentration of about hundred cells per ml. The prepared test tubes were then incubated at 37 °C for twenty hours. It was observed that the complexes that has the least concentration inhibited the growth of the isolated organisms in broth cultured.

2.4 Determination of Minimum Bactericidal Concentration (MBC)

After the isolated organisms has been cultured separately in the nutrient broth of different concentration of the synthesized complexes, the nutrient broth was then inoculated into the agar plate to assay for the bactericidal effect. It was inoculated for twenty hours at 37 °C. It was shown that the lowest concentration of the ligands inhibited the growth on the plate immediately after incubation (Alade and Irobi, 1993).

2.5 Stoichiometry and stability constant of complexes

2.5.1 Preparation of the ligands solution

A modified procedure as reported in the literature was adopted (Tella and Obaleye, 2013). Fresh stock solution of Isonicotinic Acid Hydrazide and Pyrazine-2-carboxamide were prepared. A known certain weight of the ligands: Isonicotinic Acid Hydrazide (0.14 g/L,) and Pyrazine-2-carboxamide (0.12 g/L in) were determined by dissolving them in their appropriate solvents (20 ml of ethanol and 20 ml of mixed acetone-methanol) respectively.

2.5.2 Preparation of metals solution

Solution of 0.05 M of Zn(II), Cu(II), Fe(II), Ni(II),Co(II) and Mn(II) metals (0.07g/L, 0.06 g/L, 0.06 g/L, 0.06 g/L, 0.06 g/L and 2.75 g/L) respectively were prepared by dissolving them in their suitable solvents. Distilled water was the only solvent used in dissolving all the metal ions (Tella and Obaleye, 2010).

2.5.3 Determination of the absorbance of the metals - ligands solution

Different solutions were prepared by adding different volumes of 0.05 M of each solution of the metals and the ligands. The ionic strength was maintained using 0.1 M KNO_3 at pH 7.4. The absorbance was determined using ultraviolet spectroscopy (Ogunniran et al., 2008).

2.5.4 Stoichiometry determination

Solution of 0.05 M of the ligands and the metals were prepared. Different mixtures of the metal ions (Y ml) and (30-Y) ml of the ligands were top up to 30 ml of a volumetric flask. Absorbance was determined using Ultraviolet spectroscopy following Job method of continuous variation (Ogunniran et al., 2012; Willey et al., 2008).
A graph of absorbance against concentration of metal ion divide by concentration of the metal ions and concentration of the ligands were plotted.

3. RESULTS AND DISCUSSION

3.1 Chemistry of the compounds

The results of physicochemical data are as presented in Table 1. The melting points of the complexes were found to be higher than that of their parent ligands. This indicates the formation of the complexes (Fig. 1). The magnetic moments of the synthesized complexes are in the range of 0.68 B.M - 3.58 B.M. A magnetic moment of 0.68 B.M. was observed for Cd(II) complex which indicates that the complex is essentially diamagnetic. Nickel and cobalt complexes showed magnetic moment values of 3.47 B.M. and 2.29 B.M. respectively, suggesting octahedral geometry (Ogunniran et al., 2012).

The metal drug complexes were synthesized by refluxing method. The incorporation of the metals into the ligands spheres resulted in the formation of the complexes (Sousa et al., 2012). The compounds were characterized using Infrared spectroscopy and elemental analysis. The conductivity measurements were determined in methanol for the metal complexes with result indicating they are strong electrolytes. The elemental analysis of the complexes suggest that the compounds are pure and in good agreement with the molecular formula (Willey et al., 2008).

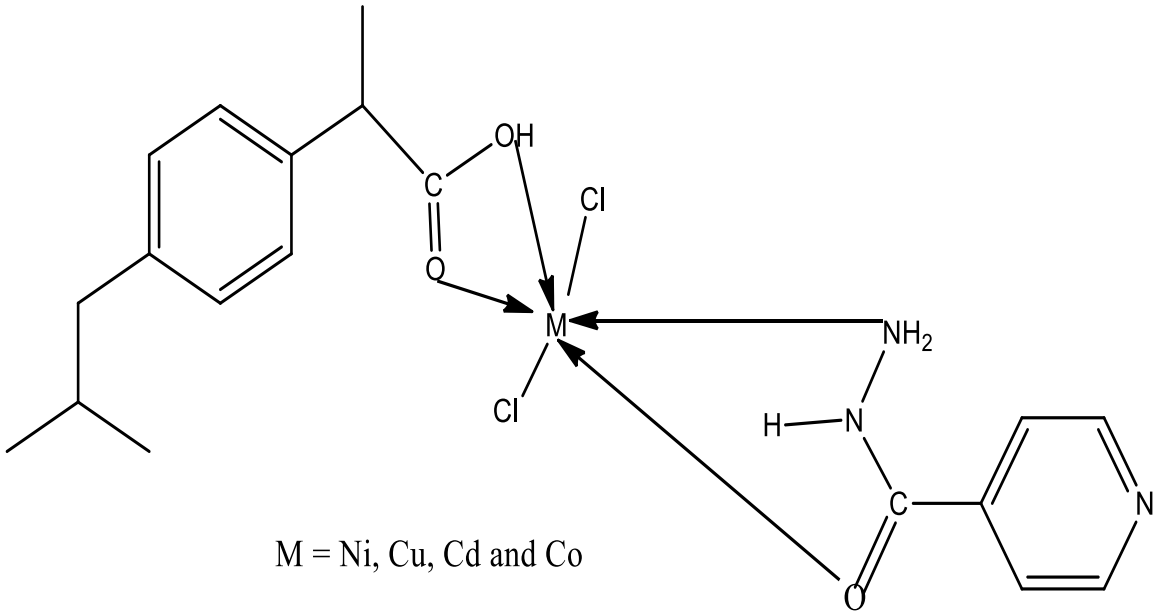

Figure 2: Proposed Structure of the complexes

Table 1: Physiochemical data of the ligands and their complexes

Ligands/Complexes	**Melting Point (₀C)**	**Found(Calculated)₀/₀**				**Conductivity $\Omega^{-1}Cm^2Mol^{-1}$**	**Magnetic Susceptibility (B.M)**
		C	**H**	**N**	**M**		
Isoniazid [ISO]	170-171	-	-	-	-	-	-
Ibuprofen [IBR]	75-77	-	-	--	-	-	-
[Ni(ISO)(IBR)Cl_2]	195-196	48.11/ 48.23	5.63/ 5.29	8.21/ 8.88	12.39/ 12.42	2.5	3.47
[Cu(ISO)(IBR)Cl_2]	186-188	47.77/ 47.74	5.57/ 5.24	8.61/ 8.79	13.29/ 13.31	3.1	3.58
[Cd(ISO)(IBR)Cl_2]	198-199	42.95/ 43.31	4.39/ 4.75	7.43/ 7.98	21.32/ 21.29	6.0	0.68
[Co(ISO)(IBR)Cl_2]	189-191	48.17/ 48.21	5.31/ 5.29	8.81/ 8.88	12.34/ 12.46	4.3	2.29

Table 2: Infrared spectra of the ligands and their complexes

Ligands/Complexes	**υ (C=O)**	**υ (O-H)**	**υ (C=N)**	**υ (N-H)**	**υ (C-N)**	**υ (M-N)**
Isoniazid (ISO)	1705	2945	-	-	2849	-
Ibuprofen (IBR)	1666	-	1552	3300	2816	-
[Ni(ISO)(IBR)Cl_2]	1786	3145	1616	3319	2810	516
[Cu(ISO)(IBR)Cl_2]	1735	3142	1610	3425	2814	519
[Cd(ISO)(IBR)Cl_2]	1720	-	1610	3319	2817	508
[Co(ISO)(IBR)Cl_2]	1715	3146	1614	3314	2811	512

3.2. Infrared absorption spectra

The Infrared bands of the prepared complexes were assigned based on the literature values obtained for similar structural compounds of the ligands (Sousa et al 2012; Ogunniran et al., 2008). The infrared spectra of both the complexes and the ligand (Fig. 3) were compared to determine the sites of coordination that may be involved in the synthesis (Ogunniran et al., 2012). A broad band within the region 3200-3600 cm^{-1} is observed which is due to asymmetric and symmetric O-H stretching vibration. The parent ligands act as a bidentate. Isoniazid is coordinated to the metal via the oxygen of the carbonyl group and nitrogen of the amine group while in Ibuprofen, the metal is coordinated through the oxygen of the carbonyl group and hydroxyl group. The band due to v(C=O) and v(N-H) were shifted to higher frequency in all the complexes. The shift to higher frequency for O in v(O-H) and v(C=O) indicate strong frequency and weak M-O. While shift to higher frequency in all the complexes indicates v(N-H). This suggest strong v(N-H) and weak M-N.

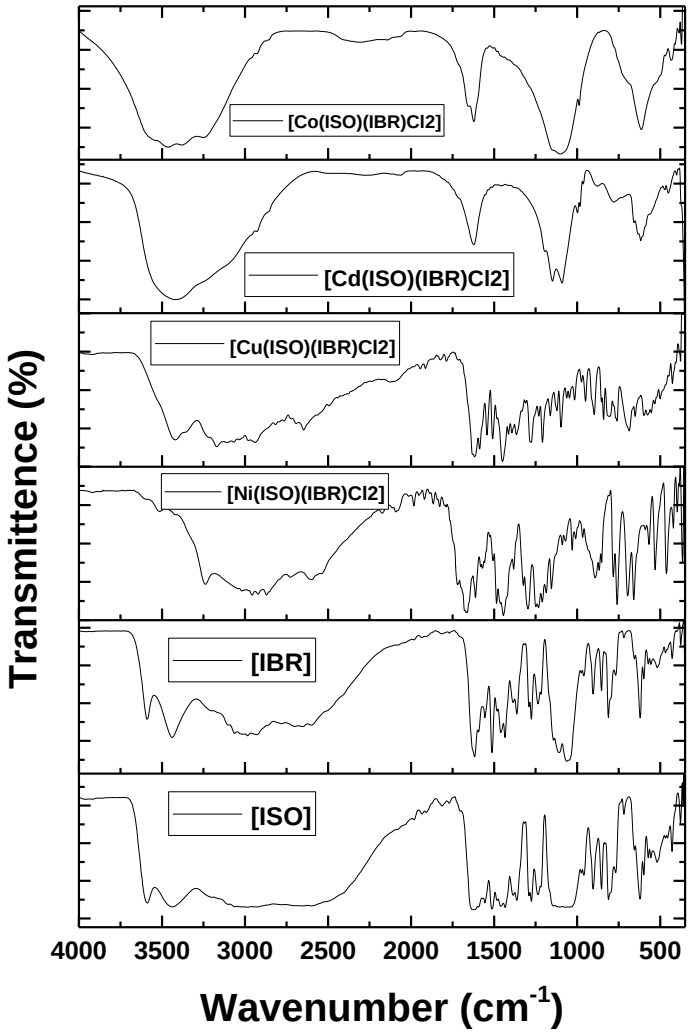

Figure 3: FT-IR of the synthesized complexes

Table 3: Antibacterial activity of the ligands and their complexes

Organisms	***Escherichia Coli***		***Staphylococcus aureus***		***Pseudomonas aeruginosa***	
Ligands/Complexes	Concentration (µl/ml)					
	20	40	20	40	20	40
Isoniazid (ISO)	-	-	-	11	-	-
Ibuprofen (IBR)	-	-	-	-	-	-
[Ni(ISO)(IBR)Cl_2]	11	14	8	12	8	13
[Cu(ISO)(IBR)Cl_2]	4	16	5	24	14	19
[Cd(ISO)(IBR)Cl_2]	22	29	13	14	13	16
[Co(ISO)(IBR)Cl_2]	9	12	11	11	17	18

Table 4: Minimum Inhibitory Concentration of the ligands and their complexes

Organisms	***Escherichia Coli***			***Staphylococcus aureus***			***Pseudomonas aeruginosa***		
Ligands/Complexes	Concentration (µl/ml)								
	5	10	15	5	10	15	5	10	15
Isoniazid (ISO)	-	-	-	-	-	-	-	-	-
Ibuprofen (IBR)	-	-	-	-	-	-	-	-	-
[Ni(ISO)(IBR)Cl_2]	+	+	+	+	+	+	+	+	+
[Cu(ISO)(IBR)Cl_2]	+	-	+	+	-	-	+	+	-
[Cd(ISO)(IBR)Cl_2]	+	-	-	+	+	+	+	+	+
[Co(ISO)(IBR)Cl_2]	+	+	+	+	+	+	+	+	+

Table 5: Minimum Bactericidal Concentration of the ligands and their complexes

Organisms	***Escherichia Coli***			***Staphylococcus aureus***			***Pseudomonas aeruginosa***		
Ligands/Complexes	Concentration (µl/ml)								
	5	10	15	5	10	15	5	10	15
Isoniazid (ISO)	-	-	-	-	-	-	-	-	-
Ibuprofen (IBR)	-	-	-	-	-	-	-	-	-
[Ni(ISO)(IBR)Cl_2]	+	+	+	+	+	+	+	+	+
[Cu(ISO)(IBR)Cl_2]	+	-	+	+	-	-	+	-	+
[Cd(ISO)(IBR)Cl_2]	+	+	+	+	+	+	+	+	+
[Co(ISO)(IBR)Cl_2]	+	+	+	+	+	+	+	+	+

DOI: 10.38061/idunas.631229

3.3 Antibacterial potentials

It was also observed that the complexes compounds exhibit greater zone of inhibition acting agent bacterial species. This confirm that the coordination increases the capability of the complexes to cross a cell membrane (Chohan and Supuran, 2006). The complexes possess high susceptibility in all the selected organisms. This indicates a pharmacological potential in the development control of the organisms (Reddy et al., 2012). The antibacterial resistance against some antituberculosis drugs such as Isoniazid were known in different countries during *in-vivo* analysis of pathogen (Yıldız et al., 2012). The metal present in the complexes could help to enhance the effectiveness against the species used. The MIC and MBC of the ligands and their complexes were studied and compared with the parent free ligands as presented in Table 4 and 5 respectively. Based on the result obtained, it was observed that the complexes indicated MIC and MBC properties in all concentrations. The data obtained showed that all the complexes are more effective except Cu complex in MBC. In MIC, it was observed that Ni and Co complexes are more effective than Cd and Cu complexes. In general, it was indicated that the ligands are not effective against the organisms when compared with their complexes (Liebowitz et al., 2001). The order of MIC activity of the as-synthesized complexes against the studied strains follows the order: $[Ni(ISO)(IBR)Cl_2]$ = $[Co(ISO)(IBR)Cl_2]$ > $[Cd(ISO)(IBR)Cl_2]$ > $[Cu(ISO)(IBR)Cl_2]$**.**

Table 6: Stoichiometry Determination of Metals - Isonicotinic acid hydrazide in Solution

Ligand	**Metal : Ligand**	**λ(nm)**	**M : L**
Isonicotinic Acid Hydrazide	Ni(II)ISO	365	1:1
		226	1:1
		218	1:1
		210	1:1
	Cu(II)ISO	245	1:1
		186	1:1
		167	1:1
		158	1:1
	Cd(II)ISO	357	1:1
		217	1:1
		209	1:1
		193	1:1
	Co(II)ISO	176	1:1
		148	1:1
		118	1:1
		112	1:1

Table 7: Stoichiometry Determination of Metals - Ibuprofen in Solution

Ligand	**Metal : Ligand**	**λ(nm)**	**M : L**
Ibuprofen	Ni(II)IBR	446	1:1
		211	1:1
		186	1:1
		153	1:1
	Cu(II)IBR	236	1:1
		211	1:1
		199	1:1
		171	1:1
	Cd(II)IBR	468	1:1
		308	1:1
		284	1:1
		200	1:1
	Co(II)IBR	431	1:1
		429	1:1
		377	1:1
		318	1:1

Table 8: Stability Constant determination of Metals- Isonicotinic acid hydrazide in Solution

Ligand	**M : L**	**λ (nm)**	**Lo**	**Mo/A X 10^{-4}**	**1/Lo**	**STABILITY CONSTANT**
Isonicotinic acid hydrazide	Ni(II)ISO	248	0.01	0.403	100	218
		231	0.02	0.433	50	
		234	0.03	0.427	33.3	
		282	0.05	0.355	20	
	Cu(II)ISO	216	0.01	0.463	100	154
		354	0.02	0.282	50	
		277	0.03	0.361	33.3	
		213	0.05	0.469	20	
	Cd(II)ISO	298	0.01	0.336	100	65
		314	0.02	0.318	50	
		323	0.03	0.309	33.3	
		487	0.05	0.205	20	
	Co(II)ISO	141	0.01	0.709	100	114
		135	0.02	0.741	50	
		119	0.03	0.840	33.3	
		174	0.05	0.575	20	

$M_o = 0.01M$

Equation for determining stability constant of complexes:

$$M_o/A = 1/\beta\varepsilon_c[1/L_o] + 1/\varepsilon_c$$

Where λ(nm) = Absorbance (A)
L_o = Concentration of the ligand
M_o = Concentration of the metal ion
β = Stability Constant

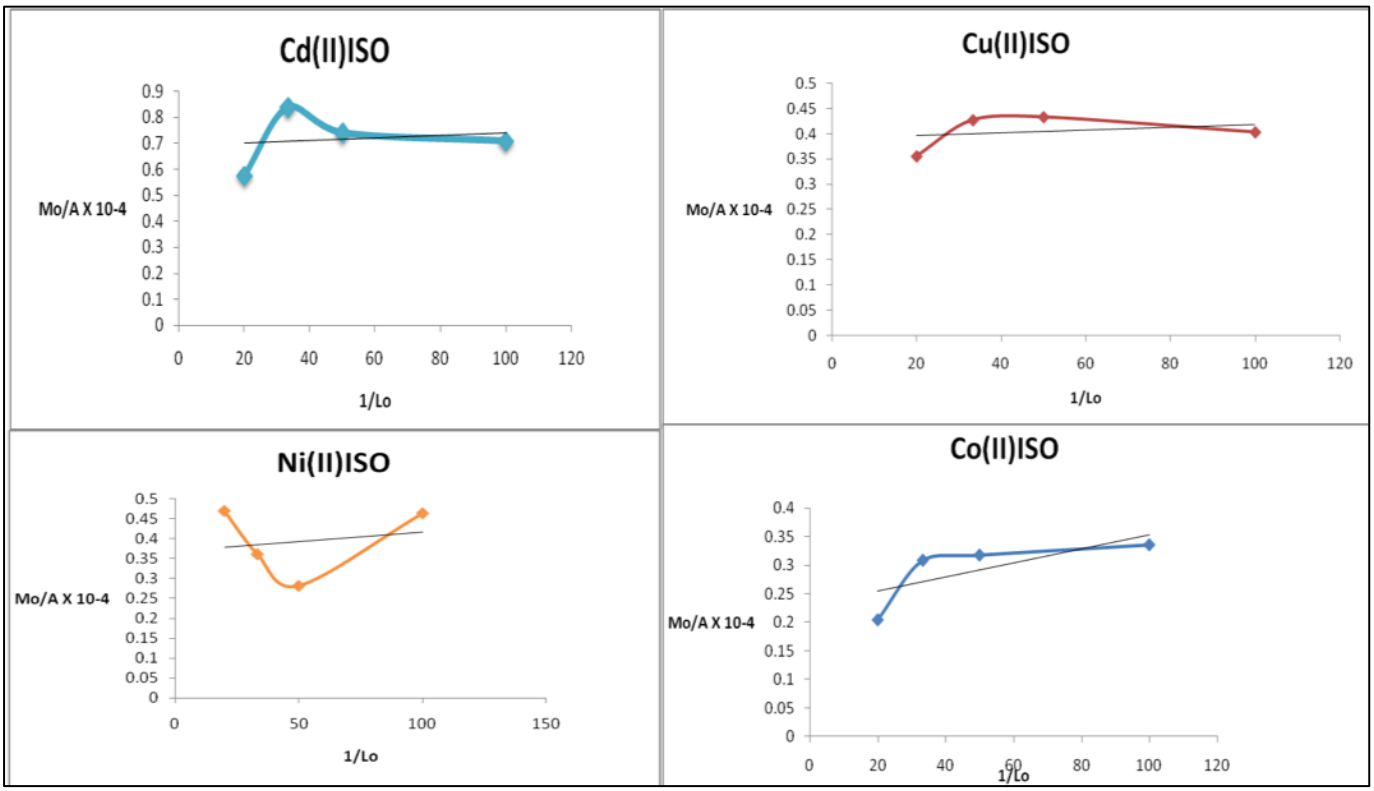

Figure 4: Graphical illustration of Stability Constant determination of Metals- Isonicotinic acid hydrazide in Solution

Table 9: Stability Constant Determination of Metal- Ibuprofen in solution

Ligand	**M : L**	**λ (nm)**	**Lo**	**Mo/A X 10-4**	**1/Lo**	**STABILITY CONSTANT**
Ibuprofen	Ni(II)IBR	324	0.01	1.543	100	231
		300	0.02	1.667	50	
		216	0.03	2.315	33.3	
		412	0.05	1.214	20	
	Cu(II) IBR	186	0.01	2.688	100	127
		211	0.02	2.370	50	
		235	0.03	2.128	33.3	
		241	0.05	2.075	20	
	Cd(II) IBR	146	0.01	3.425	100	81
		154	0.02	3.247	50	
		175	0.03	2.857	33.3	

	219	0.05	2.283	20	
Co(II)IBR	193	0.01	2.591	100	118
	205	0.02	2.439	50	
	243	0.03	2.058	33.3	
	265	0.05	1.887	20	

M_o = 0.01M

Equation for determining stability constant of complexes:

$$M_o/A = 1/\beta\varepsilon_c[1/L_o] + 1/\varepsilon_c$$

Where λ(nm) = Absorbance (A)

L_o = Concentration of the ligand

M_o = Concentration of the metal ion

β = Stability Constant

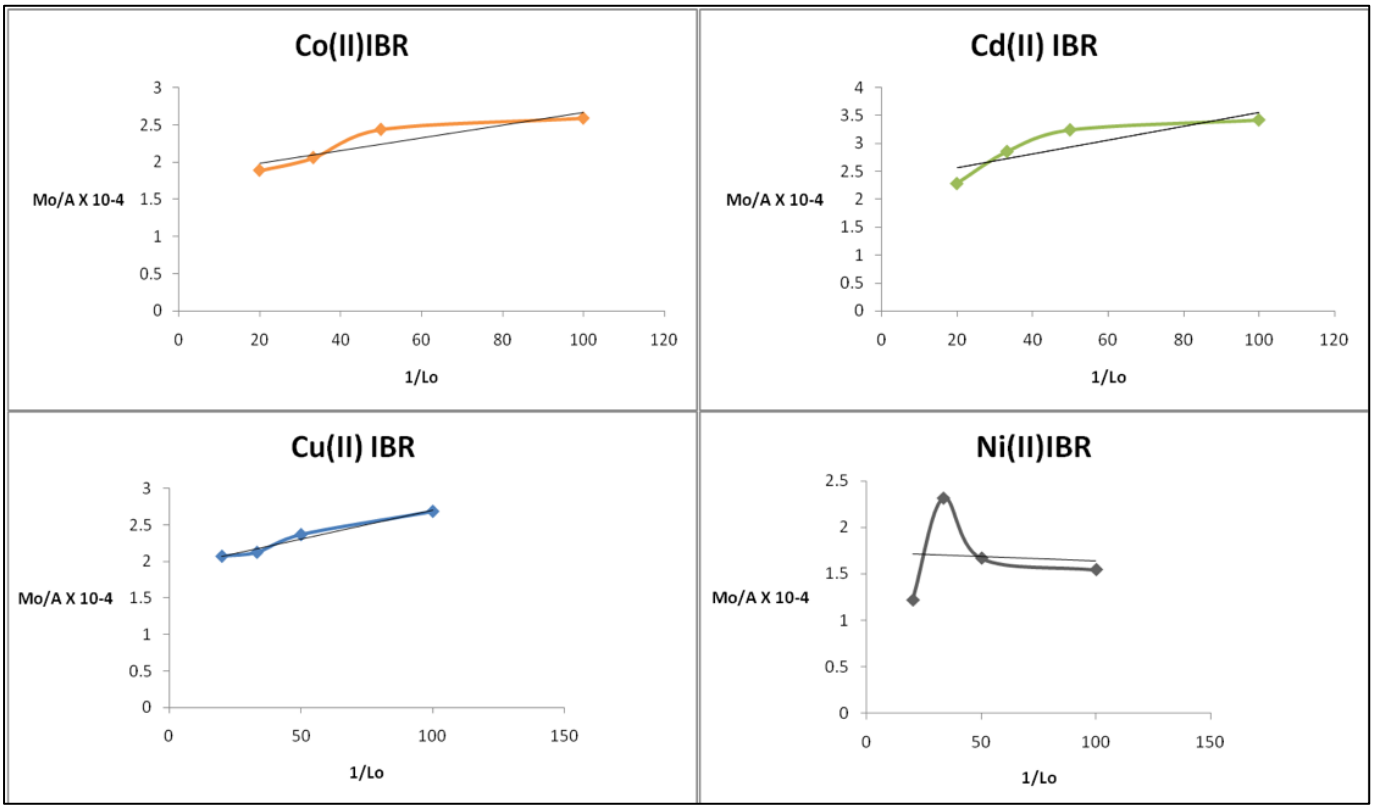

Figure 5: Graphical illustration of Stability Constant determination of Metals- Ibuprofen in Solution

From the result obtained for stability constants of the complexes as presented in Table 6-9, it was observed that the order of stability constant of the metal-ligand reaction follows this trend: Ni(II) > Cu(II) > Co(II) > Cd(II). The stability constants were found to be inversely proportional to the ionic radius of the metals. Ni(II) complex is the most stable being the metal ion with the smallest ionic radii while Cd(II) complex is the least stable because the crystal field stabilization energy of Cadmium is equal to zero and the electronic configuration is d_{10}. The order indicates that values increase with decreasing ionic radius of the metals. The order of the stability constant is in agreement with the trend of electronegativity and hence indicates that Irving-William rule is strictly obeyed (Irving and Williams, 1953).

4. CONCLUSION

Isoniazid and Ibuprofen alongside their complexes showed good yield in stoichiometry ratio of 1:1 with refluxing method. The results of the physical and spectroscopic analysis of the complexes confirm that the ligands have chelating properties coordinating to the metal ion via the oxygen of the carbonyl and hydroxyl group in Ibuprofen, and nitrogen of amine and oxygen of carbonyl group in Isoniazid. The antibacterial screening investigation confirms that the complexes possess higher antimicrobial activities as compared to the free ligands. [Ni(ISO)(IBR)Cl_2] and [Co(ISO)(IBR)Cl_2] exhibited the highest antibacterial activities against the screened bacterial strains, followed by [Cd(ISO)(IBR)Cl_2], while [Cu(ISO)(IBR)Cl_2] had the least activity, however, the activity was found higher than the free ligands. The results obtained in the study are of great significance towards further designing and developing metal (II) complexes towards combating bacterial resistance in the health sector. Incorporation of some metals into the bioactive ligands is a key metalloenzymes cofactor that can enhance greater inhibitory effectiveness against strains thus improving the development of a sensitive chemotherapy.

Acknowledgement

The authors acknowledge Industrial Chemistry Department University of Ilorin for their great support in providing for the reagents used during the research work.

REFERENCES

Adadey, S.A., Sarfo, J.K. (2016). Copper paracetamol complexes Promising lead antibacterial drug candidates. African Journal of Pure and Applied Chemistry. 10(5), 56-62.

Alade, P., Irobi, O.N. (1993). Antifungal activities of crude leaf extract of Acalypha wilkesiana. J. Ethnopharcol. 39, 171-174.

Amolegbe, S.A., Adewuyi, S., Akinremi, C.A., Lawal, A., Obaleye, J.A., Atayese, A.O. (2012). Mn(II), Ni(II), and Cu(II) Complexes of Artemisinin Derivatives: Synthesis, Characterization and Antimicrobial Activities. The pacific journal of science and Technology. 13(1), 424-429.

Arounaguiri S., Easwaramoorthy D., Ashokkumar A.(2000). Cobalt(III), nickel(II) and ruthenium(II) complexes of 1,10-phenanthroline family of ligands: DNA binding and photocleavage studies. Proc. Indian Acad. Sci. (Chem. Sci.). 112 (1),1.

Bamigboye, M.O. Anibijuwon, I.I., Ajiboye, A.E. (2017). Chelation, Characterization And Antimicrobial Studies Of Mixed Nicotinamide - Cloxacillin Metal Complexes. Nig. J. Pure and Appl. Sci. 30 (2).

Chaudhary, A., Phor, A., Singh, R. V. (2005). Potentially biodynamic tetraaza macrocycles and their manganese complexes: antiandrogen, antimicrobial and PDI studies," Bioinorganic Chemistry and Applications. 3(3-4),161-177.

Chohan, Z. H., Supuran, C.T. (2006). Metalloantibiotics: Synthesis,characterization and *in-vitro* antibacterialstudies on cobalt (II), copper (II), nickel (II) and zinc (II) complexes with Cloxacillin. Journal of Enzyme Inhibition and Medicinal Chemistry, 21(4), 441-448.

Collins, C.H., Lyne, P.M. and Grange, J.M. (1995). Microbiological methods (7_{th}edn) Butterwort – Heinemann Ltd. Britain. 175-190.

Diana, E., Chierotti, M.R., Marchese, E.M.C., Croce, G., Milanesio, M., Stanghellini, P.L. (2012). Blue and red shift hydrogen bonds in crystalline cobaltocinium complexes. New J. Chem. 36,1099.

Diana, E., Chierotti, M.R., Marchese, E.M.C., Croce, G., Milanesio, M., Stanghellini, P.L. (2012). Blue and red shift hydrogen bonds in crystalline cobaltocinium complexes. New J. Chem. 36, 1099.

Irving, H. M. N. H., Williams, R. J. P. (1953). The stability of transition-metal complexes". J. Chem. Soc. 3192–3210. doi:10.1039/JR9530003192.

Liebowitz, L. D., Ashbee, H. R., Evans, E. G. V., Chong, Y., Mallatova, N., Zaidi, M., Gibbs, D. (2001). Global Antifungal Surveillance Group. Diagn. Microbiol, Infect. Dis. 4, 27.

Maria, K. R. B., Francis, R. N. A., Vasanthi, R. P., Paulraj, A. (2013). Mixed Ligand Complexes Of Nickel(II), Copper(II) And Zinc(II) With Nicotinanilide And Thiocyanate. International Journal of Life science and Pharma research, 3(2),1.

Mewis, R.E., Archibald, S.J. (2010). Biomedical applications of macrocyclic ligand complexes. Coord. Chem. Rev. 254,1686-1712.

Mukherjee, R. (2000). Coordination chemistry with pyrazole based chelating ligands: molecular structural aspects. Coord. Chem. Rev. 203,151-218.

Naglah, A. M., Al-Omar, M. A., El-Megharbel, S. M., Refat, M. S. (2015). Structural, conductometric and antimicrobial investigations of ibuprofen analgesic drug complexes with certain metal ions. International Journal of Pharmacology. 11 (7), 773-785.

Obaleye, J.A., Adediji, J.F., Adebayo, M.A. (2011). Synthesis and biological activities on metal complexes of 2, 5-diamino-1, 3, 4-thiadiazole derived from semicarbazide hydrochloride. Molecules 16 (7), 5861-5874.

Ogunniran, K.O., Ajani, O.O., Ehi-Eromosele,C.O., Obaleye, J.A., Adekoya, J.A. and Ajanaku, C.O. (2012). Cu(II) and Fe(III)complexes of Sulphadoxine mixed with Pyrimethamine : Synthesis, Characterization, Antimicrobial andToxicology study. International Journal of Physical Sciences, 7(13), 1998-2005.

Ogunniran, K.O., Ajannaku, K.O., James, O.O., Ajani, O.O., Adekoya, J.A. and Nwionyi, O.C. (2008). Synthesis, Characterization, Antimicrobial activity and Toxicology study of some metal complexes of mixed antibiotics. African Journal of Pure and Applied Chemistry, 2(7), 69-74.

Poggi, M., Barroso, R., Costa-Filho, A. J., Barbosa de Barros, H., Pavan, F., Leite, F. C., Gambino, D., Torre, M. H., (2013). New Isoniazid Complexes, Promising Agents Against Mycobacterium tuberculosis. J. Mex. Chem. Soc. 57(3), 198-204.

Prasad, S., Agarwal, R.K. (2007). Cobalt(II) complexes of various thiosemicarbazones of 4-aminoantipyrine: syntheses, spectral, thermal and antimicrobial studies," Transition Metal Chemistry, 32(2), 143-149.

Reddy, N.S., Rao, S.A., Chari. M.A., Kumar, R.V., Jyothy, V., Himabindu, V. (2012). Synthesis and bacterial activity of urea and thiourea derivative of anacardic acid mixture isolated from a natural product cashew nut Shell liquid. Intl. J. Org. Chem., 2, 267-275.

Sousa, E.H., Basso, L.A., Santos, D.S., Diógenes I.C., Longhinotti, E., Lopes LG, Moreira, S. (2012). Isoniazid metal complex reactivity and insights for a novel anti-tuberculosis drug design. J. Biol. Inorg. Chem.17(2), 275-83. doi: 10.1007/s00775-011-0848-x.

Tella, A.C., Obaleye, J.A. (2010). Metal-Chelator: Stability constants of Transition Metal complexes of Pyrimidine and Sulphonamide Drugs. Int. J. Chem. Sci. 8 (3), 1675-1683.

Tella, A.C., Obaleye, J.A. (2013). Solvent-free synthesis, x-ray studies and *in vitro* inhibitory activities of copper(II) complexes of non-steroidal anti-inflammatory drugs. Research on Chemical Intermediates. doi: 10.1007/s11164-013-1050-1052.

Willey, J.M., Sherwood, L.M., Woolverton, C.J. (2008). Prescott, Harley and Klein's microbiology. McGraw-Hill,New York, NY, USA, 7th. ed.

Yıldız, G., Tuba B., Fatma, K.O., Selda O., Mustafa, F.S., Deniz, S.D. (2012). Synthesis of some new urea and thiourea derivatives and evaluation of their antimicrobial activities. Turk. J. Chem., 36, 279-291.